Identifying transplanted cells in the context of regenerative medicine for stroke

Nicholls, Francesca Joan

Awarding institution:
King's College London

IDENTIFYING TRANSPLANTED CELLS IN THE CONTEXT OF REGENERATIVE MEDICINE FOR STROKE

Francesca Joan Nicholls

Institute of Psychiatry, King's College London

Thesis submitted for the degree of PhD

2014

Abstract

Exogenous labels are often used to identify transplanted cells in order to elucidate their therapeutic mechanisms. In the context of stem and progenitor cell transplants, the requirements for exogenous labels must be ever more stringent in order to avoid both short and long term effects on the biology of these sensitive cell types, as well as to ensure accurate identification of transplanted cells. As cell therapies become more complex, there is also a need to be able to simultaneously image different cell populations in vivo.

Here four commonly used “optical” labeling protocols (Hoechst, BrdU, PKH26 and Qtracker) and an MRI contrast agent (a new Gadolinium nanoparticle based on ProHance) are assessed for their effects on human neural stem cell (hNSC) biology and their sensitivity and reliability for identification of transplanted cells.

With a view to developing useful paradigms for in vivo imaging of tissue engineering, two ParaCEST (Paramagnetic Chemical Exchange Saturation Transfer) agents are used to label hNSCs and human brain microvascular endothelial cells. MRI is then used to image each cell population separately after transplantation into the stroke cavity in a rat MCAO (middle cerebral artery occlusion) model.

These studies will allow the selection of labels that will have minimal effects on NSC biology whilst retaining maximal label reliability, and thereby allow accurate elucidation of the effects of complex cell therapies.

Acknowledgements

I would first and foremost like to thank Mike Modo for all his support, guidance and patience throughout my project, and for giving me the opportunity to complete some of my research in America, which has been a great experience. I'd also like to thank Brenda Williams for all her advice and support, and in particular for helping us with the logistics of working in the USA. It wouldn't have happened without her.

I'd also like to thank Wen Ling for his MRI expertise, and for his patience with my lack of MRI physics, and André Massensini for training me in the MCAO surgery. Thanks also to Tom Meade and his lab at Northwestern for working with us on the Gd project, and in particular to Matthew Rotz for being such an enthusiastic collaborator. And thanks also to Silvio Aime's lab in Torino, and Giuseppe Ferrauto in particular for fulfilling seemingly endless requests for agent.

I'd also like to thank Jessie, Harman, Terry and Tony for all their help in the lab in Pittsburgh, and for lots of useful discussions. And there were many people at King's who helped me get up and running at the start of my PhD. In particular I'm grateful to Ellen Bible, Anthony Vernon, Gehan El-Akabawy, Jon Cooper, Ivan Rattray, Ed Smith and Greg Anderson.

I'd also like to thank my mum Heather, my brother Julian, and my friends Emma and Tiziana for all their support and keeping me sane throughout.

I'd also like to thank the Medical Research Council for their financial support.

Table of Contents

Table of Figures

Table of Tables

Abbreviations

ATP	Adenosine Triphosphate
BBB	Blood Brain Barrier
BDNF	Brain-Derived Neurotrophic Factor
BLI	Bioluminescence Imaging
BOLD	Blood Oxygen Level Dependent
BrdU	5-bromo-2'-deoxyuridine
CEST	Chemical Exchange Saturation Transfer
CFDA-SE	Carboxyfluorescein Diacetate Succinimidyl Ester
CFSE	Carboxyfluorescein succinimidyl ester
CNS	Central Nervous System
CT	Computed Tomography
DALYs	Disability Adjusted Life Years
DAPI	4',6-diamidino-2-phenylindole
DiR	3,3,3',3' tetramethylindotricarbocyanine iodide
DNA	Deoxyribonucleic Acid
DWI	Diffusion Weighted Imaging
EC	Endothelial Cell
ECM	Extracellular Matrix
ES cells	Embryonic Stem cells
18FDG	[(18)F]fluorodeoxyglucose
FLAIR	Fluid-Attenuated Inversion Recovery
FOV	Field of View
FSE	Fast Spin Echo
Galc	Galactocerebroside
GDNF	Glial Derived Neurotrophic Factor
GECI	Genetically Encoded Calcium Indicator
GEMS	Gradient Echo Multi Slice
GFAP	Glial Fibrillary Acidic Protein
GFP	Green Fluorescence Protein
HBSS	Hank's Balanced Salt Solution
HCl	Hydrochloric Acid
HNA	Human Nuclear Antigen
Hoechst	2'-(4-Ethoxyphenyl)-6-(4-methyl-1-piperazinyl)-1*H*,3'*H*-2,5'-bibenzimidazole
HSV1-tk	Herpes Simplex Virus type 1 thymidine kinase
IHC	Immunohistochemistry
IP	Intraperitoneal

iPSC	Induced Pluripotent Stem Cell
IR	Inversion Recovery
ISH	In Situ Hybridization
LDH	Lactate Dehydrogenase
MCAO	Middle Cerebral Artery Occlusion
MEMRI	Manganese Enhanced MRI
MRI	Magnetic Resonance Imaging
MSME	Multi Slice Multi Echo
MTT	Methylthiazol Tetrazolium
NGF	Nerve Growth Factor
NMDA	N-methyl-D-aspartate
NSC	Neural Stem Cell
ParaCEST	Paramagnetic Chemical Exchange Saturation Transfer
PBS	Phosphate Buffered Saline
PET	Positron Emission Tomography
PFA	Paraformaldehyde
R1	Relaxivity, 1/T1
r_1	Molar relaxivity, slope of the line when concentration is plotted against R1
SAR	Specific Absorption Rate
SDF-1	Stromal cell-derived factor 1
SPECT	Single Photon Emission Computed Tomography
SPIO	Super Paramagnetic Iron Oxide
SVZ	Subventricular zone
t-PA	Tissue plasminogen activator
TA cells	Transit Amplifying cells
TE	Echo Time
TI	Inversion Time
TPM	Two Photon Microscopy
TR	Repetition Time
Tuj	Beta-III-Tubulin
UCOE	Ubiquitous Chromatin Opening Element
VEGF	Vascular Endothelial Growth Factor
WASSR	Water Saturation Shift Referencing

Chapter 1: Introduction

1.1 Stroke pathophysiology and treatment

Stroke is the third leading global cause of loss of Disability Adjusted Life Years (DALYs), with 572 DALYs lost per 100,000 in 2010 (Murray, Vos et al. 2012). The annual societal cost is estimated at £8.9 billion in the UK alone (Saka, McGuire et al. 2009). The only acute treatment currently available for stroke is tissue plasminogen activator (t-PA), which is used to break down thrombi and restore blood flow. However, only 14% of a sample of 11,262 stroke cases in the UK were eligible for t-PA, with the majority of exclusions due to the effective time window of three hours (Rudd, Hoffman et al. 2011). For the majority of stroke sufferers, there is no available intervention. Their vascular conditions can be appropriately treated to reduce the probability of another attack, but the only intervention to reduce symptoms resulting from damaged brain tissue is rehabilitation therapy. Rehabilitation is highly effective in improving functional outcome (Cifu and Stewart), but many patients still suffer from significant long-lasting disability. There is therefore an urgent need for therapies that can be applied in a broader time window and facilitate functional recovery to restore quality of life.

Ischemic stroke occurs when the occlusion of a blood vessel disrupts blood flow to an area of the brain. The reduction in oxygen and glucose first causes cells to lose function, starting with a loss of electrical activity in neurons. As the duration of ischemia extends beyond 30 minutes, cells begin to die after failure of vital functions such as membrane ion pumps (Bell, Symon et al. 1985, Lipton 1999). This results in a core of dead tissue surrounded by cells having lost their electrical activity but not yet their other functions, dubbed the penumbra. The extent and duration of penumbral tissue is highly variable between individuals, but can be found up to 16 hours after stroke onset (Marchal, Beaudouin et al. 1996).

This presents a number of therapeutic opportunities. Reperfusion allows prevention of further damage to the outer area, and preservation of penumbral tissue integrity, while neuroprotective therapies are aimed at preventing neuronal cell death within the penumbra. However the only potential method of restoring the lost core is cell replacement therapy (**Figure 1.1**).

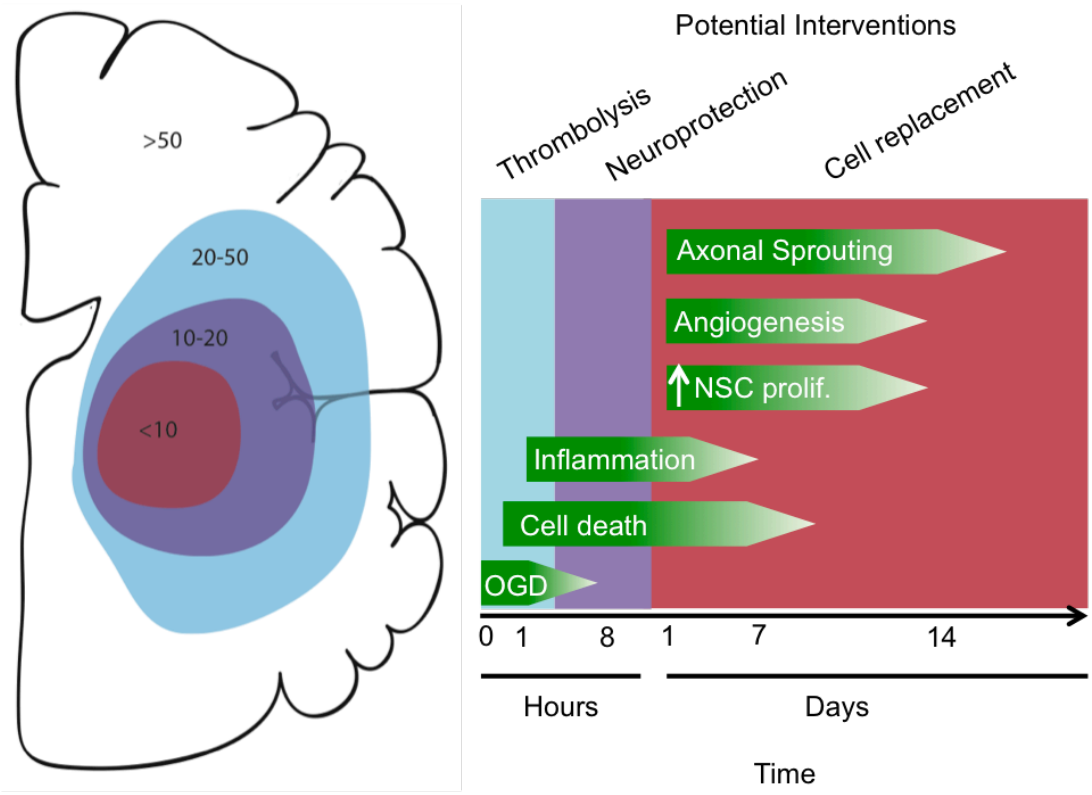

Figure 1.1 Time course of damage and potential interventions in ischemic stroke. The blue area represents "at risk" tissue, salvageable by reperfusion; purple represent the penumbra, the target of neuroprotective therapies; and red represents the core of the lesion and focus of cell replacement therapy. The numbers on the left represent approximate cerebral blood flow in ml/100g/min based on Moustafa and Baron (2008).

In adult humans, the central nervous system (CNS) has the most limited capacity for self-repair, and is well behind other tissues in its ability to recover from injury. However, there are a number of endogenous repair mechanisms initiated in response to stroke that underlie natural recovery. Neurogenesis, angiogenesis, and axonal sprouting collectively bring about a degree of repair and functional recovery after stroke.

Neurogenesis occurs in the subventricular zone (SVZ) of the lateral ventricle throughout the life of adult mammals (Alvarez-Buylla, Herrera et al. 2000). It is transiently upregulated from two days after middle cerebral artery occlusion (MCAO) in adult rats and persists for two weeks, reaching a maximum at 4-7 days (Zhang, Zhang et al. 2008). These cells have been shown to migrate to the ischemic boundary and express markers of developing and mature neurons (Arvidsson, Collin et al. 2002). Upregulation of neurogenesis after stroke has also been shown in elderly human stroke patients (Minger, Ekonomou et al. 2007). This appears to be coupled to angiogenesis (Leventhal, Rafii et al. 1999). Endothelial cell proliferation all but ceases under healthy conditions, with a turnover rate of approximately three years in the adult rodent brain (Robertson, Du Bois et al.

1985). However, angiogenesis is upregulated after stroke, with higher blood vessel counts correlating with longer patient survival (Krupinski, Kaluza et al. 1994). Endothelial cells additionally provide factors that stimulate self-renewal of neural stem cells (Shen, Goderie et al. 2004), and neuroblasts have been shown to migrate along blood vessels (Thored, Wood et al. 2007).

In traumatic CNS injuries, expression of proteins associated with inhibition of axonal growth is upregulated (Hunt, Coffin et al. 2003), creating an environment that is non-permissive for neuronal growth. However, in stroke the glial scar forms in the region of high apoptotic cell death closely bordering the infarct, which contains both inhibitory and growth-promoting molecules. But there is also a large region of peri-infarct tissue that has high levels of growth-promoting molecules and low levels of inhibitory molecules (Carmichael, Archibeque et al. 2005). It is in this area that a high axonal sprouting response is observed (Carmichael, Wei et al. 2001, Li, Overman et al. 2010).

Knowledge of the pathophysiology of stroke and its endogenous repair mechanisms has presented researchers with two main therapeutic strategies. The first is to supply drugs to target ongoing processes, such as promoting angiogenesis or preventing apoptosis in the penumbra. The second is to deliver cells, which may both supply a cocktail of growth factors to damaged tissue and serve as potential replacements for lost cells.

1.1.1 Drug delivery and biomaterials

Drug delivery targets ongoing processes, aiming either to prevent those that are thought to be detrimental, or enhance endogenous repair mechanisms.

Excitotoxicity can be attenuated using the NMDA (N-methyl-D-aspartate) antagonist memantine, which has been shown to improve behavioural outcome (Liu, Lin et al. 2009, Lopez-Valdes, Clarkson et al. 2014). There are many growth factors that are thought to enhance stroke recovery through a variety of mechanisms. Vascular endothelial growth factor (VEGF) is known to increase angiogenesis (Zhang, Zhang et al. 2000), Basic fibroblast growth factor (bFGF/FGF2) stimulates growth and proliferation of endothelial cells (Sahni, Sporn et al. 1999), and glial-derived neurotrophic factor (GDNF) and brain-derived neurotrophic factor (BDNF) have shown strong neuroprotective effects (Kurozumi, Nakamura et al. 2005). Stromal cell-derived factor 1 (SDF-1) is

a chemo attractant and attracts immune elements and progenitor cells (Fan, Shen et al. 2010), and thrombospondin has been shown to mediate synaptogenesis (Liauw, Hoang et al. 2008). However, most compounds delivered systemically suffer from a poor BBB penetration, compounds being quickly metabolized, and potential significant side-effects due to drugs affecting other organ systems (Dirnagl 2006, Ciofani, Raffa et al. 2008). Therefore many groups have looked into combination with biomaterials for delivery. Studies have shown that some growth factors are more effective when anchored to a biomaterial than when available in solution. Sahni *et al.* (1999) found higher proliferation of endothelial cells in the presence of bFGF attached to fibrinogen than in the presence of bFGF in solution. Intra-ventricular delivery of Nerve growth factor (NGF) within liposomes was shown to provide significantly higher tissue concentration of NGF then when delivered as a solution (Luk, Chen et al. 2004). NGF was also shown to have a larger effect on axon elongation in vitro when anchored to poly(dimethyl siloxane) (PDMS) than in solution (Gomez, Lu et al. 2007). Superoxide dismutase, a free radical scavenger, can be incorporated into biodegradable poly(D,L-lactide-co-glycolide) nanoparticles and achieve a 65% reduction in lesion volume, whereas the same dose in solution only achieved a 25% decrease (Reddy and Labhasetwar 2009).

It therefore seems that biomaterials play a vital role here. The chemistry behind release profiles of different biomaterials is now very advanced, and the time course of release can be carefully controlled in vitro (White, Kirby et al. 2013). However, this release may be much more difficult to control in a poorly characterized environment. Although *in vitro* efforts are in progress to establish how factors found within the ischemic environment influence release of compounds at physiologically relevant doses (Kurtoglu, Navath et al. 2009), the complexity of this environment is easily underestimated. Cytokines are released not only in response to the stroke, but potentially also in response to the biomaterials themselves. The environment also changes over time from a tissue mostly retaining its extracellular matrix and integrity, and possibly limiting the spread of nanoparticles (Klose, Laprais et al. 2009) through macrophage infiltration and debris removal to a fluid-filled cavity. It is likely that materials will degenerate differently within this evolving environment. Time-consuming in vivo studies might therefore be required to establish biodegradation profiles and associated factor release, as well as the half life of the released product. Degradation characteristics and drug availability could therefore be difficult to estimate.

Despite the hopeful preclinical results, more than 49 neuroprotective agents were studied over more than 114 clinical trials in the 20th century, and none produced a significant therapeutic effect (Kidwell, Liebeskind et al. 2001). This has been attributed to a number of factors causing a discrepancy between clinical and preclinical trials, such as the time window and duration of drug administration, patient selection criteria, target tissue and outcome measures (Gladstone, Black et al. 2002).

Gene delivery could be an important avenue of treatment for stroke, as it enables steady release of protein directly at the site without having to transport large amounts across the BBB. Most gene therapy studies for stroke use an intra-cerebral injection (Badin, Modo et al. 2009). These injections, however, distribute differentially across the brain parenchyma and are known to result in variable expression. Virus-sized particles can improve the biodistribution of therapeutic genes in the CNS (Chen, Hoffer et al. 2005). Disulphide bond-based polypeptides are becoming more commonly used as vectors, as their cytoplasm-induced reductive response facilitates the release of nucleic acids, thereby increasing transfection efficiency (Kim, Jeong et al. 2009, Kim, Lee et al. 2010). It is important to note that gene therapy can be used not only to target diseased cells with survival factors, but also remote regions to support diaschisis, i.e. neuronal plasticity that facilitates recovery (Lim, Airavaara et al. 2010). Reducible poly(oligo-d-arginines) (rPOA) can act as a carrier of the heme oxygenase-1 (HO-1) gene to decrease apoptosis (Hyun, Won et al. 2010). Both strategies (i.e. decreasing apoptosis and inducing plasticity) have been demonstrated to reduce the impact of stroke. One of the most exciting developments for gene therapy, however, would be the conversion of astrocytes in the glial scar into functional neurons (Heinrich, Blum et al. 2010).

Most commonly, a combination of gene- and cell-based therapy is envisaged to improve outcome after stroke. As viral vectors will generally indiscriminately transfect host cells where injected, transplanted cells can home into areas of damage and provide a flexible gene therapy approach. Cells overexpressing various growth factors have been shown to enhance recovery from stroke compared to unmodified cells (Kim 2004, Zhu, Zhou et al. 2004, Kurozumi, Nakamura et al. 2005, Lee, Lim et al. 2010).

1.1.2 Cell Therapy

Stem cell therapy is proving to be a promising area of research for stroke, with a large number of clinical trials now underway. The majority of these trials involve adult stem cells such as mesenchymal stem cells, CD34+ hematopoietic progenitors or cord blood stem cells administered systemically, and only one targeting intracerebral injection of neural stem cells (Clinicaltrials.govKondziolka, Wechsler et al. 2000, Bang, Lee et al. 2005, Kondziolka, Steinberg et al. 2005). These trials aim to implement efficacy previously demonstrated in animal studies (Borlongan, Tajima et al. 1998, Stroemer, Patel et al. 2009, Wakabayashi, Nagai et al. 2010), but so far no robust clinical efficacy has been demonstrated as most trials completed to date are still within the safety phase.

Adult stem cells have gained popularity compared to embryonic and fetal stem cell sources. This is due in part to reduced ethical concerns surrounding their use, but also to their safety profile. With reduced risk of oncogenesis or aberrant differentiation, and with their survival being mostly transient and peripheral, the inherent risk to patients is significantly lower.

Transplanted stem cells naturally release a cocktail of growth factors (or can be engineered to express additional factors), and can thereby provide a localised delivery of factors mentioned above and facilitate recovery through the bystander effect. Neural stem cells additionally have the potential to directly repair damaged tissue through incorporation into circuitry. At present it is unlikely that efficacy of cell transplants is due to a replacement of lost cells or tissues, but instead behavioural improvements are generally ascribed to beneficial effects exerted on the host cells (Jiang, Zhang et al. 2006). Putative mediators of recovery include regional neuroprotection, neuronal plasticity, neurogenesis and angiogenesis (Shen, Li et al. 2010). Transplantation of endothelial cells into the stroke-damaged brain reduces the size of infarction and promotes behavioural recovery (Fan, Shen et al. 2010, Ishikawa, Tajiri et al. 2013). Not only do these endothelial cells improve vascular supply, but they also deliver growth factors that are beneficial to the survival of neuronal cells (Moubarik, Guillet et al. 2011). Beneficial effects mediated through the vasculature are also thought to underpin improvements associated with intravascular infusion or intraparenchymal injection to deliver non-neuronal cells (e.g. bone marrow stem cells, umbilical cord cells). These cells typically exhibit low brain penetration and survival. However, even neural stem cells (NSCs) vary widely in their survival, with functional recovery being reported even in the

absence of significant transplant survival (Saporta, Borlongan et al. 1999). Importantly, NSCs implanted into the lesion cavity exhibit poor survival and migrate into existing tissue, rather than regenerating the lost tissue (Buhnemann, Scholz et al. 2006). This is significantly different from fetal tissue grafts implanted into the lesion cavity. In addition to neural stem cells, fetal tissue grafts contain endothelial cells, microglia, extracellular matrix and partially differentiated cells. Fetal tissue transplants therefore form a tissue clump within the cavity that poorly integrates with the host brain. Still, this "tissue clump" survives with the formation of some axonal connections, as well as an integration of blood vessels (Grabowski, Johansson et al. 1995). Survival of fetal grafts, in contrast to NSCs, following transplantation may be attributed to the presence of a complex microenvironment composed of extracellular matrix, stromal cells, and soluble factors that support the fetal progenitors after delivery. This highlights the need for biomaterials or other trophic support to deliver, support and improve therapeutic interventions is essential to limit the impact of stroke or to replace lost tissue through tissue engineering.

1.1.3 Tissue engineering

In situ tissue engineering is a further development of cell therapy (Yu and Morshead 2011). The primary aim in the context of stroke is to generate de novo tissue that could integrate into neural networks and contribute to recovery of function. Additionally, however, the lesion cavity provides an opportunity for delivery of a much higher dose of therapeutics directly to the site of injury without increasing damage to healthy tissue. In order to generate new tissue, not only will implanted cells need to remain and survive within the lesion cavity, but there is also a requirement for a vascular network and site-appropriate differentiation, as well as integration with the host brain tissue. Growth factors can be secreted from biomaterials to guide these processes (Lam, Patel et al. 2010). However, the number of processes involved is staggering and dynamic. Similar processes are well described in both mammalian development and invertebrate regeneration (Tanaka and Ferretti 2009). However the unique situation of mammalian brain regeneration will require an equally unique set of processes to ensure that an appropriate tissue forms. Although some processes will be similar to those seen in development (Cramer and Chopp 2000), it is likely that they will be orchestrated in a different way, with sequence alteration and some entirely different processes.

The simplest approach to enhance the survival of transplanted cells within the lesion cavity is to provide some structural support. A wide variety of biomaterials appear to be compatible with neural stem cells (i.e. allow survival and differentiation) (Thonhoff, Lou et al. 2008), but long-term testing under biodegradable conditions are required to establish the influence degraded scaffold components exert on cellular fate. Intra-lesion transplantation of neural stem cells with biomaterials can lead to the formation of a primitive neural tissue in the cavity as support materials degrade (Park, Teng et al. 2002, Bible, Chau et al. 2009). Hydrogel support significantly increases survival of neural progenitors within the lesion cavity (Zhong, Chan et al. 2010). It remains unclear if these approaches will translate into improved efficacy, however transplantation of neural stem cells on polymer scaffolds has been shown to improve recovery after traumatic injury of the spinal cord (Teng, Lavik et al. 2002, Olson, Rooney et al. 2009, Chen, Hu et al. 2010).

Although structural support appears essential to retain NSCs within a lesion cavity, it is unlikely that this will be sufficient to produce behavioural recovery or tissue regeneration. A demonstration of functional *de novo* tissue is a much more challenging aim. For instance, even if NSCs establish connections between themselves, they require the supply of nutrients through blood vessels. Unless an efficient and sufficient vascular supply can be established, it is unlikely that NSCs will prosper. Co-transplantation of endothelial and neural stem cells, as well as *in vitro* pre-formed neurovascular units, could overcome this issue. A controlled factor release from biomaterials is likely to be required though to ensure a concerted response and integration with the host brain. For example, Saif et al. (2010) have shown that a scaffold producing VEGF, Hepatocyte Growth Factor and angiopoietin-1 enhanced neovascularization in hind limb ischemia compared to cell therapy alone. Bible, Qutachi et al. (2012) showed recruitment of endothelial cells to the stroke lesion after co-transplantation of NSCs with VEGF-releasing microparticles. A further factor to consider is the site-appropriate differentiation of transplanted cells. This would be particularly important when transplanting directly into the lesion. Although relevant differentiation cues may be present at the periphery of the lesion, they are unlikely to be present in the core of the neuro-scaffolding. Small synthetic molecules can, however, be used to promote the striatal differentiation of human neural stem cells (El Akabawy, Martinez-Medina et al. 2011). An *in vivo* directed differentiation is therefore conceivable. Nevertheless, the logistics in combining neural stem cells with biomaterials is considerable and requires detailed protocols that can be easily

transferred between different sites. Success will also heavily depend on novel non-invasive imaging approaches that allow transplantation at an appropriate time point into a suitable site (Bible, Chau et al. 2009). Where the aim is to fill the lesion cavity with material and/or cells, the ECF currently occupying the lesion must also be taken into account, and potentially drained to avoid detrimental increases in intracranial pressure (Massensini, Medberry et al. 2014).

1.2 Identifying grafted cells

As cell therapy moves forward, elucidation of the therapeutic mechanisms relies on the reliable identification of transplanted cells within host tissue. Not only is the location of the cells indicative of their function, but also allows co-localisation with phenotypic markers to ascertain functional processes. Identification techniques must avoid false positives, false negatives and observer effects, all of which can lead to misguided conclusions regarding cell fate and effects.

False positive refers to the errant identification of a host cell as a transplanted cell, and can occur due to leakage of labels, or background signal (**Figure 1.2**B). In the context of intracerebral transplantation, false positive identification can result in an overestimation of surviving cells, and erroneous conclusions regarding their fate. The identified cell may be a neuron that is clearly integrated into host tissue, leading the investigator to conclude that the therapeutic mechanism of the transplanted cells is via cell replacement. However, this result could also be explained by label leakage into host cells, and transplanted cells may not have integrated, or indeed not survived.

False negative refers to errant identification of transplanted cells as host cells (**Figure 1.2**C). This can be due to a <100% presence of the marker in the transplanted cell population, or to later loss through label breakdown or dilution or changes in cell phenotype, and results in underestimation of transplant survival. Depending on the type of marker used, an identification bias may also be introduced, skewing the sample of cells from which the therapeutic mechanism is deduced. For example, using species specific nestin expression to identify xenotransplanted neural stem cells may later exclude cells that have differentiated into neurons and downregulated nestin expression. This could lead to conclusions that transplanted cells did not differentiate when this may not be the case.

The observer effect refers to the term coined in physics where the act of observing a system influences its behaviour. By applying labels to transplanted cells for identification purposes, the biology of the cells and therefore their therapeutic effect, may be significantly altered (**Figure 1.2**D). Labels have been shown to affect cell biology in vitro (Lehner, Sandner et al. 2011), and also their therapeutic efficacy in vivo (Modo, Beech et al. 2009).

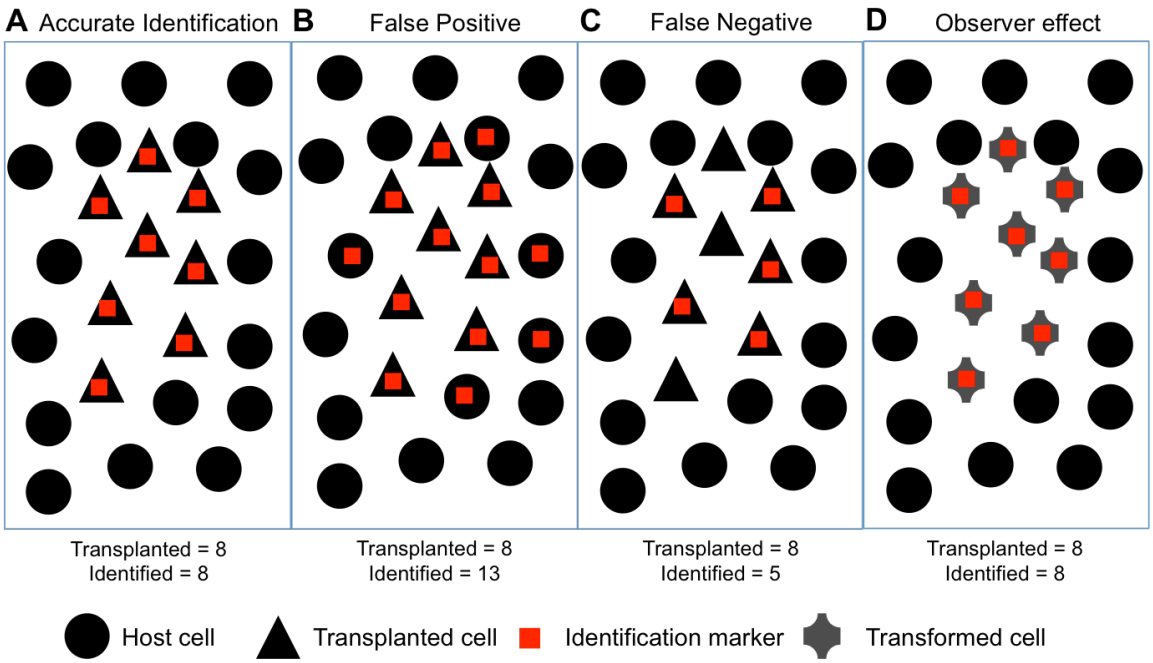

Figure 1.2 Considerations in marker selection for reliable cell identification. Accurate identification identifies only transplanted cells, and does not affect their biology (A). Presence of the identification marker in host cells generates false positives (B), whereas absence of the marker from transplanted cells generates false negatives (C). The observer effect refers to an effect of the identification marker on the biology of transplanted cells (D).

1.2.1 Histological visualisation of transplanted cells

Histological techniques offer unparalleled resolution, and the opportunity to combine cell identification with antibody labeling of relevant biological molecules. This is therefore the technique of choice to look at cell differentiation, receptor expression, immune response and a host of other processes. It has been widely used over a number of decades and is therefore well trusted, although this can at times leave the door open for insufficient rigour and cross validation.

There are many types of optical label, but all can be broadly categorized by their intracellular localisation. This gives three main categories – nuclear, cytoplasmic and membrane bound. The localisation of the dye affects not only the cell's appearance and ease of identification, but also any potential cellular effects.

1.2.1.1 Immunohistochemical techniques

Using endogenous characteristics of the transplanted cells is a very attractive option as it requires no interference with the cells prior to transplantation, thereby eliminating observer effects, and is often highly accurate and reliable. A common example is the use of species specific antibodies.

Human cells are often transplanted into rodent models in pre-clinical studies, and can be identified by human-specific antibodies such as human nuclear antigen (HNA) and Ku80 (STEM101) (Smith, Stroemer et al. 2011, El-Akabawy, Rattray et al. 2012). This of course only works in a xenograft situation. Additionally, techniques such as in situ hybridization (ISH) allow separation on the basis of genomic DNA, such as an immortalisation construct in the context of cell line transplants, or the presence of a Y chromosome to allow gender distinction. This can potentially be used even in an allograft scenario, but does of course exclude autograft.

BrdU (5-bromo-2'-deoxyuridine) is a thymidine analogue, which is incorporated into DNA in place of thymidine during DNA synthesis and can later be detected using immunohistochemistry. It has been used for identification of grafted cells since the '80s (Brown and Stanfield 1989). There are other thymidine analogues using alternate halogens such as Chlorine (CldU) or Iodine (IdU), but BrdU remains the most widely used, and has been shown to be more sensitive (Leuner, Glasper et al. 2009). Although the tight incorporation of BrdU into DNA results in a lower propensity for leakage per se, cell death results in the release of BrdU into surrounding tissue, and it has been shown to be transferred to host cells (Burns, Ortiz-Gonzalez et al. 2006). The addition of BrdU to cells prior to transplantation additionally re-introduces the potential for observer effects since it has been shown to affect cell biology (Caldwell, He et al. 2005, Lehner, Sandner et al. 2011).

1.2.1.2 Nuclear markers

Nuclear labels include those that bind to DNA such as DAPI (4',6-diamidino-2-phenylindole) and Hoechst, and reporter genes such as GFP and mCherry.

DAPI and Hoechst are most commonly used as nuclear counterstains for fluorescence histology due to their bright fluorescence, high efficiency and ease of labeling. Both are also used to label live cells for identification post-transplant (Elmadbouh, Chen et al. 2005, Rossignol, Boyer et al. 2011) but have been criticised by some for their propensity to leak into host cells (Iwashita, Crang et al. 2000, Castanheira, Torquetti et al. 2009). Additionally, Hoechst has been shown to be both toxic (Durand and Olive 1982, Singh, Dwarakanath et al. 2005) and non-toxic to cells (Hubbard, Gut et al. 2012), showing that its cytotoxicity is highly dependent on conditions and assays used. Both DAPI and Hoechst bind to AT rich regions of DNA (Vega, Garcia Saez et al. 1994), which is where many transcription factors bind (Privalov, Dragan et al. 2007). Hoechst has been shown to upregulate the pro-survival factor Survivin, and in doing so attenuate the effects of its own

cytotoxicity (Wu, Apontes et al. 2007). Transcription factors such as Mash1, which plays a role in neural commitment, also bind to AT rich regions (Ghysen, Dambly-Chaudiere et al. 1993), but population level effects on cell differentiation have not been shown.

Reporter genes refers to the insertion of a gene into the cells such that when it is transcribed, the product will be visible to the selected imaging modality. The most well-known example is probably Green Fluorescence Protein (GFP) which, as the name suggests, is fluorescent and therefore visible using fluorescence microscopy. This mechanism means that cells are only detected when viable and producing protein, and that the product cannot leak into host cells. This reduces the likelihood of false positives, but the similarity of the fluorescence to autofluorescence can still cause cases of mistaken identity (Spitzer, Sammons et al. 2011, Molcanyi, Bosche et al. 2013). Protein expression is often highly variable across the cell population, and gene silencing can occur after transplantation, depending on the promoter used, leading to a loss of fluorescence over time. Expression of a reporter gene can also induce marked changes in cell biology (Huang, Aramburu et al. 2000, Martinez-Serrano, Villa et al. 2000), and some concern has been raised over potential immunogenicity of the proteins themselves (Bubnic, Nagy et al. 2005). However, reporter genes have great potential, and improvements in the design of promoters as well as cell lines with safe insertion sites mean that many of these problems may be overcome in the future.

1.2.1.3 Cytoplasmic labels

The most well known cytoplasmic label is probably carboxyfluorescein succinimidyl ester (CFSE). It is applied to cells as the highly membrane permeant compound carboxyfluorescein diacetate succinimidyl ester (CFDASE), which is then cleaved within the cell to give CFSE, a much less permeant molecule which is fluorescent and can be coupled to intracellular molecules to achieve stable labeling (Parish 1999). It is particularly well suited to labeling lymphocytes, and quantifying their proliferation, although reports of its cytotoxicity vary (Last'ovicka, Budinsky et al. 2009, Quah and Parish 2010). Labeling of preadipocytes showed low labeling efficiency and high cell toxicity (Hemmrich, Meersch et al. 2006). CFSE is not widely used for intracerebral transplantation. Only two incidences of labeling neural cells is available in the literature, and little analysis of label effects or leakage were performed (Li, Dancausse et al. 2003, Wang, Schwindt et al. 2009).

Quantum dots are a newer technology, and represent a very broad category of particles. The defining characteristic is that they are semiconductor nanoparticles whose absorption/emission

wavelengths can be tuned via alteration of the size of the particle, with larger particles having longer wavelength spectra (Dabbousi, Rodriguez-Viejo et al. 1997). Their advantages include photostability, narrow emission spectra, capacity for addition of targeting moieties, and the potential to be used for in vivo tracking (Walling, Novak et al. 2009). However, their size differences can affect label uptake and retention (Seleverstov, Zabirnyk et al. 2006), and the particles can be made of and coated with a large variety of different materials (Anilkumar, Wang et al. 2011, Kuo, Chueh et al. 2011, Ryvolova, Chomoucka et al. 2011, Wang, Mo et al. 2011), each of which may alter particle effects on labeled cells (Hoshino, Hanada et al. 2011). The cell type and even differentiation state could also be important. For example, in a neuronally differentiating, raphe-derived cell line, fluorescent microspheres were shown to be toxic to differentiated cells, but not to the proliferating progenitors (Onifer, White et al. 1993).

1.2.1.4 Membrane dyes

Lipophilic dyes, such as PKH26 and DiR (3,3,3',3' tetramethylindotricarbocyanine iodide), incorporate into lipid regions of the cell membrane. They give a very bright fluorescence, although it is somewhat susceptible to bleaching, and are very simple to use. However, the membrane is constantly turned over as sections are used to form endosomes and exosomes, with some phagocytes turning over their whole membrane in 30min (Gheber and Edidin 1999). This inevitably leads to some leakage of the dye, and in one transplantation experiment, 88% of DiR labeling was shown to be due to host microglia rather than transplanted cells (Lassailly, Griessinger et al. 2010). However, this was after intravenous injection of cells, and little has been reported on the label's behaviour in the context of transplantation into brain tissue. However, its use as a retrograde and anterograde neuronal tracer has been investigated (Kawaguchi, Katsuyama et al. 2010)

1.2.2 Non-invasive imaging

Histology offers many advantages in terms of its resolution and ability to assess the presence of proteins in host tissue and transplanted cells. For example, caspase 3 can be used to assess apoptosis (Chen, Ma et al. 2015), and phenotype markers can assess cell differentiation and endothelial cell infiltration. However, its very significant drawback is the need to harvest and process tissue, meaning that looking at transplanted cells over time requires numerous cohorts of animals. This of course introduces ethical considerations, as well as monetary and logistical

concerns, but importantly means that one is not in fact observing the cells “over time”. This is particularly important in highly variable models, such as MCAO (Smith, Stroemer et al. 2011) where there are several “layers” of variability, beginning with lesion size and topology and extending through cell delivery and survival, and immune response. Therefore, in order to obtain a true picture of the overall process and the factors affecting it, better ways of monitoring cells in vivo are required. There are now a wide variety of imaging techniques available, the advantages and disadvantages of which (for cell tracking) are summarised in **Table 1.1**.

The ideal in vivo imaging technique would allow reliable identification of transplanted cells, as described above, and also provide anatomical information, so that the cells’ location, survival and movement relative to the lesion can be accurately determined, and also so that changes in the lesion itself can be analysed, such as lesion volume. Although lesion volume alone is not necessarily a reliable measure of therapeutic outcome, it remains a useful measure when elucidating the therapeutic mechanism of transplanted cells. In order to measure the therapeutic effect in a way that is meaningful in terms of predicting its clinical efficacy, behavioural measures are essential, since regaining motor and cognitive functions is the primary clinical goal.

1.2.2.1 Optical Imaging

Light is commonly used in histological techniques, but in vivo it suffers from a high level of scatter. The use of longer wavelengths of light, such as red and near infra red (NIR) reduce this problem, but the main limitation of light based imaging remains tissue penetration. This is a particular problem in the brain, where tissue is fixed within the skull, so penetration of two very different tissue types would be required for truly non-invasive imaging. The main light-based techniques used in rodent stroke models are Bioluminescence and two-photon microscopy.

Two photon microscopy (TPM) is most commonly used following a craniotomy, where a portion of the skull is removed to allow direct access to brain tissue. This enables imaging up to 300-500μm below dura using GFP (Kozai, Vazquez et al. 2012). TPM is useful for imaging immediate inflammatory processes (Hasenberg, Hasenberg et al. 2015), as well as angiogenesis and BBB integrity (Masamoto, Takuwa et al. 2013) but due to the required craniotomy or skull thinning, long term repeated imaging is not usually performed using this technique. In MCAO, the location of the lesion is normally at least 4-5mm below dura, which is out of range for this method (Kerr and Denk 2008).

Modality	Description	Advantages	Disadvantages
Histology	Post mortem tissue is examined by microscopy	Extremely high resolution. Ability to assess presence of a wide variety of different proteins using immunohistochemistry	Applicable only post mortem
Two photon in vivo microscopy	Living tissue is examined by 2-photon microscopy, often utilising NIR fluorescence	High resolution	Limited tissue depth; Use in brain imaging requires craniotomy
Bioluminescence	Cells with bioluminescent reporter emit fluorescence	Also report on cell viability, as ATP is required for fluorescence emission.	Little anatomical information
PET Positron Emission Tomography	Positron emitting radionuclide tracers are incorporated into biological molecules of interest. Detection of gamma rays reveals areas of high tracer concentration	High sensitivity Glucose analogue FDG can indicate metabolic activity of tissue	Little anatomical information; often combined with CT or MRI Short half life of radionuclides Ionising radiation
SPECT Single photon emission computed tomography	Gamma emitting radionuclides are incorporated into targeting molecules. Detection of gamma rays reveals areas of high tracer concentration	Very high sensitivity	Low resolution Short half life of radionuclides Ionising radiation
X-ray CT X-ray Computed Tomography	X rays are used to obtain 2D radiographic images, which are processed using digital geometry processing to create a 3D tomographic image	Rich anatomical information, particularly for bony structures and cancer detection; Short imaging time	Limited anatomical information for soft tissues Ionising radiation
MRI Magnetic Resonance Imaging	Magnetic particles are detected using resonance. Water molecules are most often used	Rich anatomical information - high resolution with very high soft tissue detail	Low sensitivity

Table 1.1 Advantages and disadvantages of different imaging modalities

Bioluminescence (BLI) refers to the use of luciferase enzymes that catalyse light-emitting reactions as reporter genes in transplanted cells. There are a number of luciferases available from different species, which have different emission spectra affecting their in vivo utility (Zhao, Doyle et al. 2005). Firefly luciferase (fluc) is the most commonly used, due to its longer wavelength and consequent reduced scatter in vivo. In order to detect transplanted cells expressing luciferase, luciferin is then administered to the animal, and luciferase catalyses the reaction between luciferin, adenosine triphosphate (ATP) and oxygen, during which light is released and detected (**Figure 1.3**). For a given fluc+ cell line, a standard curve can be set up to give a quantitative readout of cell number from a given readout of light emission (Bernau, Lewis et al. 2014).

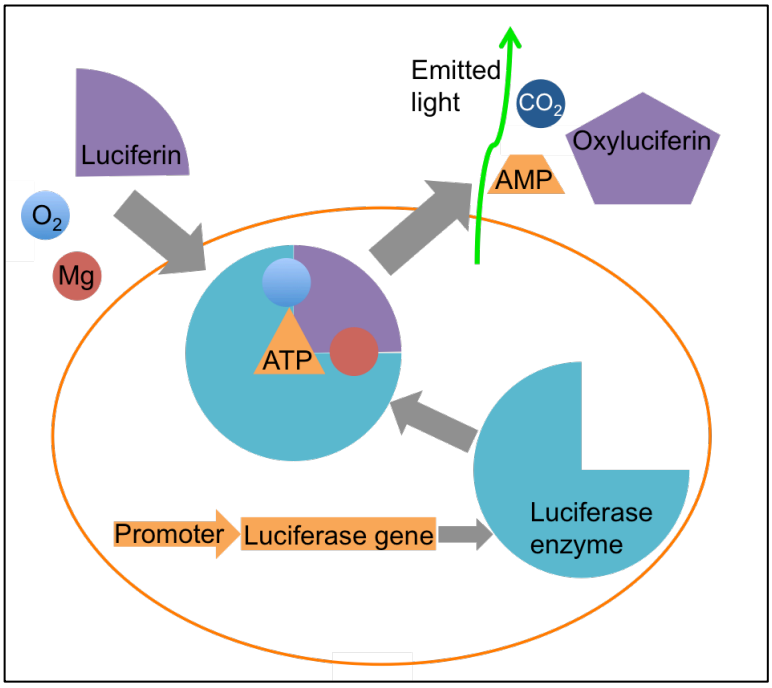

Figure 1.3 Mechanism of BLI. Luciferase expressed by modified cells catalyses the conversion of luciferin to oxyluciferin in the presence of ATP, oxygen and magnesium.

BLI is a very attractive option for cell tracking due to the relatively low cost of equipment (Inoue, Kiryu et al. 2009) and ability to report on cell viability due to the requirement for ATP and oxygen. In vivo detection in the rat striatum has been demonstrated at 9×10^5 transplanted cells over 12 weeks, with a detection threshold between 9×10^3 and 9×10^4 cells (Bernau, Lewis et al. 2014). Imaging endogenous NSCs, where luciferase expression is under the control of the nestin promoter in a transgenic mouse has been demonstrated at 2,000 NSCs (Vandeputte, Reumers et

al. 2014). The differences here may be due to a number of factors such as relative tissue depth in the two species, the level of luciferase expression, and availability of luciferin and oxygen from the blood, which may be higher for the well-vascularised SVZ compared to newly grafted cells. This may be an additional consideration for transplantation into a hypoxic environment. Assessing the relationship between oxygen/luciferin availability and light emission in vitro way well be an essential first step before utilising this method in an environment such as the lesion cavity. However, BLI has been successfully used to assess the temporal expression profile of VEGF2 after stroke in a transgenic mouse model (Adamczak, Schneider et al. 2014), and therefore may be useful in assessing the peri infarct environment and informing the design of factor releasing scaffolds.

A third optical method with potential applications here is optogenetics, where neuronal activity is linked to light. This can either be the application of light to provoke neuronal activation through e.g. channelrhodopsin, or the activation of fluorescence in the presence of intracellular calcium through genetically encoded calcium indicators (GECIs, such as GCaMP). These techniques allow assessment of the connectivity of grafted cells to host tissue, (Byers, Lee et al. 2015, Steinbeck, Choi et al. 2015) and the use of GECIs would also allow assessment of spontaneous graft activity.

However, the need to incorporate a reporter gene has its own disadvantages for cell tracking (see section 1.2.1.2 above), and the lack of anatomical information is problematic, particularly in the context of tissue engineering. Combining bioluminescence with MRI, however, shows promise in overcoming this issue (Tennstaedt, Aswendt et al. 2013).

1.2.2.2 Nuclear Imaging

Nuclear imaging methods are based on the use of gamma or x rays, which have a very high frequency ($3 \times 10^{16} – 3 \times 10^{19}$ Hz), and as such, they carry inherent safety concerns (Zanzonico, Dauer et al. 2008). The dose received by patients in medical imaging is a very small proportion of what they are exposed to annually from background radiation, but radiographers working regularly with these modalities require protective equipment.

Nuclear imaging modalities include positron emission tomography (PET), single photon emission computed tomography (SPECT) and x-ray computed tomography (CT). PET and SPECT both

have extremely high sensitivity, but the short half life of most radioligands and the lack of anatomical information means that these have not been modalities of choice for cell tracking. However, these can be combined with MRI or CT to provide anatomical context (Gildehaus, Haasters et al. 2011), and genetically modified cells can be used to over come the short half life. Herpes Simplex Virus type 1 thymidine kinase (HSV1-tk) can be used to entrap systemically administered probes such as ^{18}F-fluoropenciclovir (^{18}F-FPCV) within genetically modified cells (Iyer, Barrio et al. 2001). However, like BLI this relies on delivery of the probe through the blood, and visualisation may therefore be hampered by cell localisation within the poorly vascularised lesion environment. [(18)F]fluorodeoxyglucose (18FDG) is a radioactive glucose analogue, which can be used to measure glucose uptake to report on tissue metabolism during a stroke (Balsara, Chapman et al. 2014) or over time through recovery (Martin, Gomez-Vallejo et al. 2013). It can also be used to report on changes in dopamine binding activity using [(11)C]raclopide (Martin, Gomez-Vallejo et al. 2013). These two techniques, when combined with CT, provide insight into stroke pathology and recovery. When combined with the HSV1-tk system to identify transplanted cells, it would be possible to asses the metabolic activity and dopamine binding of transplanted tissue, providing a wealth and specificity of information not available using other imaging techniques.

1.2.2.3 Magnetic Resonance Imaging (MRI)

MRI is a tomographic imaging technique with good spatial and temporal resolution, no tissue depth limitations and no need for ionizing radiation. It is most often tuned to ^{1}H nuclei, predominantly measuring the water protons present in all tissue. These nuclei have a property known as spin, and their movement within an electromagnetic coil creates small voltages that can be detected. Their equilibrium is disturbed by the application of a radiofrequency (RF) pulse, and the time take to return to equilibrium (relaxation) is measured. Tissue contrast is generated due to the effects of the environment on different aspects of relaxation, namely T1 and T2. In order to track transplanted cells, contrast agents are added, which affect the T1 and T2 relaxation properties of protons within the cells. Contrast agents are normally grouped as T1 or T2 agents based on which property they have the most significant effect on. However, it should be noted that these two properties are closely related, so agents will always affect both to some extent.

The most commonly used contrast agent for cell tracking is iron, either in the form of nanoparticles (super paramagnetic iron oxides, SPIOs) (Guzman, Bliss et al. 2008), or with the use of the ferritin reporter gene, which increases uptake of iron from the blood and surrounding tissue (Iordanova and Ahrens 2012). Their predominant effect is on T2 contrast, and excellent sensitivity has been achieved. They have been widely used to track migration of transplanted cells in the brain (Hoehn, Kustermann et al. 2002, Jendelova, Herynek et al. 2003, Guzman, Bliss et al. 2008, Kallur, Farr et al. 2011). However, iron is an abundant element in the body and as such a T2 hypointensity can be produced by naturally occurring phenomena such as dilated blood vessels, intracerebral bleeds, or tissue damage such as an injection tract, and these can be difficult to distinguish from transplanted cells. Infiltrating immune cells also incorporate iron from their environment and produce T2 hypointensity border regions of a stroke lesion (Vandeputte, Thomas et al. 2010). Additionally, T2 weighted images are the method of choice for assessing changes in lesion volume over time, for example using deformation based morphometry (Smith, Stroemer et al. 2011) so being able to image cells without interfering with this would be an advantage.

A second class of MRI contrast agents are dubbed T1 agents, as they produce a hyperintensity on T1-weighted MR images. The most commonly used T1 contrast agent for cell tracking is Gadolinium (Gd). It is less sensitive than iron-based contrast agents (Helm 2010), but the ability to unambiguously identify cells on T1-weighted images is a significant advantage. Gd-labeled cells show the same migratory patterns as iron labeled cells (Modo, Mellodew et al. 2004). However, despite not showing significant effects on cell biology in vitro (Brekke, Morgan et al. 2007), labeled cells had reduced therapeutic efficacy compared to those labeled with the histological label PKH26 (Modo, Beech et al. 2009).

Although MRI is most often tuned to ^{1}H nuclei, it is also possible to tune to alternate nuclei such as Fluorine-19 (^{19}F). This has the advantage that there is no background signal in the body, allowing unambiguous detection, but the sensitivity is lower still than Gd, requiring large cell numbers for detectable signal (Boehm-Sturm, Mengler et al. 2011, Bible, Dell'acqua et al. 2012).

Further applications of MRI in stroke include Blood Oxygen Level Dependent (BOLD) fMRI to observe tissue oxygenation levels (An, Liu et al. 2012), and neuronal tracing techniques such as Manganese Enhanced MRI (MEMRI) to observe changes in connectivity (van der Zijden, Wu et

al. 2007). MEMRI also offers the potential for combination with PET through the use of radioactive (52)Mn (Lewis, Graves et al. 2015, Weissler, Gebhardt et al. 2015), but care must be taken as it has been shown to be cytotoxic, and long term exposure can induce symptoms similar to Parkinson's Disease (Olanow 2004).

The main drawback of MRI is its low sensitivity. Differences between tissue must be very significant before noticeable MR contrast is observed. However, the anatomical information is highly valuable. In particular, the ability to distinguish between a fluid-filled cavity and organized tissue is of great importance in the context of tissue engineering.

Modality	Most suitable application(s) in stroke	Considerations and Limitations
Optical (TPM, BLI and optogenetics)	Imaging local inflammation, and expression of proteins of interest using transgenic animal lines	Limited tissue depth
	Imaging blood flow and angiogenesis using IV dye such as sulforhodamine	Use in brain imaging requires craniotomy
	Assessment of graft-host connectivity and spontaneous graft activity using transgenic cell line with GECI	Genetic modification of animals and/or transplanted cells required
PET-CT	Assessing metabolic activity of damaged tissue and/or transplanted cells using 18FDG	Potentially unlimited number of metabolic targets can be imaged sequentially in the same animal, using CT to co-localise
	Imaging dopamine binding in stroke damaged tissue and/or transplanted cells	Reporter gene required for cell tracking
	Tracking transplanted cells using HSV-tk	Safety concerns with the use of radioactive agents
MRI	Cell Tracking	Low sensitivity due to high background as the imaging target is predominantly water
	Assessment of changes in lesion volume and topology	fMRI requires additional hardware and software
	Detection of blood flow using BOLD-fMRI	Exogenous contrast agents may leak into surrounding tissue
	Neural tract tracing, and imaging of connectivity using MEMRI	

Table 1.2 Summarising the use of different imaging methods for different applications in stroke

1.3 Image Guided Injection

Imaging can guide cell injection in a number of ways; to select subjects, to position injections to minimise damage, and to optimise placement of injected materials on an individual basis. Subject selection for inclusion in an efficacy study is routine in clinical trials (Yoo, Pulli et al. 2011), but is not yet common practice in preclinical studies. For instance, inclusion and exclusion criteria for an efficacy study could define a minimum hyperintense area on T_2-weighted MR images. Very small lesions (e.g. <10 mm^3 in the rat) revert to isointense contrast over 14 days and should therefore be excluded if lesion volume is one of the main outcome measures. Therefore it is important to have a robust imaging paradigm to detect the evolution of the lesion (Helpern, Dereski et al. 1993, Knight, Dereski et al. 1994). A very large lesion also affects efficacy, with lesions confined to the striatum showing improved behavioural outcome after NSC transplant compared to lesions spanning striatum and cortex (Smith, Stroemer et al. 2011).

Placement of injected materials is also an important consideration. Cell injection into parenchymal tissue has been shown to produce improved behavioural outcome compared to transplantation into the ventricles (Smith, Stroemer et al. 2011). Since the lesion varies in size and location between individuals, treatment efficacy may be improved by individualising dosage and placement of cells. Accidental placement into the lesion cavity rather than parenchymal tissue is likely to reduce cell survival and efficacy. Conversely, when targeting the lesion for tissue engineering, the large volume of cells and biomaterials required to fill the lesion could cause extensive damage if injected into healthy tissue (Bible, Chau et al. 2009, Massensini, Medberry et al. 2014).

The use of image guidance for transplantation requires anatomical imaging with good contrast between soft tissue types. CT and MRI are both able to provide sufficient information, but MRI provides improved soft tissue detail, and techniques such as fluid-attenuated inversion recovery (FLAIR) and diffusion weighted imaging (DWI) allow more precise delineation of lesion cavity compared to parenchymal tissue (Bible, Dell'acqua et al. 2012).

1.4 Imaging in tissue engineering

1.4.1 Imaging Biomaterials

Some biomaterials will have relaxivity properties and can therefore be easily detected using MRI, but this inherent contrast will make it difficult to interrogate what changes occur within the lesion territory (Bible, Chau et al. 2009). Therefore a tuneable or induced contrast in biomaterials might be desirable. Incorporating contrast agents into biomaterials, such as hydrogel, can make these visible on MRI without interfering with structural T2-weighted images (Karfeld-Sulzer, Waters et al. 2011, Kim, Chun et al. 2012). The release of contrast agents from biomaterials in conjunction with the release of growth factors also potentially provides a means to monitor their distribution and release kinetics in vivo (Onuki, Jacobs et al. 2010). This provides an opportunity to understand how factors released from biomaterials interact with the host brain. Multifunctional and multi-modal materials (Yim, Seo et al. 2011) might therefore be needed to allow the simultaneous monitoring of various processes. Detection of biomaterials used to engineer tissue, however, should not interfere with the visualization of tissue formation.

1.4.2 Multiple Transplant Components

The increasing complexity of transplants for tissue engineering introduces the problem of multiple transplant components. Although one option would be to simply track “the transplant” with a single contrast mechanism, it is important to elucidate the mechanisms of each component’s contribution to the therapeutic effect. Being able to independently track one or more cell populations as well as the degradation of a biomaterial would enable much swifter and more accurate evolution of tissue engineering therapies.

1.4.3 Monitoring Tissue Formation

Only T_2-weighted MR images will be insufficient to demonstrate tissue formation (Bible, Dell'acqua et al. 2012). Conventional MR contrast agents affect ^{1}H and therefore are likely to affect T_2-weighted images, whereas novel classes of contrast agents, such as ^{19}F or chemical exchange saturation transfer (CEST), are likely to be better candidates to report on the presence of biomaterials. However, for regenerative imaging, it is even more important to be able to visualize biological processes rather than the biomaterials.

In the absence of existing tissue, there are no cues to instruct site-appropriate differentiation of implanted cells. These cues need to be delivered through biomaterials or pre-differentiation of cells (El Akabawy, Martinez-Medina et al. 2011). The molecular signature of the tissue can potentially be monitored non-invasively using magnetic resonance spectroscopy (MRS) (Manganas, Zhang et al. 2007, Loewenbruck, Fuchs et al. 2011). MRS can establish a particular metabolite profile for a given tissue, such as striatum or cortex, as these metabolites are dependent on the variety of elements contained within the tissue (Brownell, Chen et al. 2004), and they thereby provide a very general means to establish what aspects of the appropriate tissue have been regenerated (Ross, Hoang et al. 1999). For instance, MRS of the rat striatum clearly indicates the presence of GABA and glutamate (Roffman, Lipska et al. 2000), two key neurotransmitters in this neuroanatomical structure. Therefore any replacement tissue needs to demonstrate that similar levels of neurotransmitters can be generated. Additionally, MRS can report on the health of the tissue with lactate being upregulated in dying cells (Woo, Lee et al. 2010) and phosphocholine being upregulated in proliferating cells (Gillies, Barry et al. 1994). Future studies have to nevertheless demonstrate that MRS can indeed provide a reliable discrimination between these different processes.

Aims and Objectives

This project has 3 specific aims:

- To compare currently used histological labels to assess their reliability for identifying cells transplanted into the brain and determine which, if any, are suitable for use in further studies
- To assess the suitability of a novel gadolinium-gold nanoparticle for visualising transplanted cells in vivo using MRI
- To assess the potential of two paraCEST agents for independent visualisation of two cell populations in vivo

Chapter 2: Histological labels for identification of transplanted cells

2.1 Introduction

Due to its excellent resolution, suitability for probing cell phenotype and function, and relatively low cost, histology remains the most widely used method of tissue analysis. In particular, fluorescence immunohistochemistry is extremely versatile, as a number of different channels can be used to assess different cell characteristics. Being able to reliably identify transplanted cells is vital in order to establish their fate after transplantation, and thereby elucidate their therapeutic mechanisms. In xenograft studies, species-specific antibodies can be used for this purpose. However, in the context of allo- or auto-graft, or where more than one population is transplanted, it becomes necessary to add an exogenous label to grafted cells in order to identify them.

Histological labels have been used since the early 90s (Sprick 1991, Trumble and Parvin 1994), and concerns about their effects on labeled cells were raised almost immediately (Samlowski, Robertson et al. 1991). However, the majority of early studies were focused on labeling of lymphocytes, either in situ or on intravenous injection of labeled cells. Studies on intracerebral transplantation of labeled cells primarily used toxicity tests, such as Trypan Blue exclusion, to assess the effects of labels on transplanted cells, and it has only been more recently that concerns have been raised regarding their more subtle cellular effects (Lehner, Sandner et al. 2011) and leakage in vivo (Iwashita, Crang et al. 2000, Burns, Ortiz-Gonzalez et al. 2006).

However, there are a wide variety of labels available, with different methods of incorporation, which may have different effects on labeled cells, and on the label's propensity for leakage. These have not been directly compared in the same context, so it is currently difficult for investigators to make an informed choice regarding selection of a reliable label. In order to be described as reliable, a label should 1) Efficiently label all required cells, 2) Have minimal effects on the cell's biology and 3) Not be lost or diluted from transplanted cells, or transferred to host cells.

In this study, we aim to test four labels using these criteria in order to draw a direct comparison of their suitability for identifying transplanted neural stem cells. Transplantation of human neural stem cells into healthy rat brain tissue allows the use of a species-specific antibody to reliably

distinguish transplanted from host cells, allowing the comparison of its localisation with that of the labels tested in order to deduce the comparative accuracy and reliability of each label.

2.2 Methods

2.2.1 Experimental Design

Experiments were designed to investigate four major questions:

1. Are all cells labeled, or would there be false negatives?
2. Are there cellular effects of the label?
3. Is there leakage and re-uptake of the labels that would lead to false positives?
4. How reliable are labels to identify implanted cells in vivo?

Based on these questions, a flow diagram (**Figure 2.1**) can be drawn that determines the suitability of a given label to progress to the next step of testing. Multiple potentially suitable labels can therefore be compared using these steps to determine which are reliable for in vivo identification of cells. To this end, six histological labels were investigated: Fast Blue, Hoechst, BrdU, eGFP, PKH26 and Qtracker.

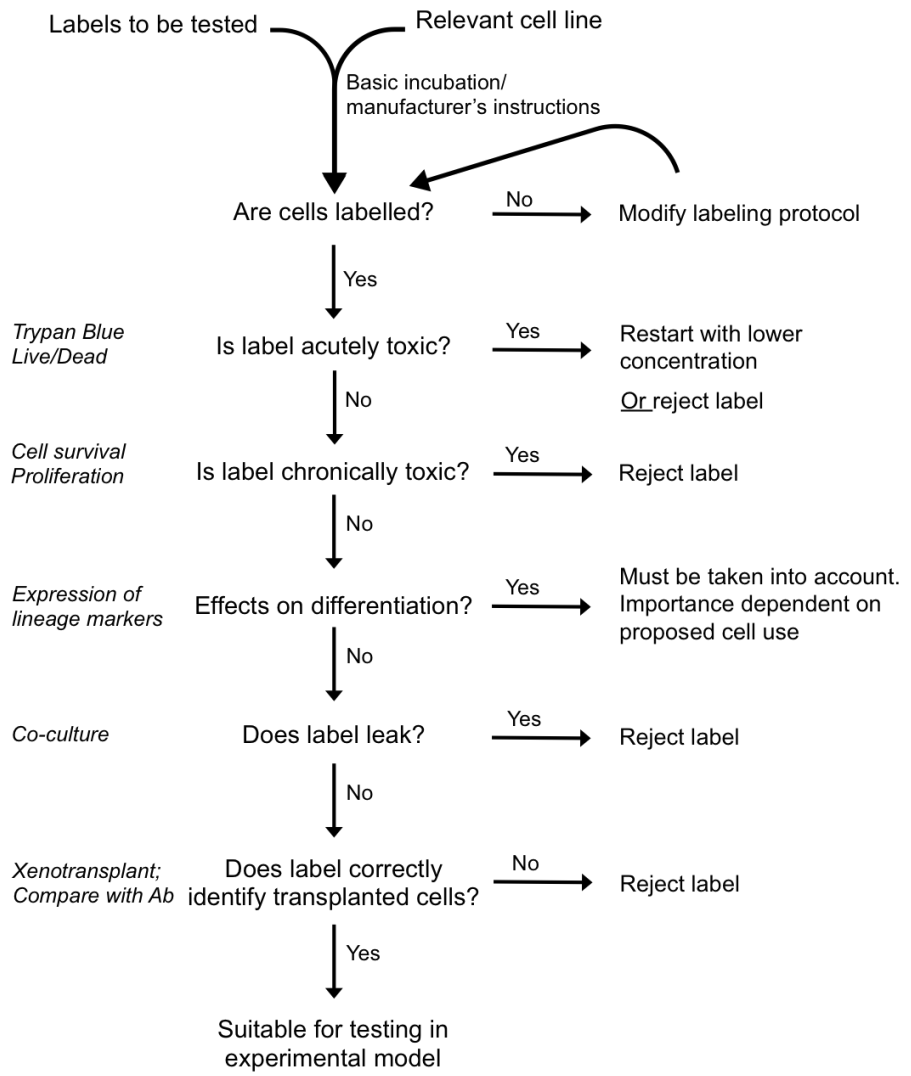

Figure 2.1. Experimental Design. Labels will undergo a battery of tests with the STROC05 neural stem cell line to determine their reliability.

The cell line selected for use is the STROC05 fetal neural stem cell line. This line is a promising candidate for tissue replacement after stroke, and has shown the capacity to form primitive neural tissue in the stroke cavity (Bible, Qutachi et al. 2012). The properties of these cells have been well characterised (El Akabawy, Martinez-Medina et al. 2011), enabling reliable detection of deviations caused by the presence of a label. Their characteristic expression of phenotypic markers before and after differentiation is shown in **Figure 2.2**A. An increased expression of GFAP, Tuj and Galc at day 7 and decreased expression of Ki67 is evident compared to day 1. The use of a human line here allows the use of species-specific (human) antibodies (**Figure 2.2**B) to identify these cells against a rat tissue background, since rat tissue does not react with these (**Figure 2.2**C). A positive control to show that these antibodies detect human cells was performed on a human hippocampus sample (**Figure 2.2**D).

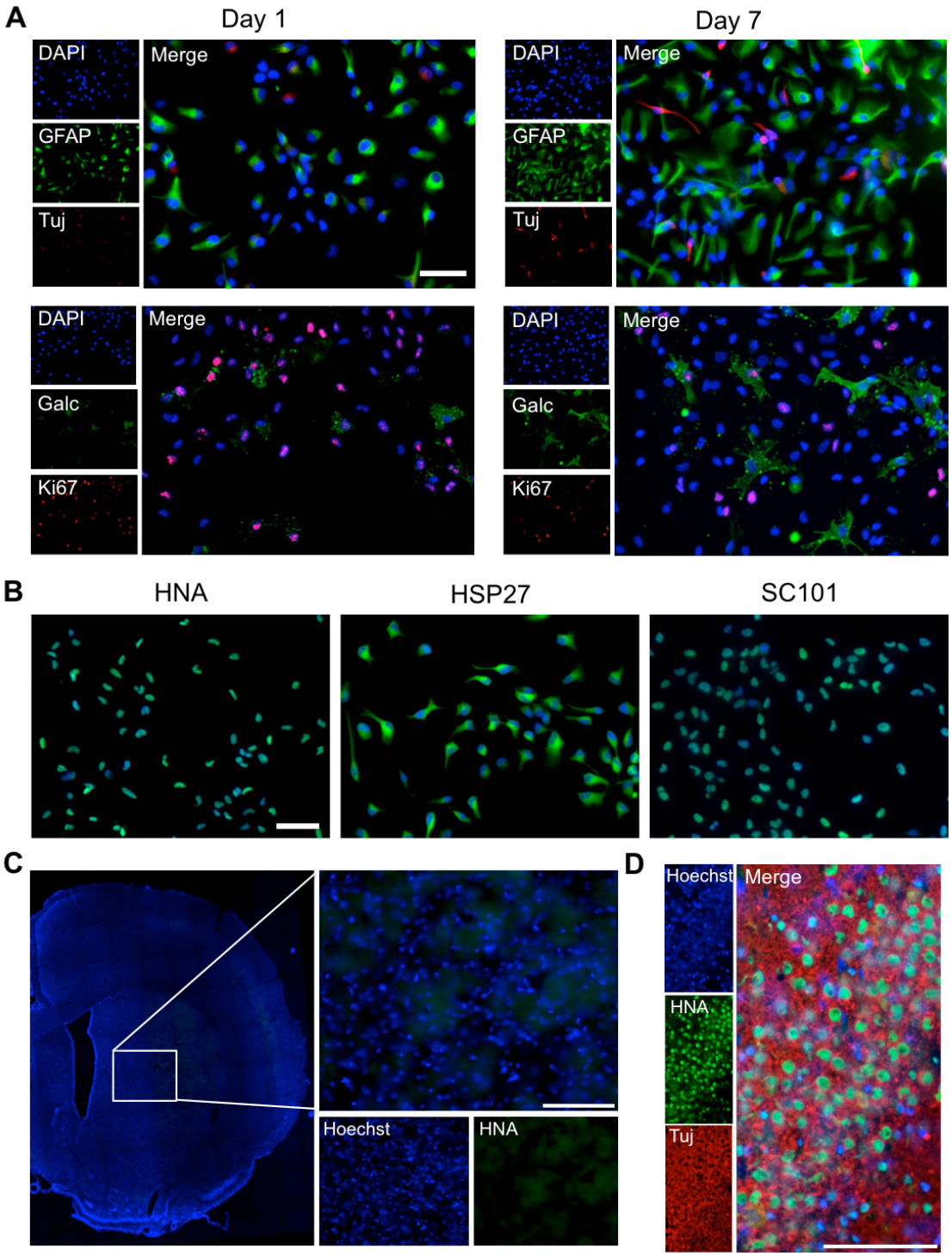

Figure 2.2. STROC05 Neural Stem Cells stained with a proliferation marker, Ki67 and markers of different cell lineages (GFAP for astrocytes, Tuj for neurons and Galc for oligodendrocytes) at day 1 and day 7 (A). STROC05 cells are positive for human specific markers HNA and SC101, and HSP27 (B). Rat tissue is negative for HNA (C) and human tissue is positive (D).

To address the questions in the flow chart above, the in vitro experiments were set up as shown in **Figure 2.3**. Specifically, after labeling, cells were tested immediately for viability. 24 hours later, extent of cell labeling and label transfer were assessed, in addition to viability (%), number of

surviving and proliferating cells, and expression of phenotypic markers. After 7 days, retention of label, survival, proliferation and phenotypic markers were measured again to establish potential delayed effects of the labeling procedure.

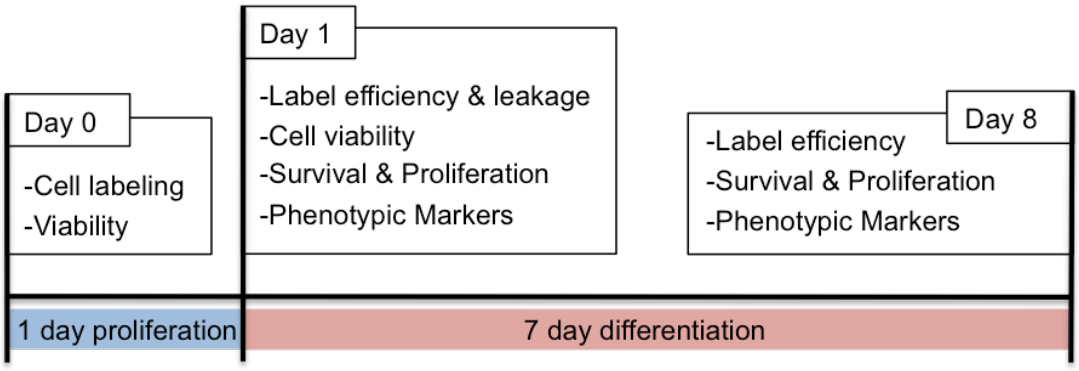

Figure 2.3. In vitro methods, showing parameters assessed at day 1 and 7.

2.2.2 Cell culture

2.2.2.1 STROC05 Cell line

The cMyc-ER^{TAM} striatal neural stem cell line STROC05 (ReNeuron) was previously described by Johansson et al. (2008). Briefly, cells isolated from the whole ganglionic eminence of a 12 week old human fetal brain were transfected with the cMyc-ER^{TAM} gene, encoded by the retroviral vector pLNCX-2 (Clontech) and transfected colonies were selected using neomycin resistance and expanded into a clonal cell line (Pollock, Stroemer et al. 2006).

STROC05 cells were grown in vitro as monolayers in T-flasks (Falcon) coated with mouse laminin (10µg/ml, Sigma L2020) for 1.5 hours at 37°C. The proliferation medium used was DMEM:F12 (Sigma D6421) supplemented as shown in **Table 2.1**, with the addition of 4-hydroxy-tamoxifen ensuring proliferation through the conditional immortalization gene. Cells were kept in a humidified-atmosphere incubator at 37°C, with 5% (v/v) CO_2, and medium was changed every 2 days. Cells were tested for mycoplasma infection regularly using the Invivogen PlasmoTest kit and found to be mycoplasma free.

Table 2.1. Components added to DMEM-F12 basal medium for STROC05 proliferation medium. For differentiation medium, bFGF, EGF and 4-hydroxy-tamoxifen were omitted.

Component	Source	Final Concentration
Human Albumin Solution	GemBio 800-121	0.03 %
Transferrin, human	Sigma T1147	100 µg/ml
Putrescine DiHCl	Sigma P5780	16.2 µg/ml
Insulin, human recomb.	Sigma I9278	5 µg/ml
L-Thyroxine (T4)	Sigma T0397	400 ng/ml
Tri-iodo-thyronine (T3)	Sigma T6397	337 ng/ml
Progesterone	Sigma P8783	60 ng/ml
L-glutamine	Sigma G7513	2 mM
Sodium Selenite	Sigma S9133	40 ng/ml
Heparin Sodium	Sigma H3149	10 units/ml
Corticosterone	Sigma C2505	40 ng/ml
bFGF	PeproTech 100-18B	10 ng/ml
EGF	PeproTech AF-100-15	20 ng/ml
4-hydroxy-tamoxifen (4-OHT)	Sigma H7904	100nM

Cells were passaged at 70-80% confluence using a standard protocol. Briefly, media was removed, cells washed once with HBSS (LifeTech) and Accutase (Sigma) was added to the monolayer, and incubated for approximately 5 min at 37°C. Once cell detachment was visually confirmed, the suspension was transferred to a centrifuge tube and spun down at 1500rpm for 5 min. The pellet was then resuspended in proliferation medium, and split 1:2 for expansion, or seeded onto glass coverslips at the desired cell density.

2.2.2.2 hCMEC/D3 Cell Line

hCMEC/D3 is an immortalized human cerebral microvascular endothelial cell line, kindly provided by P-O Couraud, (Institut Cochin, France), and its derivation has been previously described (Weksler, Subileau et al. 2005). Briefly, human brain tissue was obtained from an adult female with epilepsy following the surgical excision of an area of temporal lobe. The tissue was then subjected to enzymatic digestion, and microvessel fragments were separated by density-dependent centrifugation on 25% bovine serum albumin. These fragments were then washed and plated onto Type I Collagen coated plastic tissue culture flasks and grown to 50% confluence. They then underwent sequential lentiviral transduction of hTERT and SV40 large T antigen, and individual transduced cells were separated to produce clonal cell lines. Of these, the D3 line was selected based on its endothelial morphology, growth capacity, contact inhibition at confluence,

and stable expression of endothelial markers, such as von Willebrand Factor, PECAM-1, β-catenin and ZO-1.

For these experiments, D3 cells were grown in T75 tissue culture flasks (BD Biosciences) coated with rat tail collagen I (BD Biosciences) at 150µg/ml for 2 hours at 37°C in 5% CO_2. Growth medium consisted of EBM-2 supplemented as described in **Table 2.2**, and cells were passaged using Accutase (Sigma-Aldrich) when they reached 95% confluence.

Table 2.2. hCMEC/D3 Medium components

Component	Final Concentration	Supplier
EBM-2	Basal medium	Lonza
Fetal Bovine Serum "Gold"	5%	PAA
Chemically defined lipid concentrate	1%	Life Technologies
Penicillin-Streptomycin	1%	Sigma-Aldrich
HEPES	10mM	Sigma-Aldrich
Ascorbic Acid	5µg/ml	Sigma-Aldrich
bFGF	1ng/ml	PeproTech
Hydrocortisone	1.4µM	Sigma-Aldrich

2.2.2.3 Storage and revival

For cryogenic storage, cells were harvested as for passaging above and cells were resuspended in 1ml complete medium with 10% (v/v) DMSO (Dimethyl Sulfoxide, Sigma) at ~5 x 10^6 cells/ml for STROC05, or 5% DMSO at ~1 x 10^6 cells/ml for hCMEC/D3. The suspension was then transferred to a cryovial, which was put into a -80°C freezer in a secondary container (Mr Frosty) with isopropanol to ensure slow, steady freezing. After 24 hours, the cryovial was transferred to liquid nitrogen.

To revive cells, the cryovial was removed from storage and placed directly into a 37°C water bath until thawed. The suspension was then transferred to 10ml complete medium in order to dilute the DMSO, and centrifuged before resuspending the pellet in proliferation medium, seeding into a T75 and culturing under normal maintenance conditions. The medium was changed after 12-24 hours to ensure complete removal of any residual DMSO.

2.2.2.4 Fixation

Cells were rinsed twice with HBSS (Hank's Balanced Salt Solution, Gibco), then incubated for 15 min with cold 4% paraformaldehyde (PFA). Cells were then rinsed three times with PBS (0.01M Phosphate Buffered Saline, Sigma tablets) before being used for immunocytochemistry, or being sealed with Parafilm and stored under PBS + Sodium Azide (0.02%, Sigma) at 4°C for later analysis.

2.2.2.5 Immunocytochemistry

Coverslips were washed 3 x 5min in PBS. Cells were then incubated for 1 hour at room temperature in blocking solution (PBS + 10% Normal Goat Serum, Vector Labs + 0.1% Triton X100, Sigma) before being incubated at 4°C overnight with the required antibodies (**Table 2.3**). Cells were then washed again 3 x 5min in PBS before being incubated with AlexaFluor secondary antibodies diluted 1:500 in PBS for 1 hour at room temperature. Cells were then washed 3 x 5min in PBS before being mounted onto slides in a drop of Vectashield mounting medium + DAPI (Vector Labs).

Visualization of the BrdU label required a 2 step procedure. Immunocytochemistry for any other antibodies was performed first, then BrdU staining was applied. For this, cells underwent an additional fixation with 4% PFA for 20min to preserve the previous staining after removal of the secondary. Sections were then washed 3 x 5min in PBS followed by acid treatment to denature the DNA and allow binding of the BrdU antibody. Sections were incubated on ice for 10min with 1.0M HCl (Hydrochloric Acid, Sigma), then 10min at room temperature in 2.0M HCl followed by 20min in 2.0M HCl at 37°C. To neutralize the acid, cells were then incubated for 12min at room temperature in 0.1M Borate buffer (Sodium tetraborate decahydrate, Sigma) in PBS. Sections were then stained with BrdU antibody (rat anti-BrdU, 1:5,000, AbD Serotec) and the relevant AlexaFluor secondary according to the protocol above, but the overnight incubation with primary antibody was carried out at room temperature rather than 4°C.

Table 2.3 Antibodies and concentrations used throughout in vitro and in vivo immuno-staining.

Antibody	Concentration	Company	Cat. Ref.
BrdU	1:5000	AbD Serotec	MCA2060T
Galc	1:300	Millipore	MAB342
GFAP	1:3000	Sigma	G3893
HNA	1:400	Chemicon	MAB1281
HSP27	1:200	Enzo Life Sciences	SPA-803
Ki67	1:500	Abcam	ab15580
Nestin	1:2000	Millipore	MAB5326
Sox2	1:500	Santa Cruz	sc-17320
STEM101	1:500	Stem Cells Inc.	AB-101-U-050
Tuj	1:500	Abcam	ab18207

2.2.3 Cell labeling

Labels were used according to the manufacturers' instructions, or as previously used for cell tracking. This resulted in a range of different conditions and incubation times, shown in **Figure 2.4**. PKH26 is highly lipophilic and therefore requires only brief contact with cell membranes for intense fluorescence to be seen. Hoechst is highly cell permeant, with a high binding affinity and therefore also only requires a short incubation. Some Qtracker staining was observed with shorter incubation times, but a longer incubation time provided more homogenous labeling. BrdU is incorporated into cells only during DNA synthesis. Since the doubling time of this cell line is 3-4 days, a 4 day incubation should allow every cell to go through a proliferation cycle, and therefore to incorporate BrdU during DNA synthesis.

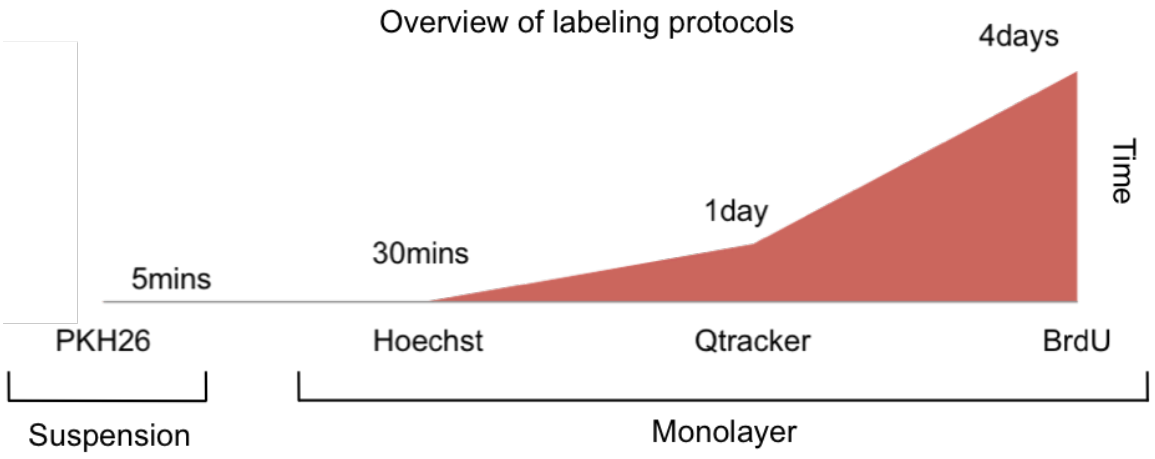

Figure 2.4. Overview of labeling protocols. The length of the protocol varies from minutes (PKH26) to days (BrdU).

2.2.3.1 PKH26

Cells were labeled according to the manufacturer's instructions (Sigma-Aldrich). Briefly, cells were harvested as for passaging, and the pellet resuspended in 1ml media. Viability (%) was then calculated by Trypan Blue exclusion, and the cells re-pelleted. 1ml diluent C per 1 x 10^6 cells was then added to resuspend cells, and an equivalent volume of PKH26 diluted 1:100 in diluent C was then added, to give a final concentration of 1:200 (5μM). Cells were then incubated for 4 minutes before 1% human albumin solution was added (equivalent volume to cell suspension) and incubated for a further 1 minute. Cells were then repelleted and washed three times in DMEM/F12 before being seeded at the appropriate density onto laminin-coated coverslips. The excitation spectrum of PKH26 peaks at 551nm and the emission spectrum at 567nm.

2.2.3.2 BrdU, 5-Bromo-2'-Deoxyuridine

77mg BrdU was dissolved in 5ml distilled water to give a 50mM stock solution. This was further diluted 1:250 and filtered (0.22μm pore size) to give a 0.2mM working solution. This is added to normal culture medium at 1:1000 to give a final concentration of 0.2μM (Caldwell, He et al. 2005) and media was replaced twice a day for four days. Cells were then harvested and seeded at the appropriate density. BrdU is not intrinsically fluorescent, but is detected using antibodies, so the excitation and emission spectra can be selected to match the microscope's filter sets.

2.2.3.3 Hoechst 33342

A stock solution was made up by dissolving 10mg Hoechst 33342 (Sigma) in 5ml distilled water to give a 2mg/ml solution, which was then filtered. This was added to normal culture medium at 1:1000 to give a final concentration of 2μg/ml, which was added to adherent cells for 30 minutes. Cells were then washed 3 times with HBSS before being harvested and seeded at the appropriate density. Due to the toxicity of Hoechst to this cell line, dilutions down to 0.02μg/ml were tested (**Figure 2.5**), but a similar cell loss by day 7 was observed.

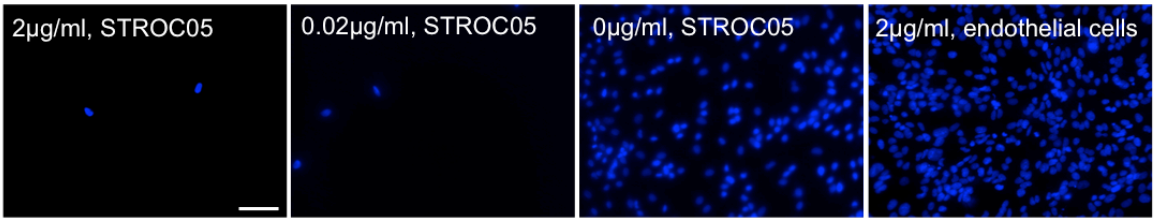

Figure 2.5 STROC05 cells were labeled with different concentrations of Hoechst, and allowed to differentiate for 7 days. A similar cell loss (number of DAPI cells) compared to unlabeled cells was observed with all concentrations tested. However, endothelial cells did not appear to be affected. Scale bar = 100µm

2.2.3.4 Qtracker

Qtracker 565 (Life Technologies) was used according to the manufacturer's instructions. Qtracker solution was made up by mixing together the required volumes of components A and B, and then incubating for 5min at room temperature. Fresh proliferation medium + 2% human albumin (Biosera) was then added to give a final Qtracker concentration of 15nM, and the solution was vortexed for 1min. Adherent cells were then washed twice with DMEM:F12, Qtracker solution was added, and cells were incubated for 24h at 37°C. Cells were then washed twice with DMEM:F12 and fresh proliferation medium was added, incubating at 37°C for 2.5h before harvesting as normal. The excitation spectrum of Qtracker 565 peaks below 400nm and the emission spectrum peaks at 565nm.

2.2.3.5 Fast Blue

Protocol 1 (Pettersson, Lobov et al. 2010): A 20mg/ml aqueous solution of fast blue (Sigma) was prepared, and 5µl was added to a 1ml suspension of 1 x 10^6 cells to give a final concentration of 100µg/ml. This was incubated at 37°C for 15 minutes before seeding cells at the appropriate density. This method resulted in very low cell survival, which was thought to be due to mechanical damage from particulate matter to the cell membranes during pipetting in suspension. It was therefore hypothesised that labeling cells as a monolayer may improve survival so the following method was tested

Protocol 2 (Liudmila Novikova, Umeå University): Culture medium was removed from growing cells and fresh culture medium was added containing fast blue at 5µg/ml. Cells were incubated for 12 hours before fast blue was removed and cells washed five times in DMEM/F12 before being harvested and seeded at the appropriate density. At this concentration, cell survival was not

affected, but no fast blue labeling was seen. Concentrations of 20, 40, 60. 80 and 100μg/ml were therefore tested using Protocol 2, and the number of surviving cells after 24 hours was counted using a ToPro3 (Invitrogen) nuclear counterstain (**Figure 2.6**). Cell survival decreased with increasing concentration of fast blue, but no labeling was seen at any concentration. Fast Blue was therefore excluded from further experiments.

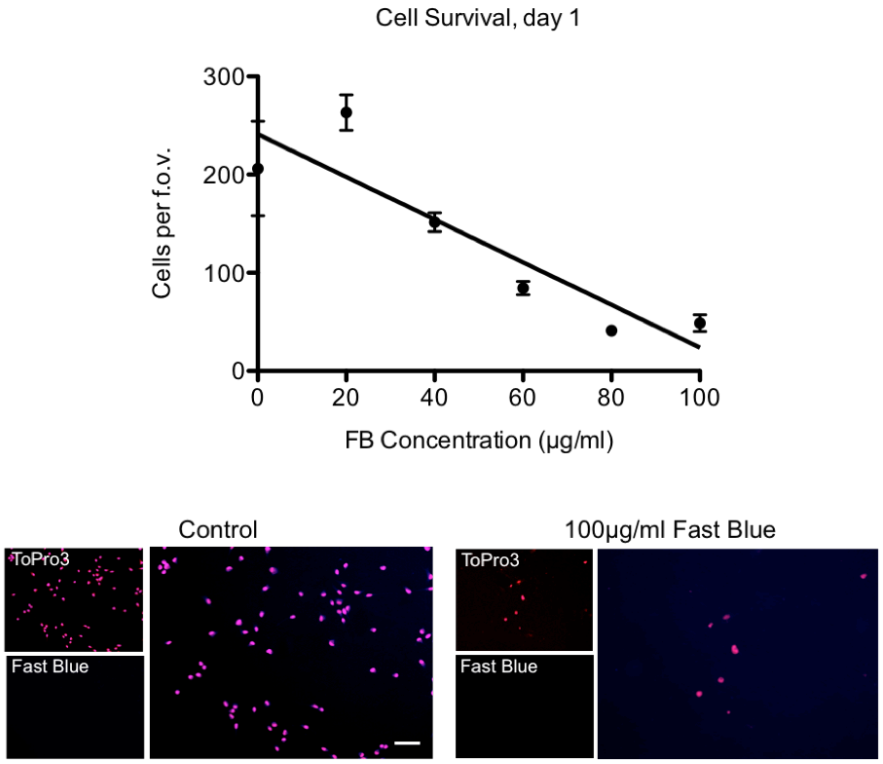

Figure 2.6. Fast Blue affected cell survival in a dose dependent manner, and no positive fast blue staining was seen even at the highest concentration. Scale bar = 100μm.

2.2.3.6 Enhanced Green Fluorescent Protein (eGFP)

Generation of eGFP-STROC05 cell line was performed by Dafe Uwanogho using lentiviral transfection of eGFP under a UCOE (Ubiquitous Chromatin Opening Element) promoter, designed to resist silencing in vivo. Once transduced, the eGFP cell line was cultured and passaged using the standard protocol.

eGFP expression was successfully detected (**Figure 2.7**A within 100% of cells. The intensity of the fluorescence was variable across the population. Cells were stained for Ki67 as a marker of proliferation at day 1 and 7, and the proportion of cells expressing Ki67, as well as the total cell number (DAPI+) were counted (**Figure 2.7**B). There were many more GFP+ cells

present than controls at both day 1 and after 7 days differentiation (**Figure 2.7**C). This can be accounted for by a dramatic increase in proliferation, as Ki67 was expressed by close to 98% of eGFP+ cells at day 1, compared to 55% of controls (**Figure 2.7**D, $p<0.001$). Additionally, cells appeared to be morphologically very different (**Figure 2.7**E), with a loss of processes and an increase in cell density. However, this difference appears to have been induced by the infection process itself rather than the presence of eGFP protein, as cells transduced by the empty vector showed the same morphological change. This eGFP+ cell line was therefore not taken forward for further experiments, particularly since the high rate of proliferation suggests potential tumorigenicity in vivo.

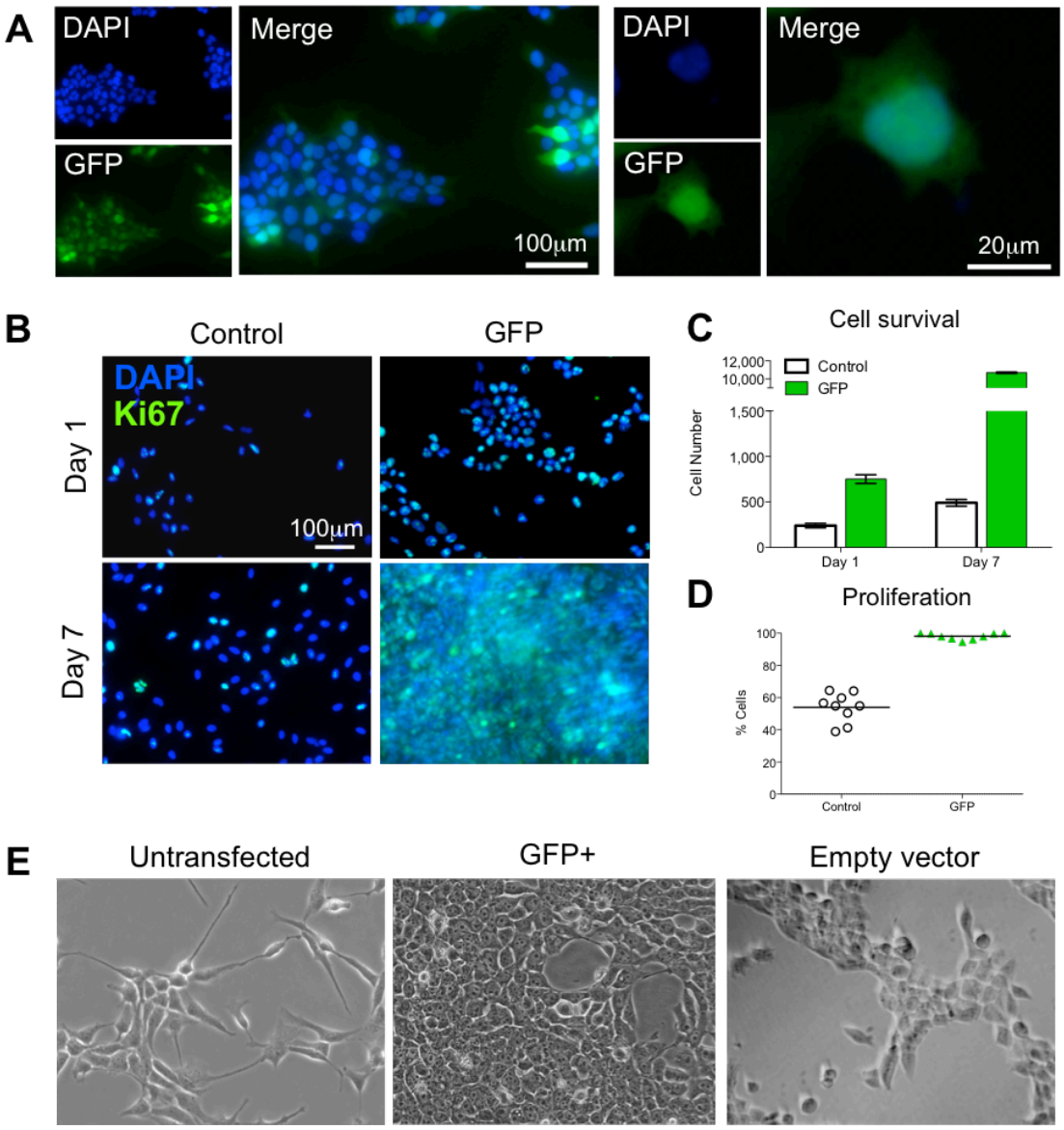

Figure 2.7 Effects of transduction on STROC05 NSCs. eGFP expression was robust (A), but cells stained with DAPI and Ki67 (B) showed a large increase in cell number compared to controls (C). Ki67 was expressed by 98% of eGFP+ cells (D), and there were morphological differences compared to control cells (E).

2.2.4 In vitro assays

2.2.4.1 Cell Viability

Trypan Blue Exclusion: Trypan blue dye is excluded from viable cells with an intact membrane, which therefore remain uncoloured, whereas dead or dying cells are permeable to the dye and become stained blue. Directly after completion of the labeling protocol, cells were harvested if necessary. Equal amounts of cell suspension and Trypan blue solution were thoroughly mixed by pulsing 10x with a pipette. The resulting suspension was transferred to a haemocytometer, and two counts were taken – total cells (Total), and blue stained cells (Blue). This was then expressed as a percentage: (Total - Blue)/Total x 100 = percentage viable cells

Live/Dead: Live/Dead staining was carried out using the LIVEDEAD cytotoxicity/viability kit (Invitrogen). Cells were simultaneously stained with green fluorescent calcein-AM (intracellular esterase activity) indicating a viable cell and red ethidium homodimer-1 (EthD-1) indicating a loss of membrane integrity evident in dead or dying cell. For this, cells were seeded at 1 x 10^5 cells/well on 13mm glass coverslips (VWR, laminin coated as for flasks above) in 24 well plates, in proliferation medium (**Table 2.1**), and cultured for 24 hours at 37°C. A solution was made up with PBS containing 4µM EthD-1 (component B; 20µl/10ml PBS) and 2µM Calcein AM (Component A; 5µl/20ml) and vortexed for 30 sec. 300µl of this solution was added to live cells after removal of media, and this was incubated at room temperature for 30 min in the dark. Slides were prepared by drawing circles using a hydrophobic barrier pen (DAKO) and dropping ~50µl of PBS into the centre. Coverslips were then placed cells-down onto this solution to avoid drying during imaging. Imaging was carried out immediately, using consistent exposure times to allow comparison between images. The excitation wavelength used for EthD1 also excited PKH26 due to their similar properties, but viable PKH26-labeled cells could still be distinguished by the additional green Calcein AM.

2.2.4.2 Cell survival & Proliferation

After labeling, cells were harvested if necessary and seeded at 1 x 10^5 cells/well. They were then cultured for 24h in proliferation medium. Cells for the Day 1 time point were then fixed, while cells for the day 7 time point were transferred into differentiation medium (**Table 2.1**) and cultured for a further 7 days before being fixed.

All cells were assayed for cell number by counting the total number of DAPI stained nuclei over 9 fields of view per coverslip (445x335µm, 20X objective). To measure proliferation, cells were stained for Ki67, which is present in the cell nucleus during all active phases of the cell cycle, only being absent during G_0 phase. The number of Ki67 cells was expressed as a percentage of DAPI nuclei, giving the percentage of cells proliferating.

2.2.4.3 Differentiation

After labeling, cells were harvested if necessary and seeded at 1 x 10^5 cells/well. They were then cultured for 24h in proliferation medium. Cells for the Day 1 time point were then fixed, while cells for the day 7 time point were transferred into differentiation medium as above and cultured for a further 7 days before being fixed.

Proliferation medium was then removed, cells were rinsed once with DMEM:F12 and differentiation medium was added (**Table 2.1**). The differentiation medium was changed after 30 min to improve removal of residual growth factors, and every other day thereafter.

After 7 days in differentiation medium, cells were fixed and stained with GFAP (Glial Fibrillary Acidic Protein, a marker of astrocytic lineage), Tuj1 (Neuronal class III beta-tubulin, a marker of early neuronal lineage) and Galc (Galactocerebroside, an oligodendrocyte marker). The number of cells staining positively for these markers was expressed as a percentage of DAPI+ cells, counted over 5 fields of view per coverslip, and was compared to unlabeled STROC05.

2.2.4.4 Co-cultures

In order to assess label leakage in vitro, NSCs were labeled, cultured overnight, and then mixed with unlabeled endothelial cells (1:1 ratio) in suspension before seeding the mixture into wells. Coverslips were coated with a mixture of collagen 1 as used for routine culture of endothelial cells, and laminin as used for culture of NSCs. The medium for the two cell types was also mixed in a 1:1 ratio. After 24 hours, cultures were stained for nestin, which is present in NSCs, but not ECs. Therefore co-localisation of nestin and the tested label indicates correct identification, whereas the presence of the label in a nestin negative cell indicates label leakage.

In order to rule out the possibility that observed results were only due to mechanical transfer between cells during the pipetting process, other paradigms were investigated. **Figure 2.8**A shows the method as described above. In **Figure 2.8**B, ECs are seeded first and cultured for 24

hours in their normal medium before switching to mixed media and seeding labeled NSCs on top. In **Figure 2.8**C, labeled NSCs are seeded first and cultured for 24 hours in their normal medium, before being washed three times with HBSS, switching to mixed media and seeding ECs on top. Finally, ECs and labeled NSCs were cultured separately for 24 hours in their own medium, before the conditioned medium from the NSCs was added to the ECs (**Figure 2.8**D), which were cultured for a further 24 hours before being fixed and stained.

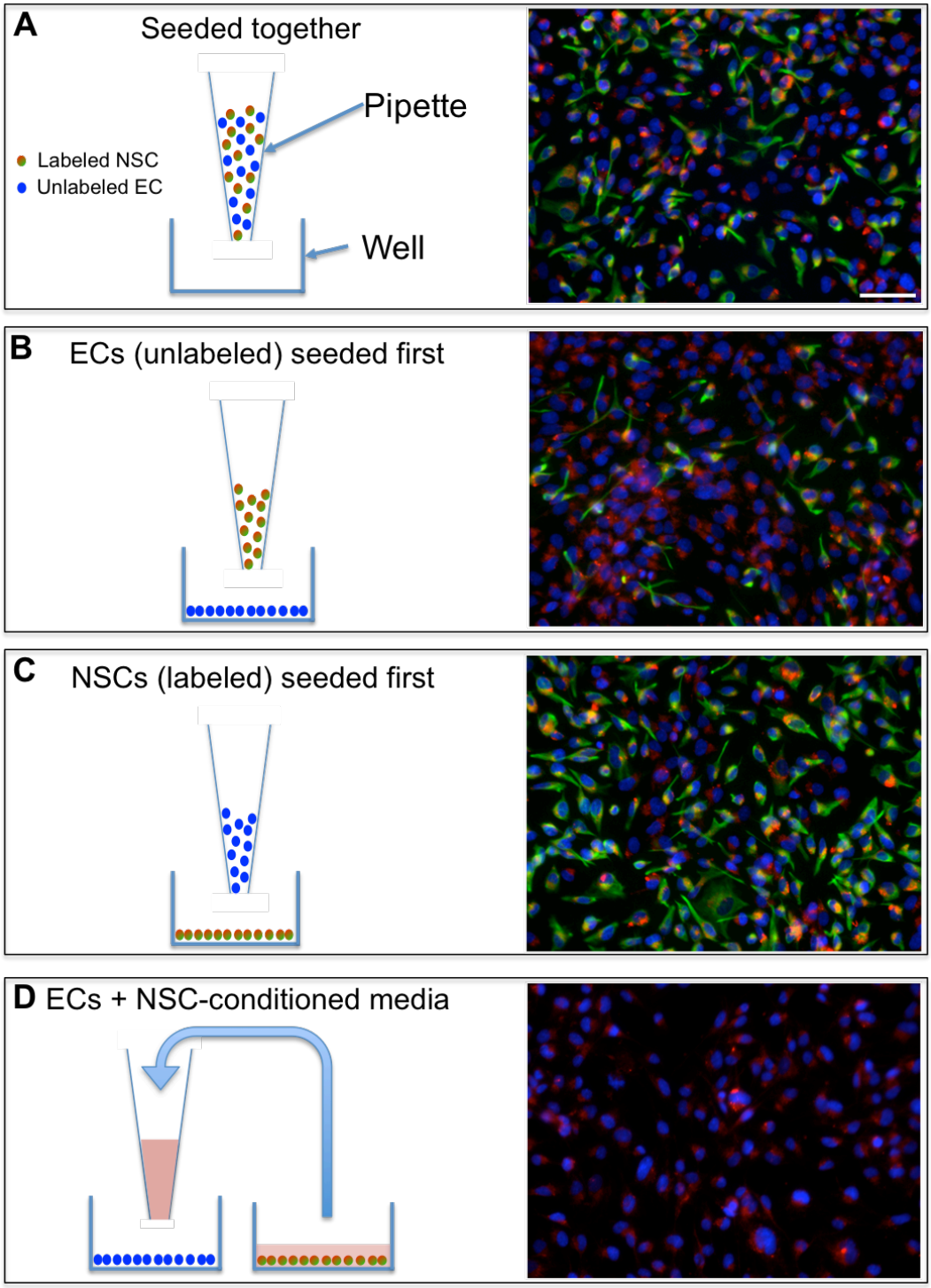

Figure 2.8. Conditions tested for co-culture, shown here with PKH26 labeled cells. Labeled NSCs (staining positive for nestin, green) were seeded with unlabeled ECs and co-localisation of PKH26 with nestin was assessed 24 hours later. Results were unaffected by seeding conditions. Whether labeled and unlabeled cells were seeded together (A), unlabeled cells were seeded first (B), labeled cells were seeded first (C) or simply conditioned medium was used (D), all ECs were labeled after 24 hours. Scale bar = 100μm.

2.2.5 Transplantation

The way in which cells are prepared for transplantation can affect their in vivo survival. Additionally, transplantation of dead cells is known to have effects on label leakage and reuptake (Burns, Ortiz-Gonzalez et al. 2006), making consistent cell viability at transplantation vital for this study. Conditions for storage of cells between cell preparation and transplanted were therefore tested, comparing room temperature against ice over time to define the available time window at each condition. Cells were prepared as for transplant at 50,000 cells/µl on three separate occasions, and three samples were counted at each time point. Cells maintained their viability much better at room temperature than when stored on ice, with a time window of 7 hours after preparation (**Figure 2.9**), so these were the conditions selected for use prior to in vivo experiments.

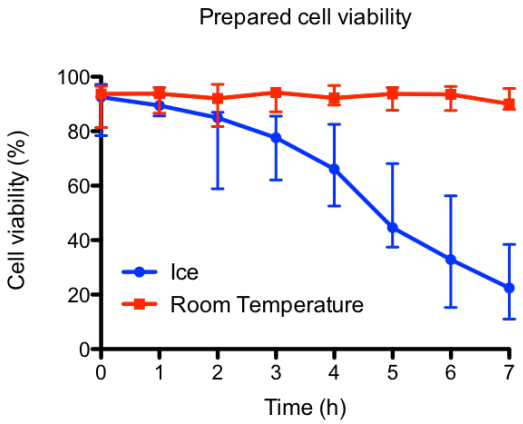

Figure 2.9. Cell storage conditions between preparation and transplant. Cells stored on ice after preparation showed a reduction in cell viability after 4 hours compared to immediately post preparation (blue line, $p<0.05$). However, when cells were stored at room temperature, their viability remained consistent up to 7 hours (red line, $p=0.097$). Data are shown as median ± range, (n=9).

2.2.5.1 Cell Preparation

Cells were labeled the day before transplantation, and incubated overnight in fresh proliferation medium based on results showing that overnight incubation after labeling reduced in vivo leakage (Lassailly, Griessinger et al. 2010). They were then washed three times with HBSS before being harvested as normal and resuspended in PBS. Cells were then counted (6 samples) using a haemocytometer and the total number of cells in the suspension was calculated. Cells were then centrifuged (5min, 1500rpm) and PBS aspirated. In order to achieve a cell density of 50,000

cells/µl, the volume of PBS to be added was calculated taking into account the cell volume as follows:

$V_L = V_T - V_C$

Where V_L = the volume of liquid to be added; V_T = Total volume of suspension (µl) = Total cell number/50,000; V_C = Volume occupied by cells = Total cell number x 3.912pl (volume of 1 cell)

Worked example:

For a total of $3x10^6$ cells, $V_T = 3x10^6/50{,}000 = 60\mu l$ and $V_C = 3x10^6 \times (3.912x10^{-6}) = 11.7\mu l$. Therefore the volume of PBS to be added = 60 - 11.7 = 48.3µl

The cell density was then verified by diluting 1µl of cell suspension in 50µl PBS and then further diluting 1:2 in Trypan Blue before counting (n=6 samples) using a haemocytometer, and adjustments made if the density was more than 10% different from the target density. For a target density of 50,000 cells/µl, densities of 45,000 to 55,000 cells/µl and cell viability of >85% were accepted (**Figure 2.10**). Cells were then aliquoted into separate suspensions for each animal to minimise potential variation and loss of viability induced by repeated resuspension.

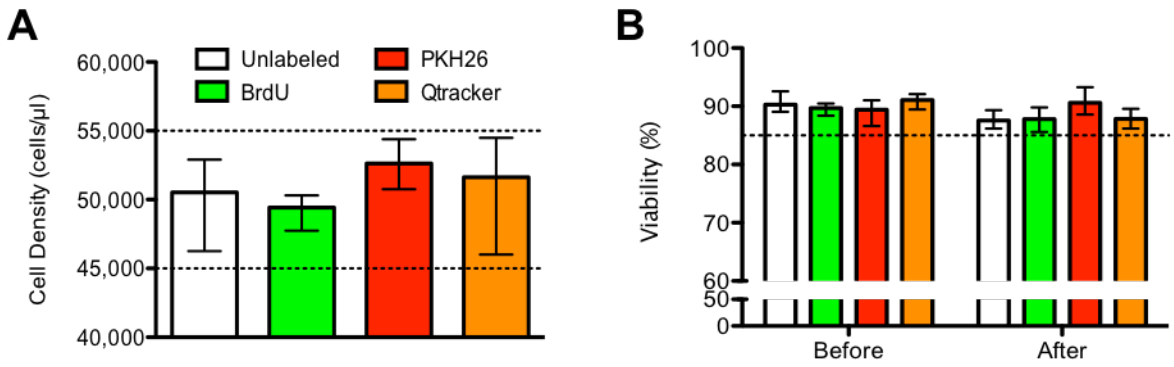

Figure 2.10. Cell density (A) and viability (B) with mean for each label. The range indicates the variation between different sets of transplant surgeries. Dotted lines show cut-off points.

2.2.5.2 Stereotactic Surgery

Male Sprague-Dawley rats (180-200g, Taconic Labs) were kept on a 12 hour light/dark cycle and allowed food and water ad libitum. Animals were then anesthetized using Isoflurane (4% induction, 2% maintenance) and secured to the stereotactic frame (Kopf) using ear and teeth bars. Body temperature was maintained using a homeothermic heating blanket controlled by a

rectal temperature probe. A rostro-caudal incision was made along the top of the head, and Bregma was located. A frame-mounted drill was used to make small burr holes in the skull at 0.9mm anterior and ±2.5mm laterally to Bregma. Cell suspension was briefly pipetted to resuspend cells, and 5µl of cell suspension was then taken up into a 10µl Hamilton syringe. For each set of surgeries, separate syringes were used for each group to avoid cross contamination, and each syringe and needle were cleaned 3 times in 3 separate vials of sterile PBS between animals. The syringe was then attached to the frame, and the 26G needle was inserted slowly to 5.5mm below dura. 4µl of cell suspension (total ~200,000 cells) was then injected at 1µl/min, and the needle was left in place for an additional two minutes before being slowly removed. Each animal received two injections (different experimental groups), one in each hemisphere. The two burr holes were then sealed with bone wax (Fisher), the incision was sutured, and the animal was given topical analgesic cream (2.5% Lidocaine and 2.5% Prilocaine, Sandoz) and IP Buprenex (0.05mg/kg; Henry Schein) and allowed to recover. Animals were then weighed daily until they had regained their pre op weight.

2.2.5.3 Perfusion

Animals were given IP injections of Pentobarbital Sodium (Fatal Plus, Vortech) at 10mg/100g body weight, and observed until the righting reflex was absent. They were then placed in a supine position inside a chemical hood, and the toe pinch reflex was tested. Once this was absent, the rib cage was dissected until the heart was easily accessible. The descending aorta was clamped, and a needle placed through the bottom of the left ventricle, and into the aortic arch, where it was clamped in place. The right atrium was then cut to allow exsanguination, and the peristaltic pump (MasterFlex, Cole Parmer) connected to the needle was switched on to pump ice cold PBS (0.01M) through the system. Once the outflow began to run clear, the pump was switched to ice cold PFA (4% in 0.01M PBS). Perfusion was concluded when the animal's forearms became rigid, and the brain was then removed and placed in 4% PFA overnight, after which it was washed three times in PBS and placed into 30% Sucrose (Sigma) for cryoprotection in PBS with 0.5% Sodium Azide for preservation.

2.2.5.4 Sectioning

Brains were separated into two hemispheres, embedded in frozen section compound (Surgipath FSC 22, Leica) and cut at 40µm section thickness 1:8 series on a Leica Cryostat. These were

then stored as floating sections in Tissue Cryopreservation Solution (TCS, 30% Ethylene Glycol, 25% Glycerol and 0.5% Sodium Azide in PBS) to prevent freezing at -20°C until processing for Immunohistochemistry.

2.2.6 Immunohistochemistry

Immunohistochemistry was performed as in section 2.2.2.5 for immunocytochemistry. Floating sections were transferred from one wash to the next in a 24 well plate using a paintbrush. Additionally, all washing and incubation steps were carried out on a shaker, and 0.3% Triton X-100 was used, rather than 0.1%. These measures were taken in order to improve antibody penetration of the tissue.

Instead of using Vectashield + DAPI, sections were incubated for 5min on a shaker at room temperature with Hoechst (1µg/ml in PBS, Sigma) before being washed again (3 x 5min, PBS), mounted onto slides and coverslipped with Vectashield mounting medium (Vector Labs). This again improved homogeneity of staining throughout the tissue thickness.

2.2.7 Image analysis

Images for analysis were acquired using an AxioImager M2 microscope (Zeiss) in conjunction with Stereo Investigator software (MBF). In one series, all areas containing cells positive for HNA or for the label of interest were imaged using a 20X objective. For analysis, alternate sections of those imaged were selected in addition to always choosing the first, last and centre section containing cells in order to have a representative coverage of the graft. In each image, an ROI was drawn and all cells within it that were positive for HNA and/or label of interest were counted and categorised using ImageJ64 and its cell-counter tool. Cells (Hoechst+) were categorised as “correctly identified” where both HNA and the label were present, “false negative” where HNA was present but the label was not, or “false positive” where HNA was not present but the label was. Cells with faint, shadowy HNA staining that expanded well beyond the nucleus were not counted as HNA positive, as this was background auto fluorescence. Cells with cellular HNA staining were counted as positive, whether the staining was nuclear or cytoplasmic. An indicator of positive Qtracker and PKH26 labeling is concentrated dots around the nucleus and, in the case of BrdU, labeling of the nucleus. Extremely bright flares of fluorescence were not counted as this is not indicative of positive staining or labeling, but rather miscellaneous debris. An example is shown in **Figure 2.11**

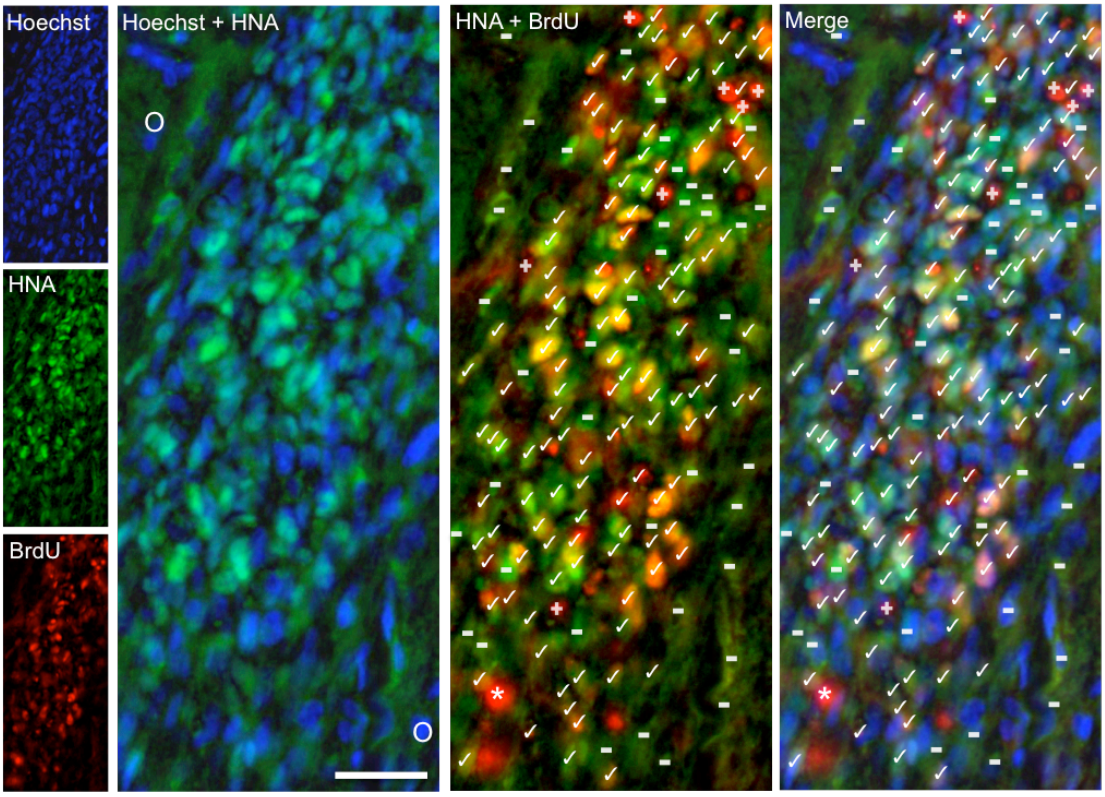

Figure 2.11. In vivo quantification. ✓ indicates a cell correctly identified by the label, positive for both HNA and the label under investigation (here BrdU). + indicates a false positive, where an HNA negative cell is positive for BrdU. – indicates a false negative, where a cell is positive for HNA but negative for label. * indicates fluorescent debris, which was not counted as positive BrdU staining. O indicates cells negative for both HNA and BrdU which would therefore not have been included in the count. Scale bar = 100μm.

2.2.8 Statistics

Statistical tests were performed using Prism 5.0f (GraphPad). Where percentages are calculated and the values are close to 0 or 100%, there is potential for the distribution to become skewed due to floor or ceiling effects. Therefore, normal distributions have not been assumed, and non-parametric tests have been used throughout. For cell viability over time (**Figure 2.9**), a Friedman test was used, with Dunn's multiple comparison test. For all other in vitro experiments, Mann-Whitney tests were used to compare each group of labeled cells with its matching control. For in vivo analyses (**Figure 2.18**), Kruskal-Wallis tests were used with Dunn's multiple comparison test to compare all labels to each other. Values were considered significant where $p<0.05$. For in vitro assays, three biological replicates, each with three technical replicates were conducted to give n=9 (unless otherwise stated). For in vivo analysis, n=5 animals per label per time point.

2.3 Results

2.3.1 Cell labeling

From the six labels under investigation here, Fast Blue did not label cells and hence was omitted from further analysis. eGFP labeled the cells, but was also excluded from further analysis due to a significant transformation in cellular characteristics. The four labels that were advanced for further testing were Hoechst, BrdU, PKH26 and Qtracker. All were easily incorporated into STROC05 NSCs. Hoechst is seen in the nucleus, co-localised with ToPro3, used here as a nuclear counterstain during immunocytochemistry. BrdU is also localised to the nucleus, whereas PKH26 and Qtracker are both situated in the cytoplasm, shown by their co-localisation with nestin (**Figure 2.12**A). Hoechst showed a very homogenous distribution across cells (**Figure 2.12**B), with all showing approximately equal fluorescence. BrdU, however, was highly variable with some cells fluorescing much more brightly than others. PKH26 and Qtracker appear similar, and both are somewhat variable across the population.

The expected intracellular localisation of each label is shown in **Figure 2.12**C. Hoechst binds to the minor groove of DNA, whereas BrdU is incorporated into DNA during proliferation, replacing Thymidine. These localisations are both corroborated by the cell images shown. PKH26 binds to the phospholipid bilayer, inserting into the cell membrane and was therefore expected to be mainly at the edge of the cell. However it is seen in the perinuclear area, suggesting incorporation into the membranes of organelles and endosomes. The Qtracker system is based on Qdot nanocrystals at 10-20nm, consisting of a core made of cadmium mixed with selenium or tellurium, coated with zinc sulphide. This is coated with a proprietary targeting peptide for localisation to the cytoplasm, which is reflected here by the location of the intracellular fluorescence.

All labels showed over 99% labeling efficiency at day 1 (**Figure 2.12**D). There were insufficient Hoechst labeled cells remaining at day 7 for analysis. BrdU showed a significant drop in labeling efficiency, from 99% to 87% ($p<0.001$), but PKH26 and Qtracker retained a label efficiency above 99%.

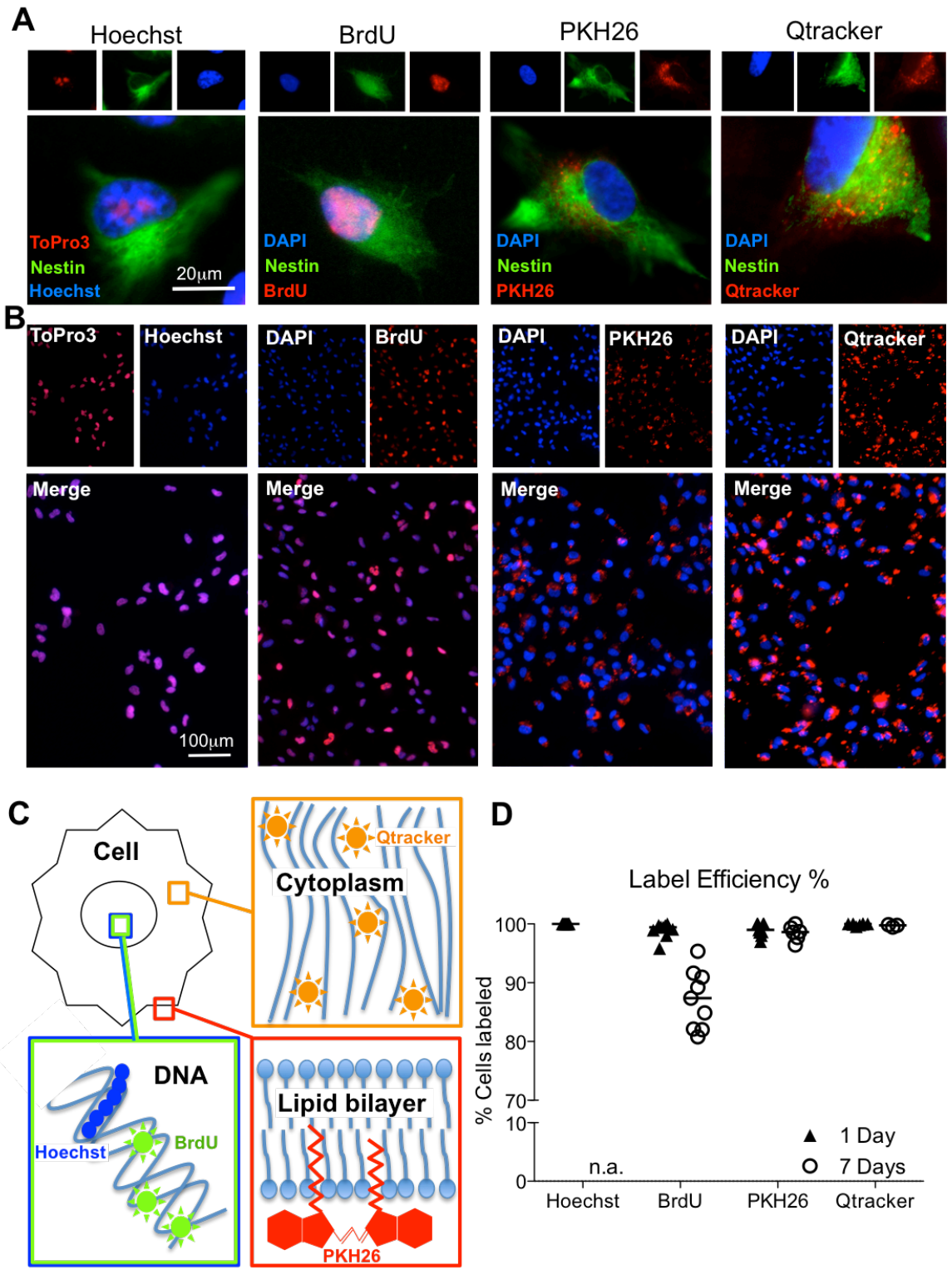

Figure 2.12. Label Efficiency. The appearance of cells after labeling is shown here at the single cell level (A), and the population level (B). The intracellular localisation of each label is slightly different (C). Labeling efficiency was high at day 1 for all labels tested (D). At day 7, efficiency remained high for PKH26 and Qtracker, but dropped for BrdU (lines represent the median).

2.3.2 Cell viability

In order to assess the effects of the labels on cell viability, Trypan Blue and Live/Dead assays were used to count the number of live and dead cells (**Figure 2.13**A). The Trypan Blue exclusion assay consists of a blue dye which is only cell permeable when the cell membrane is damaged. Therefore the number of cells able to exclude the dye as a proportion of the total gives a measure of the number of viable cells. No significant difference was shown from controls immediately after labeling for Hoechst, BrdU or Qtracker labeled cells (**Figure 2.13**B). However, PKH26 labeled cells showed a significant 6.4% reduction in viability ($p<0.001$). This shows that the labeling procedure for PKH26 affects viability, although whether the source is the label itself or other causes (e.g. supplied diluent, labeling in suspension) remains unclear. Additionally, since Hoechst, BrdU and Qtracker labeling protocols are all conducted on adherent cells, there is opportunity for dead cells to detach and be lost during the labeling procedure, and therefore not be included in the final count.

The Live/Dead assay consists of red dye permeable only to cells with a damaged membrane, and also a green dye requiring active intracellular esterases to produce green fluorescence. At 24 hours after labeling, there were no significant differences from unlabeled cells (**Figure 2.13**B). Hoechst labeled cells showed a 2.4% lower viability than controls, but this was not significant ($p=0.16$).

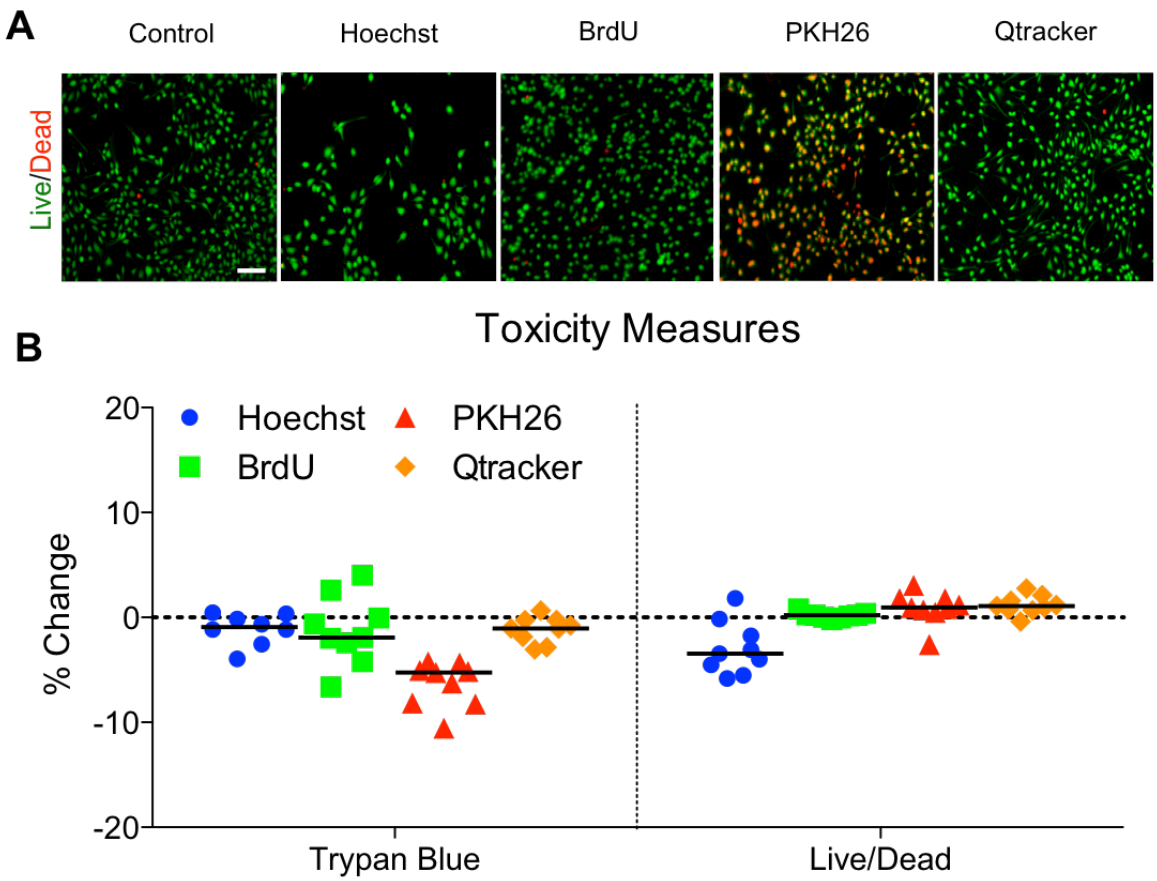

Figure 2.13. Labeled cells were stained with a Live/Dead kit comprising Calcein AM (green, live cells) and EthD1 (red, dead cells, A). Viability of labeled cells was compared to control cells using Trypan Blue immediately after labeling and Live/Dead after 24 hours (B, median change in % viability). Scale bar = 100µm

2.3.3 Cell survival and proliferation

In order to gauge delayed effects on cell death and proliferation, cells were seeded onto coverslips and allowed to proliferate overnight or differentiate for one week before being fixed, and the number of remaining cells counted. Cells were then stained for Ki67, a marker of proliferation (**Figure 2.14**A). The cell number and percentage expressing Ki67 were compared to unlabeled cells, to provide a measure of the changes induced by the label.

Hoechst had the most dramatic effect on cell number (**Figure 2.14**B), with 77% fewer cells than controls at day 1 ($p<0.01$), and almost no cells remaining at day 7 ($p<0.001$). Ki67 expression was also reduced by 45% ($p<0.001$) at day 1, and there were insufficient cells to assess this at day 7. Hoechst was therefore not taken forward to further in vitro or in vivo testing.

BrdU had the smallest effect on these parameters (**Figure 2.14**C). Proliferation is slightly elevated at day 1 at 12.8% higher than controls ($p<0.05$), but there was no significant change in cell survival ($p=0.095$). By day 7, there appears to be very little difference to control cells (Survival $p=1.0$; Ki67 $p=0.72$), showing no delayed toxicity due to the presence of the label within cells over 7 days.

Cells labeled with PKH26 appeared different from controls at day 1, but similar at day 7 (**Figure 2.14**D). At day 1, cell number was elevated ($p<0.001$) while Ki67 expression was lower than controls ($p<0.001$). Since the expression of Ki67 is reduced, the high cell number at day 1 is not likely to be due to an increased proliferation rate. It may therefore be due to improved adhesion or survival of cells after plating, as passaging of unlabeled STROC05 cells normally results in some cells floating and being lost in media changes rather than adhering to the laminin coating. However, at day 7 neither cell number ($p=0.93$) nor Ki67 expression ($p=0.37$) are different to controls. The return of cell number to normal levels can be accounted for by the reduced proliferation rate seen at day 1. It seems that the labeling process itself rather than the presence of the label may be the source of the change in cell behaviour at day 1.

Cells labeled with Qtracker showed an increased cell number at both time points, whereas Ki67 expression was elevated at day 1 and then slightly reduced at day 7 (**Figure 2.14**E). The cell number at day 1 was more than double (124%) that of controls ($p<0.001$), whilst Ki67 expression was only slightly elevated (27% higher than controls, $p<0.0001$). Given that the doubling time of these cells is 3-4 days, it seems unlikely that the modest increase in proliferation could be solely responsible for the large increase in cell number over just one day. It is therefore likely that cell survival and/or adhesion are also enhanced by Qtracker or the labeling protocol during the passaging process. However, the specifics of the targeting peptide used in the Qtracker kit are unavailable so its potential interactions remain unclear. At day 7, cell number remains significantly higher than controls ($p<0.001$), but this is likely to be a direct result of the higher cell number at day 1, and therefore does not represent any further change. However, Ki67 expression is reduced at day 7 ($p<0.001$), suggesting an effect of the continued presence of Qtracker in the cells over 1 week.

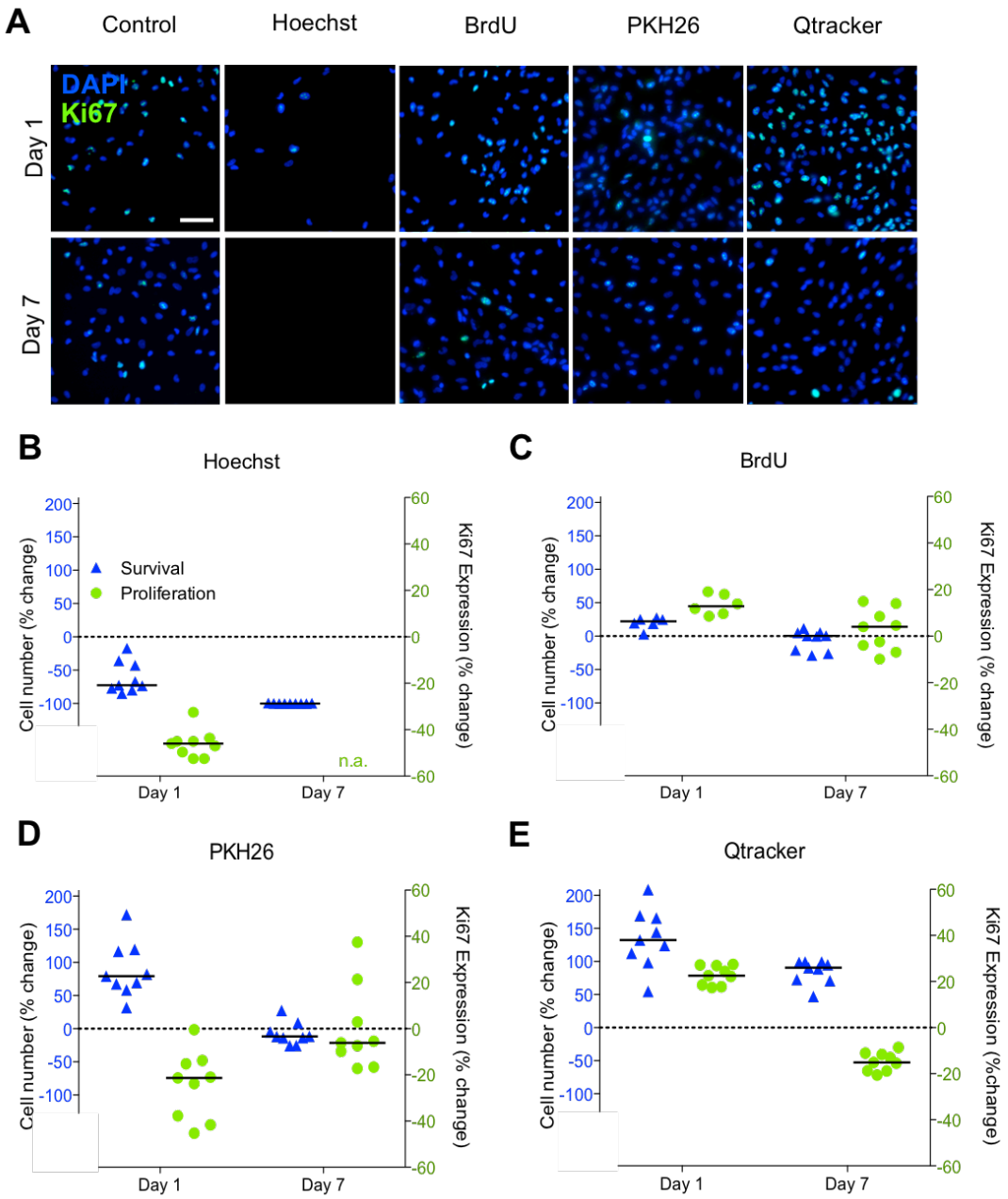

Figure 2.14. Effects of labels on STROC05 survival (DAPI+ cells) and proliferation (Ki67 expression) (A). Hoechst showed the most dramatic effect, with very few cells remaining at day 7 (B). BrdU showed little difference from controls, suggesting that the label is well tolerated (C). PKH26 showed differences at day 1, but not at day 7 (D), and Qtracker showed differences at both time points, showing that cells were affected by the label's presence in the cell (E). Scale bar = 100µm.

2.3.4 Label effects on cell phenotype

In order to assess more subtle effects on the biology of neural stem cells, labeled cells were differentiated for seven days before being stained for markers of different lineages; GFAP for astrocytes, Tuj for neuronal cells and Galc for oligodendrocytes (**Figure 2.15**A). Tuj and Galc positive cells appear morphologically consistent between control and labeled cells. However,

clear differences can be seen in GFAP positive cells. Compared to controls, PKH26 labeled GFAP+ cells show morphology more characteristic of reactive astrocytes, with increased projections and brighter staining. Qtracker GFAP+ cells, however, show long single or double projections rather than multiple ones, more suggestive of a radial glia phenotype.

Cells labeled with BrdU have a lower proportion of GFAP positive cells at both 1 day ($p<0.05$) and 7 days ($p<0.05$, **Figure 2.15**B). Since the difference between labeled and unlabeled cells remains consistent between day 1 and day 7, it seems that this is due to initial toxicity of the BrdU labeling protocol to GFAP positive cells, and that the continued presence of the label in the cell does not have further effects. The number of Tuj positive cells is not significantly different from controls either at day 1 ($p=0.86$) or day 7 ($p=0.64$), showing that BrdU does not affect the proportion of neuronal precursors. The number of Galc positive cells is significantly higher than controls at day 1 (+18%, $p<0.01$), suggesting that these might be the cell sub-population with increased proliferation. At day 7, the difference is smaller but still significant (+6%, $p<0.01$), consistent with reduced proliferation.

PKH26 labeled cells do not show significant differences for any of the three markers at day 1 (GFAP $p=0.16$, Tuj $p=0.93$, Galc $p=0.10$, **Figure 2.15**C), showing that the labeling process does not have acute effects on cell phenotype. However, the presence of the label in cells over 7 days shifts the ratio of cell populations towards GFAP positive cells, with an 11% increase in GFAP positive cells ($p<0.001$), but a decrease in Tuj positive (-6%, $p<0.001$) and Galc positive (-3.6%, $p<0.05$) cells.

Qtracker labeled cells show a significant increase in the proportion of GFAP positive cells at day 1 ($p<0.001$) and day 7 ($p<0.001$, **Figure 2.15**D), showing that the labeling process increases this proportion, but that the continued presence of the label does not appear to have further effects. The proportion of Tuj positive cells is not significantly different from controls at day 1 ($p=0.81$) or day 7 ($p=0.063$). The proportion of Galc expressing cells is not significantly different from controls at day 1 ($p=0.39$), but is significantly decreased at day 7 ($p<0.05$, $n=3$).

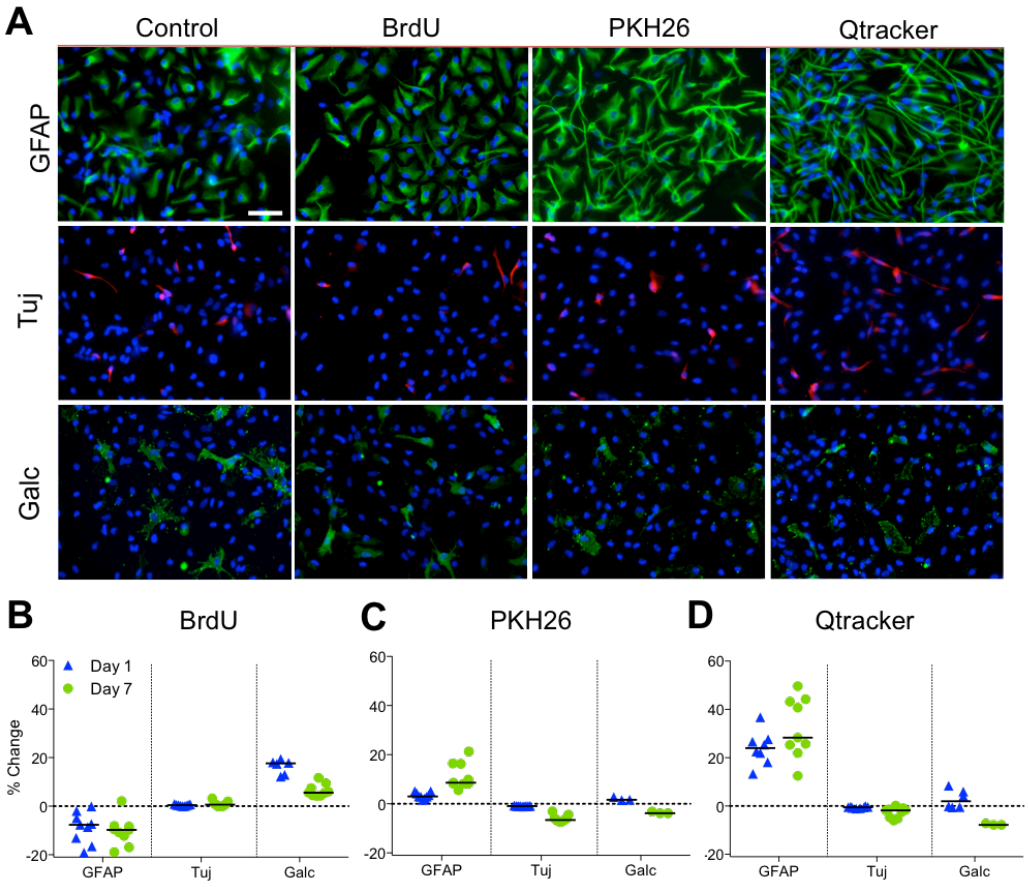

Figure 2.15 Cells were allowed to differentiate over seven days and stained for GFAP, Tuj and Galc (A). The percentage of cells expressing each marker was compared to unlabeled cells after labeling (median % change) with BrdU (B), PKH26 (C) or Qtracker (D), and are show here as median change from controls. Scale bar = 100µm.

2.3.5 Label leakage in vitro

In order to assess the propensity for the label to be released from labeled cells and taken up by its neighbours, labeled NSCs were seeded together with unlabeled D3 endothelial cells (ECs). These were distinguishable by staining with an antibody against nestin or sox2, which are expressed by NSCs but not ECs. Therefore label retention could be assessed on its localization within only nestin or sox2 positive cells.

With Hoechst-NSCs, all ECs were Hoechst positive after 24 hours (**Figure 2.16**A). Although the DNA binding of this label makes it less likely to be lost from viable cells, Hoechst labeling has a significant effect on viability. It's therefore likely that the label was released from dying cells and taken up by those remaining. With BrdU-NSCs, some ECs remained unlabeled (**Figure 2.16**B, red arrow), but some were faintly labeled with BrdU (**Figure 2.16**B, blue arrow). This reflects the

higher cell survival of BrdU-NSCs compared to Hoechst-NSCs, and that its incorporation occurs only during DNA synthesis. With PKH26-NSCs, all ECs were labeled after 24 hours (**Figure 2.16**C). Similar lipophilic dyes DiI and DiR have previously been shown to be released not freely into media but in diffusible elements recoverable by ultracentrifugation (Lassailly, Griessinger et al. 2010). These data show that PKH26 is transferable by the same mechanism, as conditioned medium was sufficient to induce EC labeling (see section 2.2.4.4). This mechanism is most likely exosome transfer, which has been shown to occur in neural progenitor cells (Marzesco, Janich et al. 2005). Qtracker-NSC co-culture also resulted in labeling of all ECs, and are also likely to be transferred within exosomes due to their cytoplasmic location. Overall, BrdU was the only label not to result in labeling of 100% of co-cultured ECs, but some label transfer was still observed.

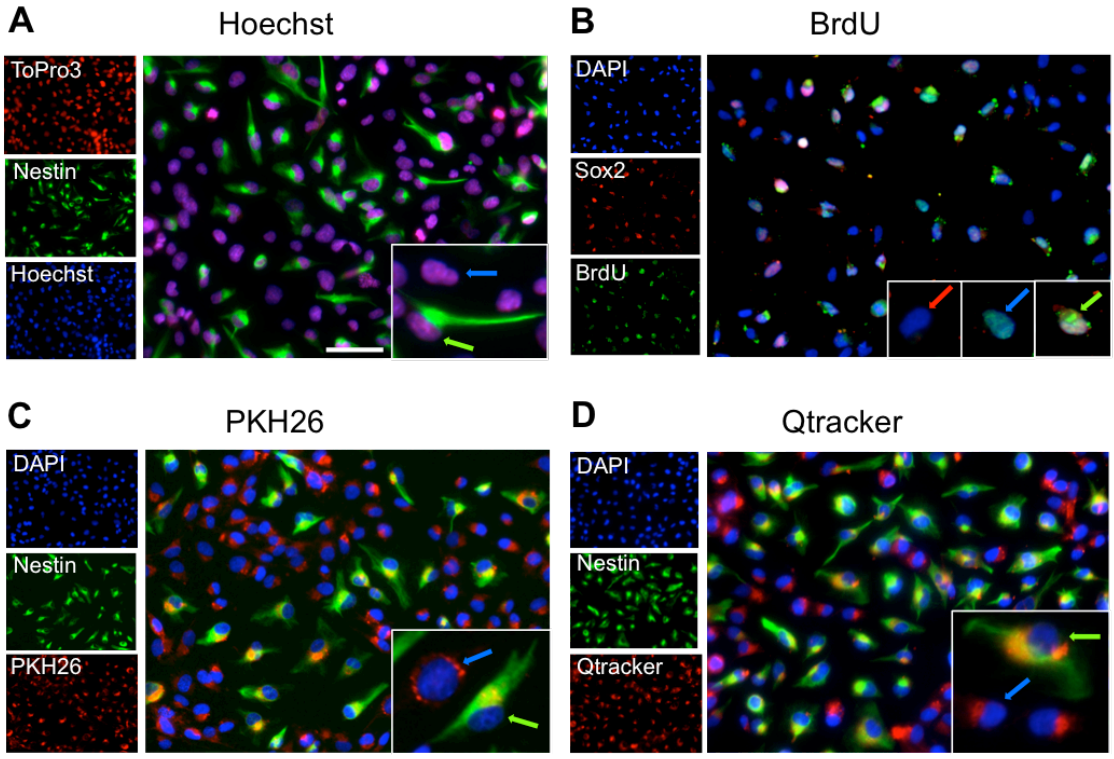

Figure 2.16 Labeled NSCs were seeded with unlabeled ECs to assess label transfer. All cells are stained with nuclear counterstains ToPro3 (A, red) or DAPI (B,C,D, blue). NSCs can be identified by nestin (A,C,D, green) or sox2 staining (B, red). Green arrows show labeled NSCs; Blue arrows show labeled ECs, indicating that label has been transferred from NSCs. Red arrow indicates unlabeled ECs. Scale bar = 100µm.

2.3.6 Reliability of labels for identifying transplanted cells in vivo

Labeled cells were transplanted into the striatum of healthy rats, and sections were stained with HNA (Human Nuclear Antigen) which reacts with the transplanted cells but not host tissue. The

extent of co-localisation with HNA was then assessed for each label to give a measure of its reliability. The graft appears to be much reduced in size over seven days (**Figure 2.17**) showing that many cells died. However despite this, there does not seem to be significant leakage of the labels into surrounding host tissue. Due to the punctate nature of their labeling, PKH26 and Qtracker labeled grafts appeared somewhat hazy under the microscope, and at times making it more difficult to precisely identify which cell nucleus the labeling belonged to. BrdU as a nuclear label was much clearer.

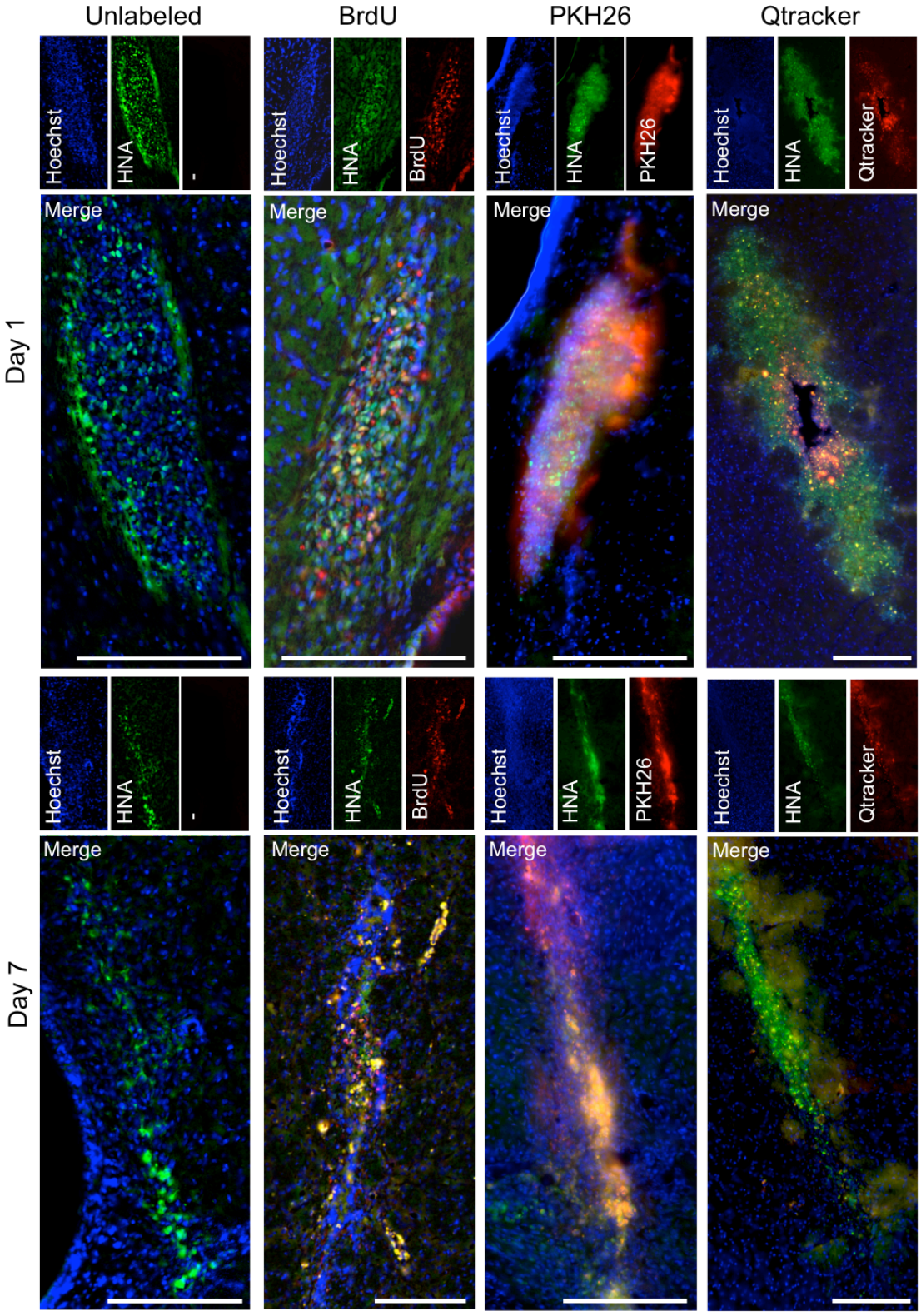

Figure 2.17 Transplanted cells 1 and 7 days post transplant showing HNA (green), Hoechst counterstain (blue) and labels (red). The overall appearance of the graft is consistent across labels at each time point, and the size of the graft appears much reduced by day 7. Scale bars = 200μm.

Cells were counted and categorised as either correctly identified (HNA+/Label+), False negative (HNA+/label-) or false positive (HNA-/Label+) as shown in **Figure 2.18**A. At day 1, all labels

correctly identified ~60% of cells (**Figure 2.18**B) with no significant difference between them ($p=0.99$). At day 7, Qtracker correctly identified 75% of cells. This was significantly more than PKH26 at 51% ($p<0.05$). BrdU correctly identified 62% of cells at day 7, which was not significantly different from either PKH26 or Qtracker.

At day 1, ~38% of cells were not identified by the labels, despite being HNA+ (**Figure 2.18**C), and there were no significant differences between the labels ($p=1.0$). At day 7, PKH26 had 46% false negatives, significantly higher than Qtracker at 24% ($p<0.05$). BrdU was not significantly different from either at 29%.

False positives, where cells appeared to be labeled despite being negative for HNA, constituted the smallest group, showing very little transfer of the labels from transplanted to host cells (**Figure 2.18**D). At day 1, Qtracker had 1.6% false positives, significantly more than BrdU at 0.16%, and PKH26 was not significantly different from either at 0.44%. At day 7 there were no significant differences between labels ($p=0.44$) and the numbers remained very low at <1% for all labels.

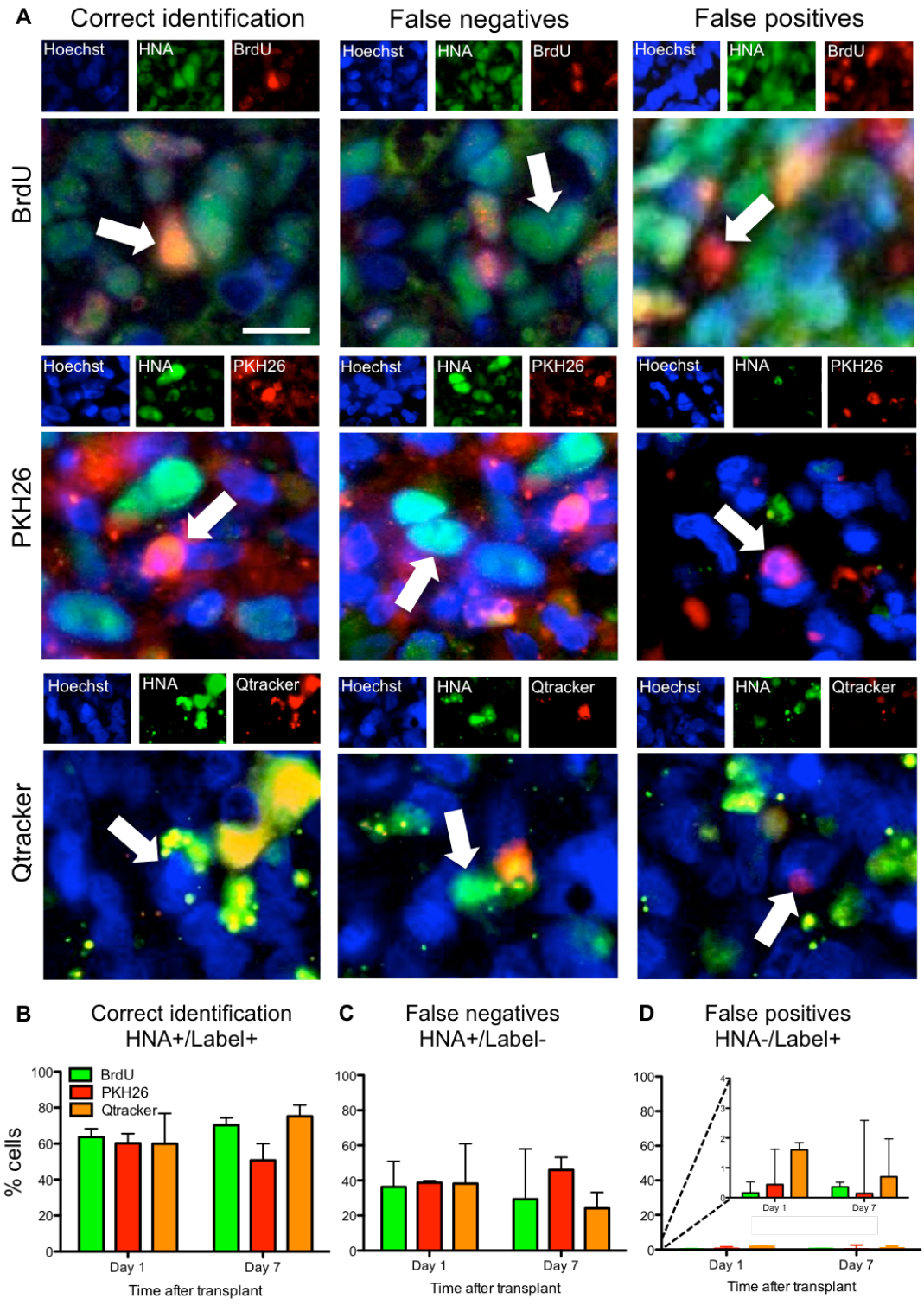

Figure 2.18 Cells were categorised as correctly identified (HNA+/Label+), False negative (HNA+/label-) or false positive (HNA-/Label+) (White arrows, A). The number of cells in each category was counted, and expressed as a percentage of the total, shown here as median and IQ range for each label for Correct identification (B), False negatives (C) and False positives (D). Scale bar = 20µm.

2.4 Discussion

Reliable cell identification is vital in order to understand and improve therapeutic transplants. Here we compared widely used cell labels for tracking transplanted neural stem cells. None of the labels tested showed significant leakage in vivo, but all showed a large number of false negatives. All labels tested showed some effect on cell biology, and the commonly used toxicity tests were insufficient to detect these effects.

2.4.1 Reliable Identification of transplanted cells

The reliable identification of transplanted cells is essential in order to elucidate their therapeutic mechanisms, and the use of exogenous labels is necessary where transplanted cells are not immunohistochemically different from host tissue, for example in the case of allo- or auto-grafts. Exogenous labels potentially provide a method of identification that is quick, and easy to translate between different cell lines and types. Concerns have been raised about their reliability, and most of the labels tested here have previously been shown to be transferred to host cells, or otherwise to be easily confused with host cell types (Iwashita, Crang et al. 2000, Burns, Ortiz-Gonzalez et al. 2006, Lassailly, Griessinger et al. 2010, Spitzer, Sammons et al. 2011). However, they are still used and relied upon for identification of transplanted cells, and to draw conclusions about their fate (Liu, Zou et al. 2014).

False negatives have not been studied in much detail, but are equally important. Since labels are likely to be lost most quickly from cells that are proliferating, this can induce a bias in drawing conclusions about the transplanted population, as a proliferating subpopulation would be excluded from the analysis. The concentration of the agent is likely to be a key factor in attaining a balance between false positives and false negatives, and factors such as the cell proliferation rate in vivo, the time between labeling and transplant and the status of the cell at implantation will all affect this optimisation.

It has previously been shown that transplantation of dead cells results in a higher incidence of label transfer (Burns, Ortiz-Gonzalez et al. 2006), showing that the viability of the transplant will affect not only its therapeutic efficacy but also the reliable identification of the cells. This combination would make interpretation extremely challenging. Factors potentially affecting viability here include the storage conditions between cell harvesting and transplant, as well as the time window available (Gobbel, Kondziolka et al. 2010). This is particularly important when one

cell preparation is used for a number of contiguous surgeries to ensure delivery of a consistent product between the first and last transplant of the day (see **Figure 2.9**). Additional items to consider here include those involved in the delivery process, such as potential cell damage if they must be delivered through a small bore needle (Agashi, Chau et al. 2009, Gobbel, Kondziolka et al. 2010). However, even after transplantation, membrane turnover and vesicle release will cause some leakage of labels located in the membrane or cytoplasm (Lassailly, Griessinger et al. 2010). Additionally, since the eventual fate of most transplanted cells is cell death (Smith, Stroemer et al. 2011), a lot of label will eventually be released regardless of the efficiency of its binding to cell components.

2.4.2 Impact of exogenous labels on cell function

All labels tested here have been previously shown to be both toxic and non-toxic, depending on the cell type and labeling protocol (including concentration). This has made it challenging to draw comparisons between labels. Additionally, some studies use viability assays as the sole measure of label impact, and these have here been shown not to be sensitive to delayed cellular effects.

The reported phenotypic effects of exogenous labels vary widely, and include proliferation, migration, homing and differentiation. One potential mechanism for altering the phenotype of a population is through selective toxicity, whereby the viability of a sub-population is affected, thereby biasing the proportion of the remaining population towards an alternate phenotype. BrdU in particular has been shown to be selectively toxic to neuronal precursors (Caldwell, He et al. 2005), although this effect can be attenuated by using a lower concentration.

However, there appear to be other phenotypic effects unrelated to toxicity. In **Figure 2.15**, a clear difference in morphology can be seen between the PKH26- and Qtracker-labeled GFAP+ cells. Such a consistent population-wide change in morphology cannot simply be due to selective toxicity, and suggests that labels are interfering with cellular pathways.

When assessing a label's suitability for use, it is therefore important to take into account the proposed therapeutic mechanism. For example where the end goal is tissue replacement, differentiation and survival are the most important parameters. However, if neurotrophic effects were the proposed mechanism, then ELISAs to assess changes in growth factor release would be more important. However, due to the interplay between these with regards to both the transplant and host tissue, an extensive battery of tests would be required to rule out label effects. Although

a reasonably high-throughput battery could be set up to encompass a wide range of potential effects, this would not be a time- or cost-effective solution for most laboratories. Therefore for each labeling application, the utility of the label versus other methods must be weighed against the assays required to show a lack of label effects on cell function.

2.4.3 Future use of exogenous labels

The results shown here, taken along with previous studies, suggest that where immunohistochemistry can be used to identify transplanted cells, that would be preferable to using any kind of labeling. However, this is not always possible. Xenografts provide an easy way to distinguish between transplanted and host cells, but are not always the preferred paradigm. Indeed, they bring extra problems of their own in the form of immunocompatibility issues requiring immune suppression. Additionally, not all protein structures are so highly conserved that cells of any mammalian species can be transplanted into any other with the same results. Allografts therefore have distinct advantages, and with the advent of widely available iPSC technology, autografts may become more commonplace. In these instances, there may be no antibody-detectable differences between transplanted and host cells, necessitating the use of an exogenous marker. Additionally, in the tissue engineering field, transplants are becoming increasingly complex and may require transplantation of more than one cell population. This again makes it more challenging to find sufficient immunohistochemical differences for antibody detection alone.

2.5 Conclusion

Rigorous testing of histological labels is of great importance, particularly as much is yet unknown about the therapeutic mechanism of transplanted cells. Simple viability assays are not sufficient to reveal the complete nature of a label's effects on cell biology. All labels tested here showed some effect on NSC proliferation and differentiation, indicating that caution should be exercised in their use with this cell type. In vitro co-culture showed high levels of label leakage and as such was a poor predictor of in vivo reliability, where false negatives were a more significant problem than false positives. This study shows different results to other previous reports, showing that the cell type, labeling protocol and in vivo paradigm are all likely to affect the reliability of tracking labels. It is therefore recommended that labels are thoroughly tested on the specific cell type and in the proposed disease model before relying on their validity. In vivo results showed little difference in label reliability. However, of those tested, BrdU would be the label of choice due to its reduced cellular effects, and ease of identification due to the label's nuclear localisation.

Chapter 3: Gadolinium-Gold nanoparticles for identifying transplanted cells using MRI

3.1 Introduction

Magnetic Resonance Imaging (MRI) is a powerful tool, with good spatial resolution and no tissue depth limitations, affording longitudinal studies in the same population of animals. In the context of stroke, MRI is used clinically for diagnosis, to differentiate between haemorrhagic and ischemic stroke and to predict prognosis (Ahmed and Masaryk 2004). Preclinically, MRI is used in conjunction with behavioural assessment to determine the efficacy of potential therapies in rodents and primates (Bihel, Pro-Sistiaga et al. 2010, Boltze, Schmidt et al. 2012). As well as reducing the number of experimental groups required for anatomical assessment over a number of time points as compared to histology, the number of animals required per group can also be reduced due to the increased statistical power of paired observations for a given effect size (Modo 2009). In order to correlate the location and migration of transplanted cells with anatomical and behavioural changes, it is necessary to visualise both the transplanted cells and lesion anatomy over time. This presents a challenge due to the spatial resolution of MRI, which, although high compared to other in vivo imaging modalities, is relatively low when compared to histology. However, recent increases in magnetic field strength allow improved signal to noise ratio in shorter imaging times, and advances in contrast agent design are further improving sensitivity. In order to visualise transplanted cells, however, a high intracellular concentration of contrast agent is required, which is likely to have detrimental effects on cell biology (Brekke, Morgan et al. 2007).

3.1.1 T1 and T2 Agents

Most commonly used MRI contrast agents can be split into two categories based on whether they predominantly affect the T1 or T2 properties of the labeled material. In terms of stroke, one important aspect of assessing potential therapies over time would be to analyse the effects of therapies on the anatomy of the lesion, such as volume and topology (Modo, Beech et al. 2009, Smith, Stroemer et al. 2011). Both T1w and T2w MR images show the lesion anatomy (**Figure 3.1**). However, the T1w image is fairly flat, with the exception of the lesion and ventricles, which are hypointense. The T2w image shows improved tissue contrast and anatomical detail, with hyperintense lesion and ventricles, and hypointense white matter.

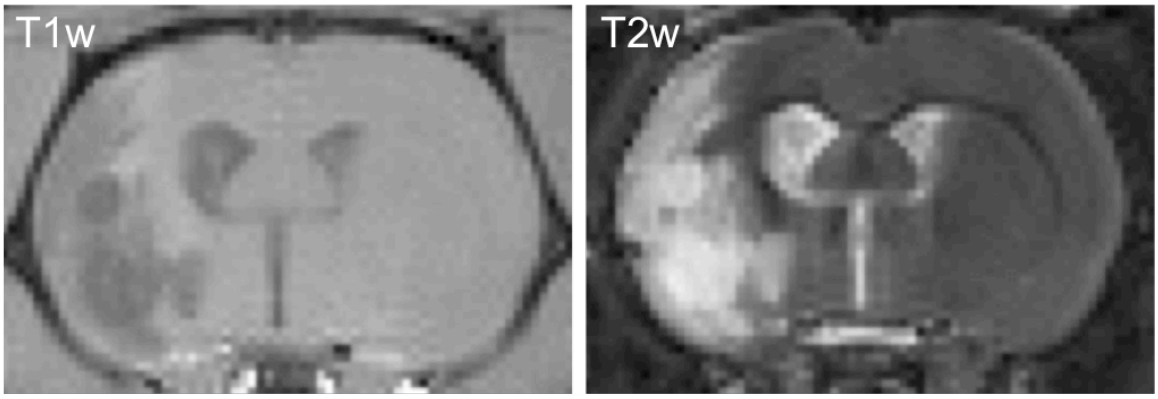

Figure 3.1 T1w and T2w images of a stroke-lesioned rat brain. In the T1w image, the lesion is visible as a hypointense area, but there is very little hyperintensity within the brain tissue. The T2w image shows the lesion as hyperintense, with additional anatomical detail such as hypointense white matter.

The most commonly used cell tracking method is currently Superparamagnetic Iron Oxide (SPIO) particles (Tang, Sha et al. 2013), which have excellent sensitivity and therefore provide a low cell detection threshold. However, their predominant effect is on T2 shortening, producing a hypointensity that may be confused with naturally occurring phenomena, such as hematoma and white matter, which also produce T2 hypointensity. Gadolinium(III) (Gd^{3+}), however, is predominantly a T1 agent, although it does have both T1 and T2 shortening effects. However, the advantage is that naturally occurring phenomena are very unlikely to produce a T1 hyperintensity, making the signal highly specific to the transplanted cells. A range of Gd based agents are in clinical use, for CNS imaging e.g. Gd-DTPA (Magnevist) and Gd-HP-DO3A (ProHance) (Kanal, Maravilla et al. 2014). For cell tracking, a high intracellular concentration of agent is required, but free Gd^{3+} ions are highly toxic to cells, making the thermodynamic stability of the chelate of great importance to allow uptake of sufficiently high concentrations of agent without compromising cell viability (Cabella, Crich et al. 2006). A previous Gd agent design, GRID, showed good cell uptake and a useful fluorescence moiety (Brekke, Morgan et al. 2007), but was later shown to impact therapeutic efficacy (Modo, Beech et al. 2009). The Meade lab have since worked on improving the design of this agent, and we here test the next generation, GdAuNPs.

3.1.2 GdAuNPs

GdAuNPs retain the characteristics of bimodality, including a Cy3 moiety, and good cell uptake. The macrocyclic chelate HPDO3A is used rather than the linear DTPA used in GRID, which reduces the potential for release of free toxic Gd ions. Gold nanoparticle (AuNP) synthesis has been developed over the last half century, and optimized methods are now high-yielding and reliable. The gold itself is visible by Computed Tomography (Popovtzer, Agrawal et al. 2008) and

Electron Microscopy (Horisberger and Rosset 1977), and the large surface area is highly functionalizable. Thiols, phosphines and amines have a high affinity for gold, and these can be used as anchors to allow further functionalization through, for example, oligonucleotides. However, care must be taken, since observed toxicity of AuNPs is normally due to functionalization moieties rather than the gold itself (Daniel and Astruc 2004).

Oligonucleotide-AuNP conjugates (DNA-AuNPs) have found many uses, as oligonucleotide loading imparts useful particle characteristics. Higher loading leads firstly to higher particle stability, which is thought to be due to the attraction of Na^+ to the particle surface, resulting in inhibition of DNase enzymes (Seferos, Prigodich et al. 2009). Secondly, high oligonucleotide loading leads to improved cellular uptake due to increased protein adsorption onto the surface of the nanoparticle, facilitating interaction with the cell membrane (Giljohann, Seferos et al. 2007). These properties make it an excellent candidate for cell tracking applications, where high intracellular concentration and long-lasting signal are important. The previous version of the particle showed improved relaxivity (Song, Xu et al. 2009), and this has since been further optimised by Matthew Rotz at Northwestern. The molecular parameters governing water exchange (tau m) and rotational correlation time (tau r) have been improved and optimised for high field.

We here aim to test the utility of GdAuNPs for identifying neural stem cells after transplantation into the rat brain.

3.2 Methods

3.2.1 Particle synthesis

Particle synthesis was performed by Matthew Rotz at Northwestern.

All reagents and solvents were purchased from Sigma-Aldrich unless otherwise stated. Citrate stabilized AuNPs (15.3±1.4 nm) were synthesized by a previously described protocol (**Figure 3.2**). Oligonucleotides were synthesized on solid phase CPGs by standard techniques on a MerMade automated synthesizer. All reagents and protected 3' Thiol modifier CPGs and C6 amino modifier dT modified bases were purchased from Glen Research (Sterling, Va). Oligonucelotides were deprotected from the solid phase using AMA conditions [(1:1 methylamine:ammonium hydroxide (*sat.*)] for one hour. Purification was performed using reverse phase high performance liquid chromatography (HPLC) on a Varian HPLC using a mobile phase consisting of 30mM triethyl ammonium acetate buffer pH 7 (TEAA) and acetonitrile (ACN). Separation was achieved using a gradient of 75% Acetonitrile over 45minutes, as monitored by DNA backbone and Cy3 wavelengths at 254 and 546 nm respectively. Purified oligonucleotides were stored at 4 °C until particle synthesis. Inorganic Gd(III) complex **5** was synthesized using standard organic chemistry techniques (vide infra). Characterization was achieved using a Varian 500 MHz NMR and a Bruker AutoFlex III MALDI spectrometer.

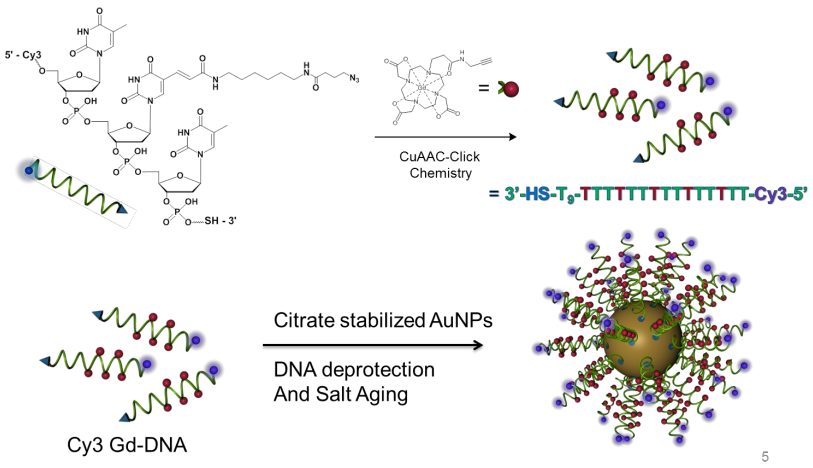

Figure 3.2 Schematic showing the steps of particle synthesis

3.2.2 Inductively Coupled Plasma Mass Spectrometry (ICP-MS)

ICP-MS was performed by Matthew Rotz at Northwestern.

Quantitation of Au and Gd was accomplished using ICP-MS of acid digested samples. Specifically, 60 µl of TraceSelect nitric acid (> 69%, Sigma) and 60 µl of TraceSelect HCl (fuming 37%, Sigma) was added to a 15 mL centrifuge tube. To this acid is added a 5 µl aliquot of Gd(III) DNA AuNPs. Nanopure H_2O and multi-element internal standard were added to produce a solution of 2% nitric acid (v/v), 2% HCl (v/v) and 5.0ng/ml internal standard up to a total sample volume of 3 mL for analysis of Gd(III) content. Gold samples were prepared in a similar fashion, but diluted 10 fold and analysed in a total volume of 10 mL. Individual Au and Gd(III) elemental standards were prepared at 0.500, 1.00, 5.00, 10.0, 25.0, 50.0, 100, and 250ng/ml concentrations with 2% nitric acid (v/v), 2% HCl (v/v) and 5.0ng/ml internal standards up to a total sample volume of 10ml. ICP-MS was performed on either a computer-controlled (Plasmalab software) Thermo (Thermo Fisher Scientific) PQ ExCell ICP-MS equipped with a CETAC 500 autosampler or a computer-controlled (Plasmalab software) Thermo X series II ICP-MS equipped with an ESI (Omaha) SC-2 autosampler. Each sample was acquired using 1 survey run (10 sweeps) and 3 main (peak jumping) runs (100 sweeps). The isotopes selected were ^{197}Au, ^{156,157}Gd and ^{115}In, ^{165}Ho, and ^{209}Bi (as internal standards for data interpolation and machine stability). Particle concentrations were calculated from resultant ICP concentrations of Au by approximating the number of gold atoms per particle through the use of particle diameter and the density of atoms in bulk gold (here 98,247 Au/AuNP).

3.2.3 Relaxivity at 1.41T

Relaxivity measurements were performed by Matthew Rotz at Northwestern

A concentrated stock of Gd(III)-DNA AuNP conjugates was obtained (700µl). From this stock, an aliquot of 300µl was serially diluted for a total of five solutions. The five solutions were heated to 37°C and 250µl of each concentration was placed into a Bruker minispec mq60 NMR spectrometer (60 MHz) for measurement of T1 relaxation time. Data was collected using an inversion recovery pulse sequence, with a 15s repetition time and 10 data points (average of 4 measurements per point). The remaining volumes of each solution were utilized for ICP analysis of [Gd(III)]. The inverse of the longitudinal relaxation time (1/T1, s-1) was plotted versus the

Gd(III) concentration (mM). By applying a linear fit to this data, the slope generated is reported as the relaxivity of the agent (mM-1 s-1). Lines were fitted with $R^2 > 0.99$.

3.2.4 Stability and shelf life analysis

These experiments were performed by Matthew Rotz at Northwestern

To assess loss of gadolinium from particles over time, concentrated stock was centrifuged, the supernatant decanted and particles resuspended in 0.1x Hank's Balanced Salt Solution (HBSS) at approximately 55nM AuNP per tube and stored either at 4°C or 37°C. ICP-MS was used to quantify the initial particle concentrations, including total Gd(III) content per tube. Particles were stored for 24 hours, at which time they were vortexed and centrifuged (30 minutes at 4°C, 21,000g). A sample of the supernatant was removed (containing no AuNPs), which was analysed for Gd(III) content. The Gd(III) content measured was normalized to the initial Gd(III) concentration of each tube, and quantified as percentage of Gd(III) lost from the particle surface into the surrounding solution. This process was repeated in 24 hour increments for a period of two weeks.

In parallel with shelf life stability experiments, a separate aliquot of particles was measured for r_1 and r_2 relaxivities the first day after conjugation. Less the particles used for ICP analysis, particles were recovered and reconcentrated after the measurement of relaxivity and then placed back into storage at 4°C. This process was repeated on days 8 and 17.

3.2.5 Cell labeling

STROC05 human neural stem cells were cultured as in section 2.2.2.1. Particles were diluted to the required concentration (0.02, 0.2 2 or 20nM AuNP) in complete growth medium supplemented with an additional 2% Human Albumin Solution to improve particle uptake via surface protein adsorption (Giljohann, Seferos et al. 2007). This was then added to the cell monolayer, and incubated for 24 hours before washing 3x with HBSS and fixing or harvesting.

3.2.6 In vitro assays

To assess particle uptake by ICP-MS, cells were seeded in 48 well plates at 150,000 cells/well and labeled with different particle concentrations. They were then washed five times with HBSS and harvested using Accutase. An accurate cell count was then obtained using a haemocytometer and the cell suspension was sent to Northwestern for ICP-MS as in 3.2.2.

The Cy3 moiety could be detected using fluorescence microscopy, so images were taken using consistent microscopy parameters, and all images were acquired in a single session. These were then run through a simple MATLAB code (see Appendix 1) to determine the mean intensity of images acquired using this filter set, and the resulting number was divided by the cell number in the image (DAPI count) to give relative fluorescence units (RFU) per cell. The RFU per cell of unlabeled cells was subtracted to control for background.

Assays for cell survival, proliferation and differentiation were conducted as in 2.2.4.2 and 2.2.4.3.

3.2.7 MR Imaging

MRI sequences were designed and implemented by Wen Ling. All imaging was performed on a 9.4T Varian system using a volume quadrature coil with inner diameter 38mm (Virtumed). The parameters used for different image acquisitions are shown in **Table 3.1**. Slice thickness was 0.5mm throughout.

Table 3.1 MR Imaging parameters used for different samples

			TR(s)	TE(ms)	Averages	FOV
In vitro	Solutions	T1 map	10.4	40	1	45x30mm
		T1w	0.5	2.02	1	
		T2 map	5	15 to 480	1	
		T2w	2	27.87	1	
	Cells	T1 map	12.2	40	1	45x25mm
		T2 map	3	15 to 480	1	
		T2w	3	32.74	1	
In vivo		T1 map	10.4	40	1	30x30mm
		T1w	0.5	2.73	6	
		T2 map	4	7.2 to 229	2	
		T2w	6.1	70.78	8	
Ex vivo		T1 map	15.4	40	1	30x30mm
		T2 map	6	7.2 to 229	2	
		T2w	6.1	70.78	8	

T1 maps were acquired using global Inversion Recovery (IR) with fast spin echo (FSE) readout with Ti values of 0.01, 2, 4, 6, 8, 10 and 10.2s.

T1w images were acquired using a Gradient Echo Multi Slice (GEMS) sequence, T2w images using FSE and T2 maps using Multi Slice Multi Echo (MSME) with 32 echoes, where TE was varied between each echo by 15ms in vitro or by 7.2ms in vivo.

For ex vivo T1 maps using different voxel sizes, the FOV was kept constant at 30x30mm, slice thickness 0.5mm. Matrices of 48x48, 64x64, 96x96, 128x128, 192x192 and 256x256 were then used to produce voxel volumes of 195, 110, 49, 28, 12 and 7nl. For in vitro cell suspension phantoms, an FOV of 45x25mm and slice thickness of 0.5mm were used with matrices of 64x32, 96x48, 128x64, 192x96, 256x128, 384x192 and 512x256 to give voxel volumes of 4, 8, 17, 31, 69, 122 and 275nl.

3.2.7.1 In vitro

For cell pellet phantoms, labeled cells were washed 3 times in HBSS, harvested, counted and centrifuged in 0.1ml PCR tubes (Axygen) in PBS. They were then placed into a block of agar gel for imaging.

For cell suspension phantoms, labeled and unlabeled cells were washed 3 times in HBSS, harvested, resuspended in PBS and counted. They were then suspended at 10, 50, 100, 150 and 200 thousand cells/µl in a final concentration of 6% gelatin in PBS, taking into account the cell volume as in section 2.2.5.1. The Gd concentration of each phantom was calculated from the known cell density and cell uptake of GdAuNP. This could then be plotted against R1 ($1/T_1$) and a linear fit applied to give the relaxivity (r_1) in $mM^{-1}s^{-1}$.

3.2.7.2 In vivo

Labeled cells were washed 3 times in HBSS, harvested and resuspended in PBS for counting. If cell viability was <85%, cells were not taken forward to transplant. Cells were then spun down and resuspended at 125,000 cells/µl in 4mg/ml Extracellular Matrix (ECM) hydrogel, kindly provided by Stephen Badylak. Stereotactic surgery was performed as described in section 2.2.5.2, using the same coordinates, with a total of 5µl of cell suspension injected per site. Labeled cells were transplanted into the right hemisphere and unlabeled cells in the left in a total of 5 animals. One animal received a total of six cell injections (3 of labeled cells, and 3 unlabeled) at different cell densities to give a total of 250,000, 625,000 or 1,000,000 cells per site. The remaining 4 animals all received only 2 injections each, of 625,000 labeled and unlabeled cells.

MRI was performed 24 hours after transplant for all animals. 3 were then sacrificed for ex vivo MRI and histology. The remaining 2 were scanned again at 7 days before sacrifice. Animals were anesthetized with Isoflurane (4% for induction, 2% for maintenance), and body temperature was maintained using a homeothermic water bed controlled via a rectal temperature probe. Breathing was monitored using a pressure sensitive “bubble” placed beneath the chest, with a Biopac system.

On sacrifice, perfusion was carried out as in section 2.2.5.3. For ex vivo scans, brains were secured in a 50ml falcon tube of PBS. For the animal that received six injections, the brain was scanned immediately after perfusion and T1 contrast was consistent with that observed in vivo.

For the others, the brains were stored in PBS at 4°C for up to 2 weeks before imaging. There was no T1 contrast evident for labeled cells, even when contrast had been apparent on in vivo scans. This was attributed to a storage issue, and the results from the ex vivo scans were therefore excluded from analysis.

Histology, Immunohistochemistry and image capture and analysis were conducted as in Chapter 2.

3.2.8 Statistics

Statistical tests were performed using Prism 5.0f (GraphPad). For cell survival and proliferation, ANOVAs were used to compare each label concentration with unlabeled controls. For differentiation, Mann Whitney tests were used. Pearson correlation was used to correlate SNR with voxel size. To generate the contour map showing the in vivo effect of voxel size and cell number on T1, Minitab Software was used.

Values were considered significant where $p<0.05$. For in vitro assays, three biological replicates, each with three technical replicates were conducted to give n=9 (unless otherwise stated).

3.3 Results

3.3.1 Nanoparticle characterization

GdAuNPs were designed to provide high payload delivery of GdHPDO3A, bearing improved high-field relaxivity per Gd. Oligonucleotides with a Cy3 moiety were synthesized, and click chemistry was used to conjugate these to GdHPDO3A complexes. This DNA was then loaded onto the surface of 13nm gold nanoparticles to produce GdAuNPs with ~500 GdHPDO3A per particle (**Figure 3.3**A).

Prior to the co-incubation of particles with cells, particle relaxivity (R_1 and R_2) was measured at 1.41T over a two week period, and was shown to remain consistent (**Figure 3.3**B). The amount of Gd released from the particles into solution was also measured in order to assess the stability of the particles and indicate a potential shelf life. When particles were stored at 4°C, no Gd loss was observed over two weeks, showing that particles can safely be stored for two weeks between production and use. However, when particles were incubated at 37°C, a small but steady loss of Gd was observed at a rate of ~0.4% of total Gd per day, resulting in a cumulative loss of <6% of total Gd over 2 weeks (**Figure 3.3**C). This indicates that physiological temperatures negatively impact particle stability, but only to a very small degree. However, particle stability in vivo would also be affected by pH and the presence of enzymes, potentially resulting in lower stability in vivo.

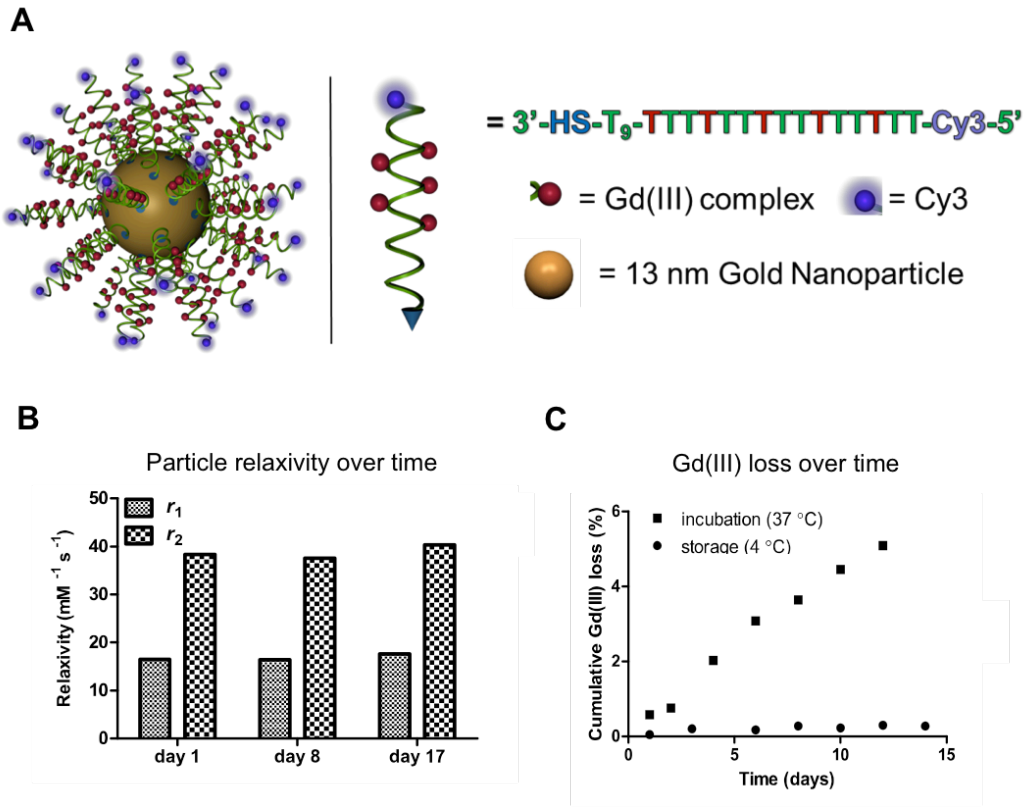

Figure 3.3 GdAuNPs. Particles consist of a gold nanoparticle core loaded with DNA to which the GdHPDO3A and Cy3 moieties are attached (A). Particles retain their relaxivity properties (1.41T) over more than 2 weeks (B). There is a small amount of Gd(III) loss at 37°C, amounting to <6% of total Gd over 2 weeks. However, loss is negligible (<0.5%) when particles are stored at 4°C (C).

To test particle performance at high field compared to GdHPDO3A (ProHance), solutions of GdAuNPs and GdHPDO3A at the same Gd concentration were imaged at 9.4T, and R1 and R2 maps were generated (**Figure 3.4**A). Plotting Gadolinium concentration against R1 gave a molar relaxivity (r_1) of 6.68$mM^{-1}s^{-1}$ for GdAuNPs, which was over twice that of GdHPDO3A at 3.07$mM^{-1}s^{-1}$(**Figure 3.4**B), and r_2 was 13 times higher for particles (**Figure 3.4**C). The increase in relaxivity seen with GdAuNP compared to ProHance is due to particle design improving molecular parameters, such as water exchange (tau m) and rotational correlation time (tau r).

When relaxivity is expressed per mole of particles, rather than per Gd(III), the comparison to GdHPDO3A becomes skewed, here showing a relaxivity of 2548$mM^{-1}s^{-1}$ (**Figure 3.4**D), which is 830 times that of GdHPDO3A (**Figure 3.4**E). Therefore measurements such as relaxivity should not be expressed on a per particle basis.

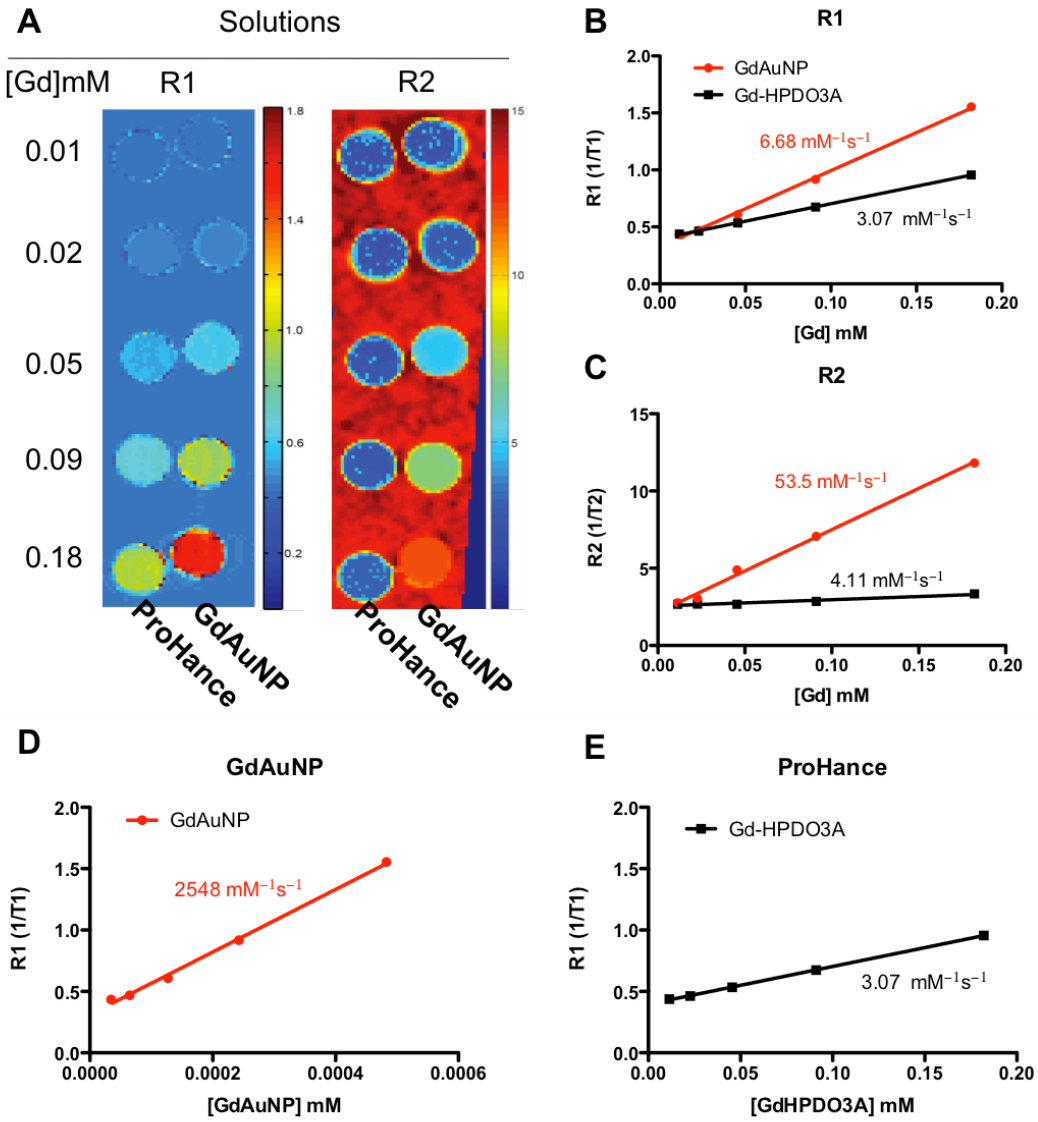

Figure 3.4 MRI of GdAuNP compared to ProHance (GdHPDO3A) at 9.4T. R1 and R2 maps were generated (A). GdAuNP was shown to have 2.2x the R1 molar relaxivity of GdHPDO3A (B) and 13x the R2 relaxivity. Expressing r_1 relaxivity on a "per mole of particles" basis suggested that r_1 was 830x higher in GdAuNP (D) compared to GdHPDO3A (E).

3.3.2 Cell uptake

The factor having the largest effect on sensitivity of detection is the intracellular Gd concentration (Song, Xu et al. 2009). It is therefore important to maximise intracellular Gd concentration without impacting cell survival and phenotype. In order to first assess particle uptake into cells, STROC05 NSCs were incubated for 24 hours with GdAuNPs diluted in growth medium at a range of particle concentrations (**Figure 3.5**A). Cy3 fluorescence could be seen even at the lowest concentration of 0.02nM particles (**Figure 3.5**B), and the particles generally appeared to be colocalized with nestin (green, **Figure 3.5**C), showing a cytoplasmic localization. The amount of Gd per cell was

measured by ICP-MS (**Figure 3.5**D), and Cy3 was measured by relative fluorescence per cell (**Figure 3.5**E), with both showing a similar pattern of uptake across incubation concentrations. The uptake appears to be an active process, since the resulting intracellular concentration was higher than that of the incubation solution. For example, at 20nM particle concentration, the incubation concentration was ~7µM Gadolinium given a loading of 350Gd/particle, whereas the final intracellular concentration was 56µM. This is due to the Oligo-DNA coating, which has previously been shown to increase particle uptake (Giljohann, Seferos et al. 2007).

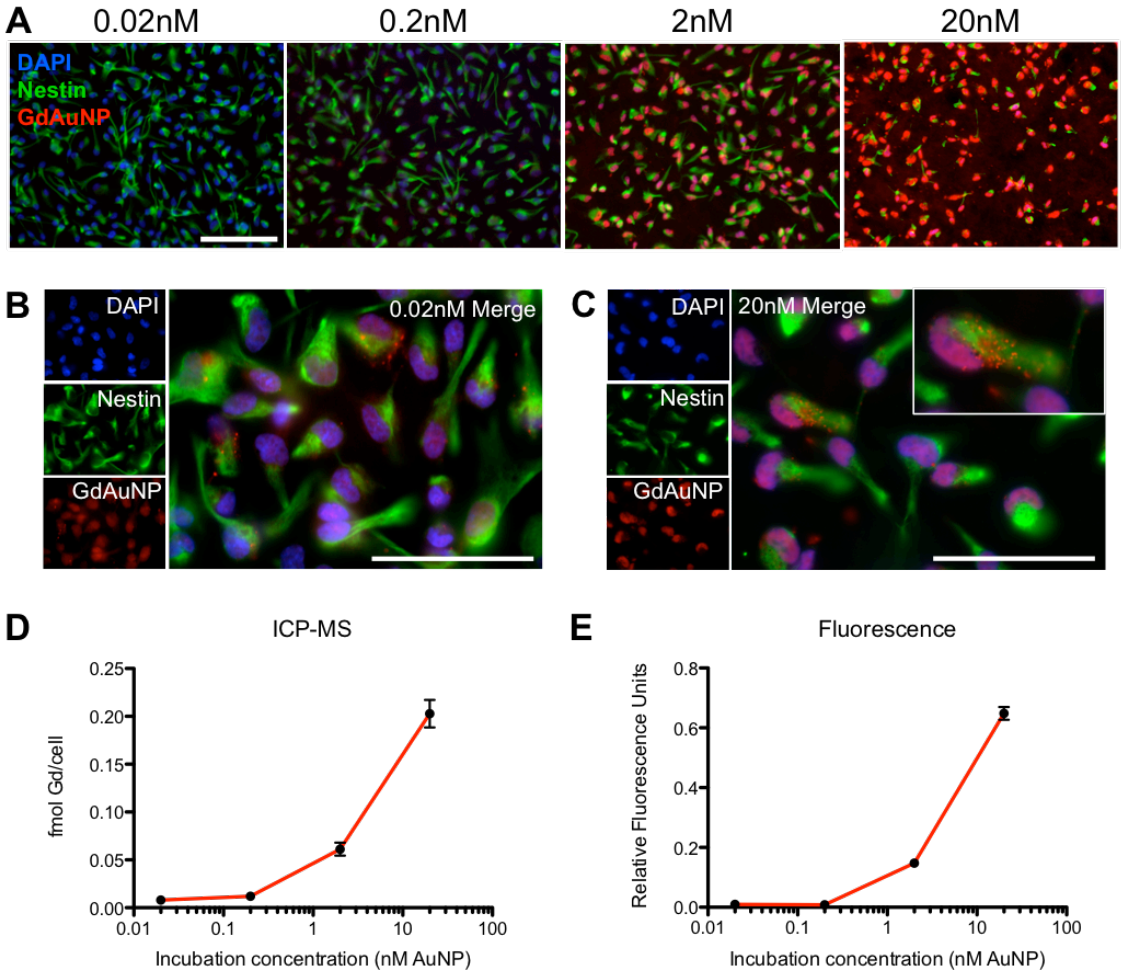

Figure 3.5 Cell Uptake of GdAuNPs at different particle incubation concentrations, shown by the fluorescent Cy3 moiety (red, A, scale bar = 200µm). Fluorescence was visible even at the lowest concentration (B, scale bar = 100µm) and appeared to be localized to the cytoplasm (C). Cell uptake was measured by ICP-MS (D) and RFU per cell (E).

3.3.3 Cellular effects in vitro

GdAuNPs generally seemed to be well tolerated by NSCs. Labeled cells were cultured under proliferation conditions overnight, or for seven days in differentiation medium and than stained

with DAPI and Ki67, a marker of cell proliferation (**Figure 3.6**A). Cell survival was assessed using a DAPI count, and was not significantly affected at either day zero or day seven at any particle concentration (**Figure 3.6**B). There appears to be a trend toward decreased survival at day zero for the 20nM particle concentration, but this is not statistically significant (p=0.19). Cell proliferation was assessed by counting the percentage of total cells expressing Ki67 protein (**Figure 3.6**C). The expected behaviour of down-regulation of Ki67 during a seven day differentiation protocol was observed, and this was unaffected by increasing particle concentration. At higher concentrations of 50, 100 and 200nM particles (n=1 well per concentration), the majority of cells died during the incubation period. It was therefore determined that 20nM was the maximum tolerated concentration. In order to assess if this concentration was suitable to take forward for imaging experiments, the effect on cell phenotype was assessed. The percentage of cells expressing GFAP (as a marker for astrocytic cells), and Tuj (Beta-III-Tubulin, for neuronal cell types) was compared between unlabeled cells and those labeled with 20nM particles. There was no significant change observed in cell phenotype (**Figure 3.6**D), showing an absence of cell type specific toxicity, or effects on differentiation.

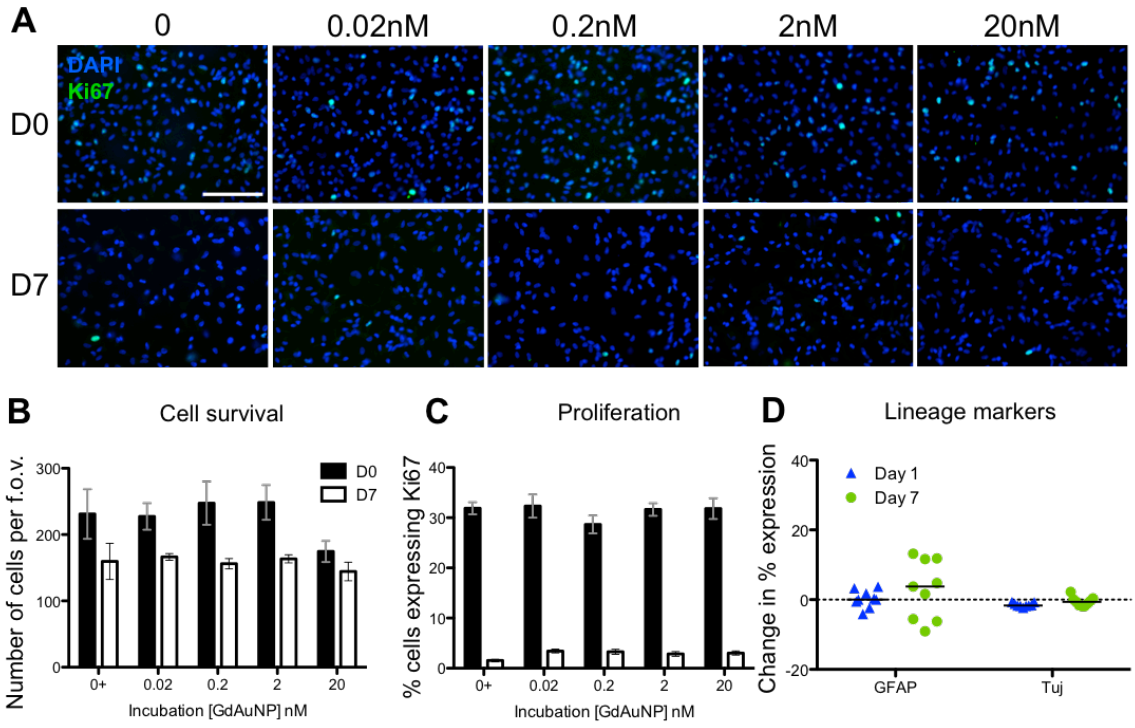

Figure 3.6 Effects of GdAuNPs on neural stem cell biology. Cells at day 0 and day 7 after labeling were stained with DAPI and Ki67 (A, scale bar = 200μm). No significant effects were seen on the number of surviving cells at any concentration of GdAuNP at day 0 (p=0.19) or day 7 (p=0.63) (B) or on the percentage of cells expressing Ki67 at day 0 (p=0.63) or day 7 (p=0.30) (C). Cells were also stained to assess phenotypic changes, and no significant differences were seen between those labeled at 20nM particles and controls (GFAP, p=0.60; Tuj, p=0.49) (D).

3.3.4 Batch variability

With new particle types, variability between particle batches is a common concern, and characterisation of only a single batch can lead to un-representative data that is later found to be irreproducible. Here, batches of particles were prepared separately for direct comparison, and assessed for consistency of cell uptake and survival effects. The loading of the batches showed noticeable variation (Batch 1 = 248Gd/NP; Batch 2 = 345Gd/NP; Batch 3 = 350Gd/NP), and therefore the particle concentration (rather than Gd concentration) was standardised across experiments. This resulted in a high consistency of Au/cell across batches (**Figure 3.7**A), whereas small differences can be seen in Gd/cell, particularly a lower Gd/cell for Batch 1 compared to 2 and 3 (**Figure 3.7**B).

Cell survival at day 1 was also compared across the three particle batches in order to assess any differential toxicity between batches (**Figure 3.7**C). The three batches performed consistently despite the range in incubation concentration of Gd (from 5μM in Batch 1 to 7μM Gd in Batch 3 at 20nM AuNPs), and no difference was seen in cell survival.

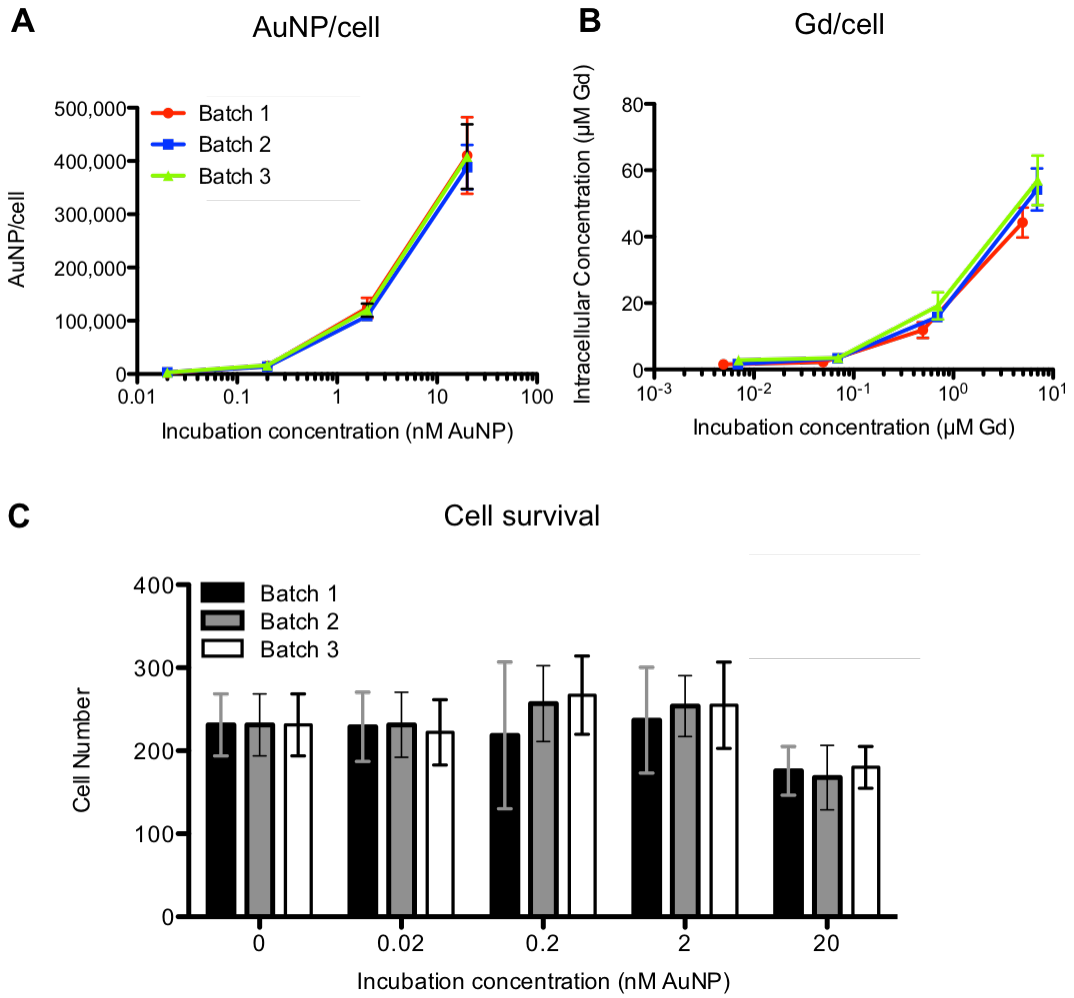

Figure 3.7 Batch Variability. Three separate batches of GdAuNPs were prepared and used to label cells. AuNP uptake was consistent across batches (A), and Gd/cell varied with the Gd-loading of each batch of AuNPs (B). Cell survival was also consistent across batches and concentrations (C).

3.3.5 Effect of GdAuNP labeling on MRI of cell pellets

In order to verify that the level of Gd uptake provided sufficient contrast for MRI detection, labeled cells were pelleted and imaged at 9.4T. Cells were labeled either with GdAuNP or with GdHPDO3A at the same incubation concentration of Gd, and R1 and R2 maps were generated comparing these to blank cells and buffer (**Figure 3.8**A). Cells labeled with GdHPDO3A showed only a minor difference in R1 compared to blank cells, but GdAuNP-labeled cells showed a large increase in R1 (**Figure 3.8**B). This result was attributed to a combination of higher intracellular concentrations of Gd and the superior molar relaxivity of the particles compared to ProHance. Changes in R2 followed the same pattern (**Figure 3.8**C), but appeared less dramatic than previously seen with solution phantoms. This may due to the low concentration here (56μM),

where differences in T1 have been shown to be more marked than differences in T2 (May and Pennington 2000).

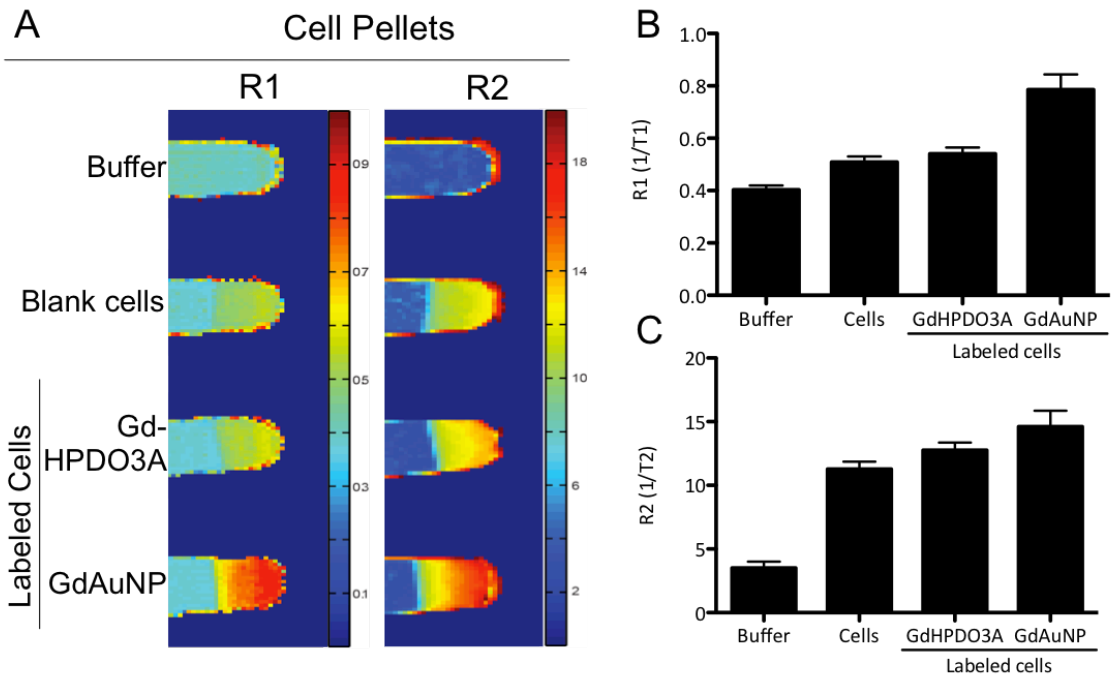

Figure 3.8 MRI of cell pellets in vitro. Blank cells, and cells labeled either with Gd-HPDO3A or GdAuNP were imaged at 9.4T and R1 and R2 maps were generated (A). Cells labeled with GdAuNP showed increased relaxivity compared to blank cells and those labeled with Gd-HPDO3A, both R1 (B) and R2 (C).

3.3.6 Effect of cell density and voxel size on MRI detection

Parameters such as voxel size are often decided based on scanning time and image resolution, but voxel size can also affect the efficiency of a contrast agent. To investigate these effects, labeled cells were suspended in gelatin at varying cell densities and imaged at 9.4T. At a constant field of view (FOV) and slice thickness, the matrix size was varied to give 6 different voxel volumes ranging from 4 to 275nl (**Figure 3.9**A). Signal to noise ratio increased with increasing voxel size (Pearson correlation $p<0.01$), whereas the difference in R1 between labeled and unlabeled cells decreased as voxel size increased ($p<0.01$) **Figure 3.9**B). This effect could be attenuated by selecting an ROI which included only the centre of the sample, excluding the coronal area which would be susceptible to partial volume effects with increasing voxel size. When the centre ROI was selected, the correlation with voxel size became insignificant ($p=0.12$, **Figure 3.9**C).

Relaxivity is affected by the microenvironment of the contrast agent. The r_1 molar relaxivity of GdAuNPs in cells was calculated as 3.87mM^{-1}s^{-1} (**Figure 3.9**D), which is considerably lower than their molar relaxivity in solution, which was 6.68mM^{-1}s^{-1}. This is likely due to a combination of reduced water access, due to water having to cross the cell membrane to interact with the Gd complex, and the presence of intracellular proteins. Their interaction with the Gd complex can affect the tumbling frequency of Gd, thereby reducing its relaxivity.

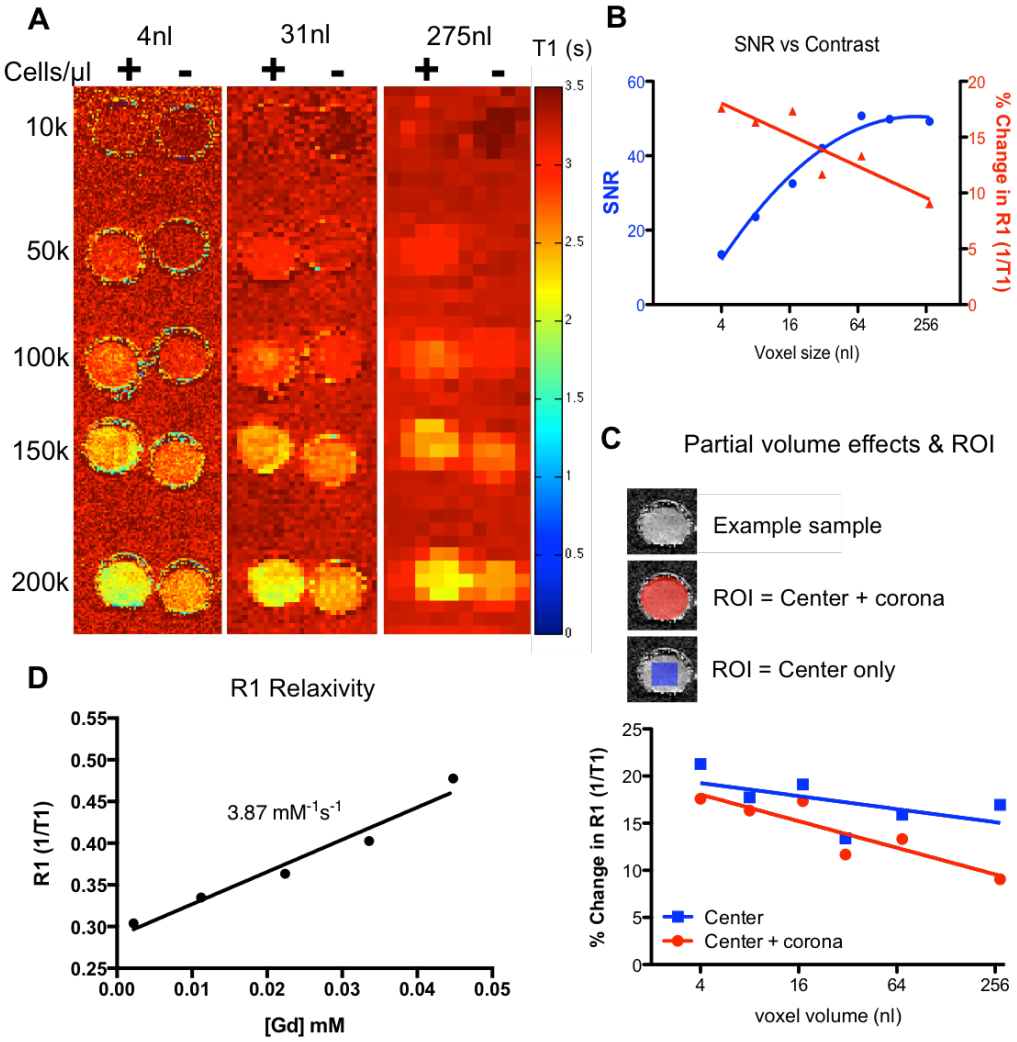

Figure 3.9 Labeled and unlabeled cells were suspended in gelatin at different cell densities (A, **+** = labeled cells, **-** = blank cells). Increasing voxel size had higher SNR but less contrast between labeled and unlabeled cells (B). The decrease in contrast could be attenuated by selecting ROIs in the centre of the sample to avoid partial volume effects (C). The relaxivity of GdAuNPs in cells is 3.87mM^{-1}s^{-1} (D).

3.3.7 Cell detection in vivo

To assess cell visibility on MRI in vivo, labeled and unlabeled cells were transplanted into healthy rat striatum and MR images were taken the following day. Labeled cells were clearly visible on T1w images (**Figure 3.10**A, right hemisphere), whereas unlabeled cells showed no change in contrast (left hemisphere). T2w images showed only some oedema and tissue damage, with neither labeled nor unlabeled cells visible. This was supported by histology, where transplanted cells in the right hemisphere showed red fluorescence consistent with the Cy3 moiety of GdAuNPs, whereas this was absent from unlabeled cells in the left hemisphere. Both populations were visible using human nuclear antigen (HNA).

At higher magnification, both Cy3 fluorescence and dark spots consistent with gold were observed within the graft (**Figure 3.10**B). GdAuNP were well colocalized with HNA staining, with 71% of cells being positive for both HNA and GdAuNP (**Figure 3.10**C). False negatives (HNA+, GdAuNP-) were more numerous than false positives (HNA-, GdAuNP+) at 29% compared to <0.5%. This suggests that the MR contrast in vivo is more likely to be an underestimation of transplanted cells than an over-estimation.

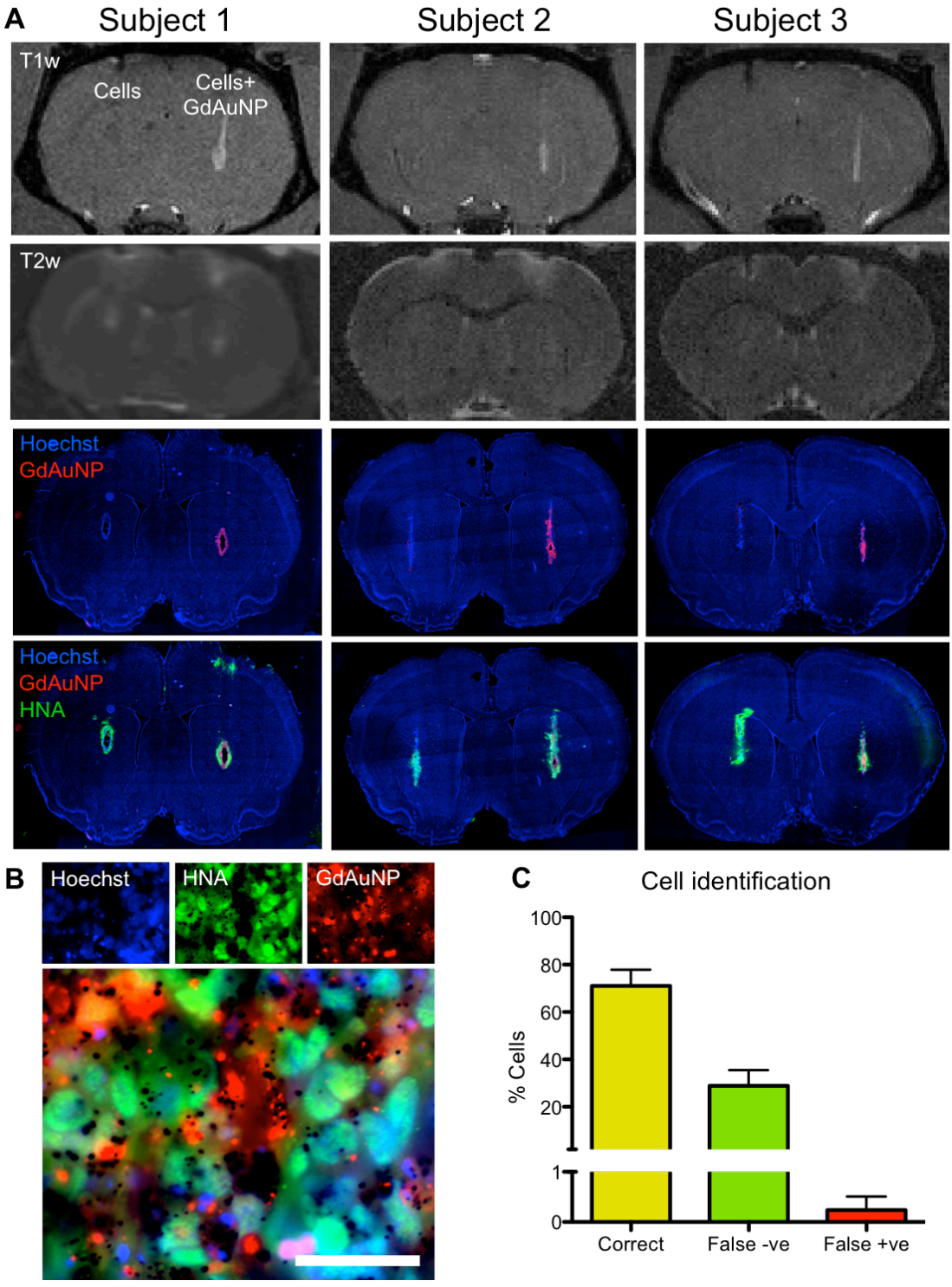

Figure 3.10 Transplanted GdAuNP labeled cells are clearly visible on T1w MR images, whereas unlabeled cells in the left hemisphere are not. Neither are visible on T2w images. Histology shows GdAuNP (red) and HNA labeling all transplanted cells (green, A). A higher magnification image shows good colocalisation of HNA and Cy3 (B, scale bar = 100μm), which is supported by the counts showing a high level of correct cell identification (C).

3.3.8 Serial imaging of transplanted cells over one week

One of the benefits of MRI is the ability to image over time in the same animals in order to track anatomical changes and assess their correlation with the behaviour of transplanted cells. However, contrast agents often remain visible after cell death, generating false positive detection (Berman, Galpoththawela et al. 2011). In order to assess whether GdAuNP continue to generate T1 hyperintensity after cell death, labeled and unlabeled human cells were transplanted into the rat brain without immune suppression and allowed to die over 7 days. MR images were obtained after 24 hours while cells remained viable, and again at day 7 when very few transplanted cells were detected by histology. Both animals showed the expected hyperintensity on T1w images at day 1, but this contrast had largely disappeared by day 7 (**Figure 3.11**). When this was compared with histology, very little staining was seen either for GdAuNPs or HNA, which is indicative of very low cell survival. This shows that upon the death of transplanted cells, the remaining agent is not detected in the extracellular space or within host cells. This is likely due to the presence of high levels of DNases such as CAD (Caspase Activated Deoxyribonuclease) during apoptosis, which may break down the oligonucleotide component of GdAuNPs, thereby leaving GdHPDO3A in solution and below the MRI detection threshold.

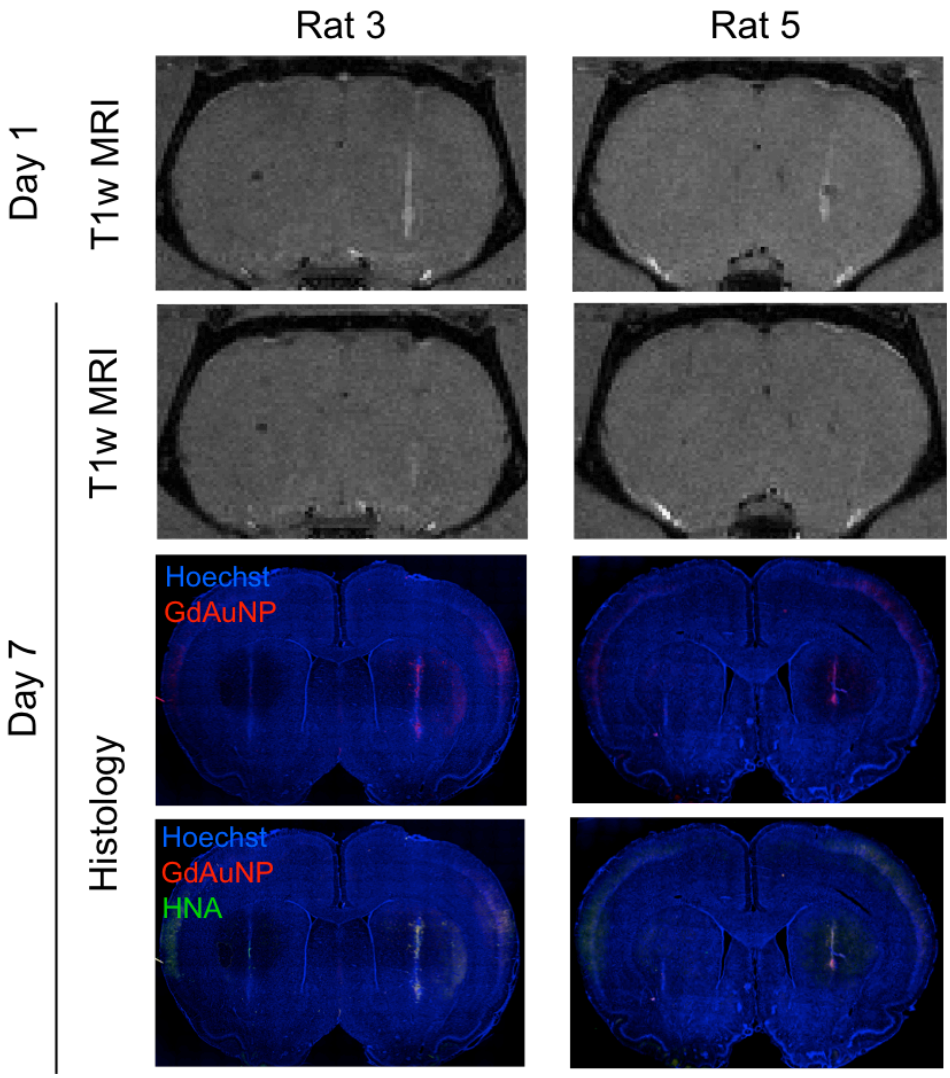

Figure 3.11 Seven days after transplantation, very little contrast is seen on the MR images, corrsponding with a lack of histological staining for transplanted cells (HNA) or GdAuNP.

3.3.9 Effect of cell number and voxel size on cell detection

In order to assess the effect of voxel size and cell number on detection by MRI, one animal received injections containing three different cell numbers, both labeled and unlabeled. The animal was sacrificed and perfused with PFA the following day and the brain was immediately imaged in PBS at 9.4T. Retaining a constant FOV (30x30mm) and slice thickness (0.5mm), the matrix size was varied to acquire T1 maps with voxel volumes ranging from 7 to 195nl. At the smallest voxel volume, the T1 shortening can be clearly seen for all GdAuNP labeled transplants, but this is less clear at 49nl and no longer visible at 195nl (**Figure 3.12**A).

In order to quantify this effect, the T1 of an ROI within the area occupied by labeled cells was compared to an area occupied by unlabeled cells for each map. The resulting contour map shows

that voxel size has a much larger effect on the observed change in T1 than total cell number (**Figure 3.12**B). This is likely due to inhomogeneity of the sample, as the probability of including unlabeled host cells in any given voxel increases with voxel size, thereby effectively reducing the agent concentration. This shows that the frequently used description of a detection threshold as a number of “cells per voxel” can potentially be misleading as this will vary considerably depending on voxel size.

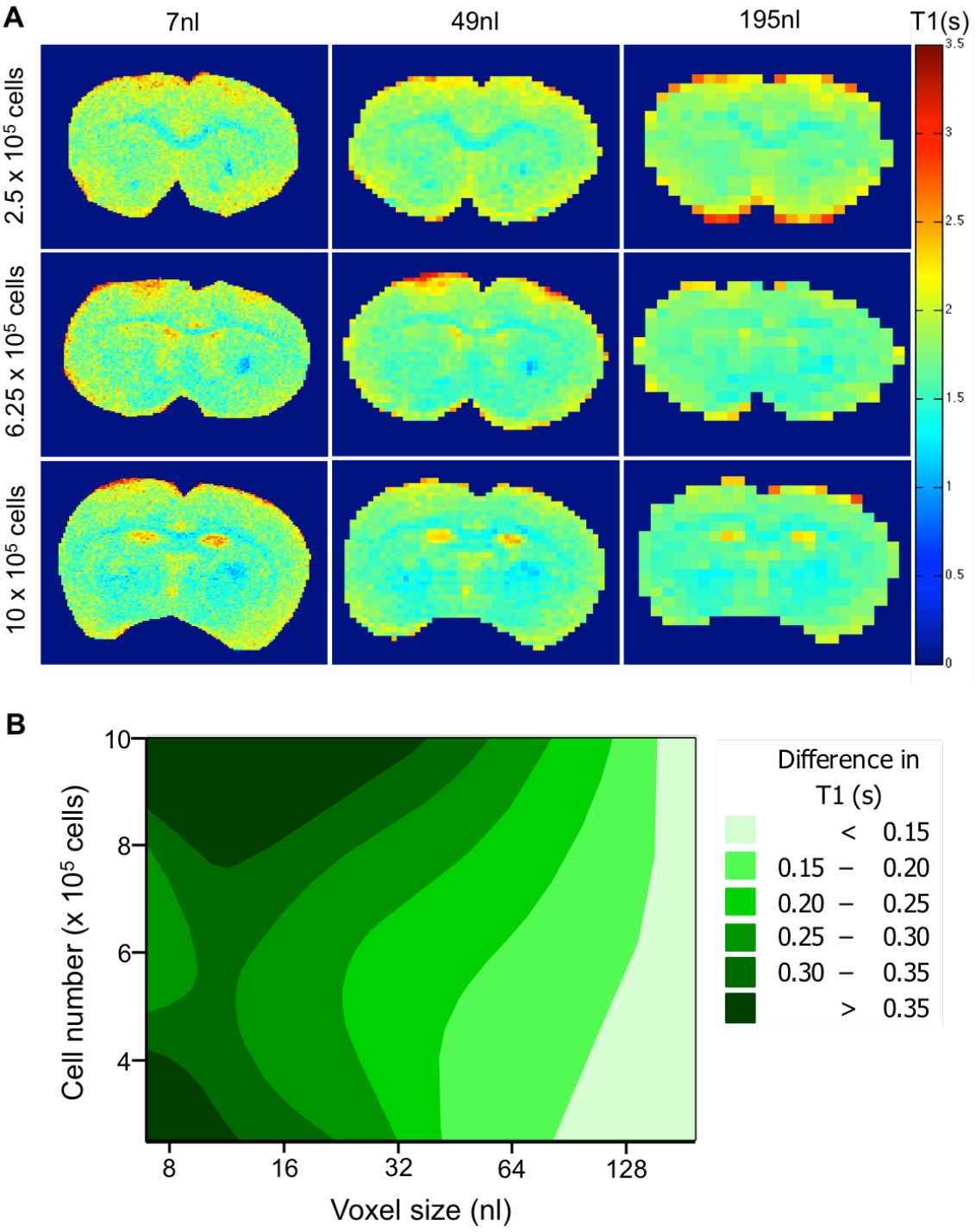

Figure 3.12 T1 maps of 3 different injection sites were acquired at 6 different voxel sizes (A). The change in T1 of labeled compared to unlabeled cells was compared across cell number and voxel volume, with voxel volume having a more marked effect than cell number (B).

3.4 Discussion

In this work we have shown the potential of a novel Gd nanoparticle, GdAuNP, for tracking neural stem cells in vivo. Our work indicates that the particles are easily taken up into cells, show consistent characteristics between batches, and have no significant effects on the biology of human neural stem cells at the concentrations used. Labeled cells can be detected in vivo using T1w images, and contrast is no longer seen after cell death. The effect of voxel size on cell detection was also investigated, and partial volume effects were found to play a significant role. This agent shows promise for cell tracking, but requires further investigation as to its efficacy during long term cell survival.

3.4.1 Challenges in T1 agent detection

A major challenge in cell detection using T1 agents is to achieve an optimal intracellular concentration and distribution of agent for cellular imaging. Since the sensitivity of T1 based MR probes is inherently lower than T2 agents (Helm 2010), a high concentration is required for detection. However, dosing of cells with high concentrations of contrast agents can increase the risk of negative effects on both labeled cells and surrounding tissue (Modo, Beech et al. 2009). In addition, Gd(III) agent stability can be improved by the use of macrocyclic, rather than linear chelates due to improved kinetic stability (Idee, Port et al. 2009), and as such, these are being used increasingly in the design of new particles for cell tracking and may attenuate cellular effects.

As the intracellular concentration increases, the localisation of the agent within the cell becomes increasingly important. Nonspecific endocytosis or pinocytosis is the most commonly used route of agent uptake due to its simplicity and efficiency, but this results in localisation of the agent to endosomes, which has been shown to produce a quenching of the T1 effect above 10^{10} Gd/cell (Terreno, Geninatti Crich et al. 2006). It has further been shown that there is no such quenching of the T2 effect at high agent concentrations, and that the observed T2 relaxivity in lysosome localised agent may instead be increased, potentially due to susceptibility effects (Kok, Hak et al. 2009). The concentration of agent seen in the present study was 10^{8} Gd/cell, below the threshold for quenching and subsequently produced clear signal change on T1w images. However, no signal change was visible on T2w images in vivo, suggesting that the concentration threshold for a T2 effect is higher than that for T1, potentially due to increased “noise” as brain tissue itself has

a lot of T2 contrast. In previous studies using GRID (Gadolinium Rhodamine Dextran), a concentration of 9 x 10^{10} Gd/cell was achieved, and labeled cells were visible on T2w but not T1w images, supporting this hypothesis (Brekke, Morgan et al. 2007, Modo, Beech et al. 2009).

The interplay between an agent's properties, its microenvironment and the imaging parameters used result in a seemingly elusive "sweet spot" for optimum contrast. Molecular parameters interact with magnetic field strength, resulting in a fairly narrow range of optimal water exchange and tumbling frequency for a given field (Caravan, Farrar et al. 2009). However, these molecular parameters are highly sensitive to events such as protein binding and water access, resulting in the differential relaxivity between agents in solution and inside cells as seen here and elsewhere (Kok, Hak et al. 2009). Partial volume effects are much discussed in the context of diffusion weighted MRI (Roine, Jeurissen et al. 2014), but little attention has been given to them in the context of cell tracking. To assess efficacy of potential cell transplant therapies and correlate cell presence and migration with clinically relevant outcomes such as motor coordination, e.g. as assessed by the footfault test (Modo, Stroemer et al. 2000), large animal numbers are required per study. This necessitates shorter imaging times per animal in order to increase throughput, and lower resolution images are significantly faster to acquire and have a better SNR. However we show here that the use of large voxels is likely to result in a significant underestimation of cell number. The selection of voxel size must therefore be based on a balance between acceptable cell detection thresholds, SNR and imaging time constraints. At high field, SNR is not such a significant concern as at lower field, so smaller voxel volumes will give the most accurate cell detection.

3.4.2 Specificity of cell detection

Since there is normally very little contrast in a T1w image of the brain, T1 contrast agents are able to generate a very specific signal that is less likely to be confused with naturally occurring phenomena than a T2 based agent. However the question of agent specificity to the cells remains an issue. Any agent present outside transplanted cells, whether from the injectate solution or after leakage from labeled cells, will be detected as contrast. Bimodal agents allow validation of MRI contrast using histology, as shown here and elsewhere (Detante, Valable et al. 2012), in order to assess the specificity of cell detection. One area of particular concern is the fate of the label after cell death, as lingering label could produce erroneous contrast. The data shown here show an absence of MRI contrast after cell death, consistent with the findings of Guenoun, Ruggiero et al.

(2013), who showed that Gd contrast was quickly reduced below the detection threshold on transplantation of dead labeled cells, compared to SPIO-labeled cells, where contrast persisted for over 2 weeks in the absence of viable cells.

For this reason, it can be expected that Gd(III) based agents should not produce a significant number of false positives, but false negatives may be more of a problem. T1 agents have a generally lower sensitivity, and loss of contrast can be seen as a result of intracellular localisation, or sub-optimal agent concentration or protein interaction. Additionally, data here shows that 29% of transplanted cells did not appear to contain agent. It is therefore important to thoroughly assess all these factors before relying on Gd labeling as a sole indicator of cell location.

3.4.3 Utility of cellular MRI in transplantation studies

Cellular MRI has proven to be an extremely useful source of information in transplantation studies, showing, for example, the time course of cell migration from the contralateral hemisphere to the ischemic area (Hoehn, Kustermann et al. 2002). Many groups saw similar cell behaviour after transplant into stroke models, corroborating its utility (Adamczak and Hoehn 2012). However, much remains to be elucidated regarding the therapeutic mechanism of transplanted cells and their potential for tissue replacement rather than purely neurotrophic effects. In this context, the combination of cell tracking with other MRI techniques to assess angiogenesis and de novo tissue formation may be a powerful combination. In particular, the use of diffusion tensor imaging to show restoration of connectivity across a lesioned area may be highly pertinent.

However, the issue of potential label toxicity remains. New agents are subjected to an increasing battery of in vitro tests, which provide valuable data. But this may not be sufficient to assess the in vivo ramifications of potentially compromised cells, or label effects on local tissue. Indeed, even after proving useful for cell tracking in vivo in the disease model (Modo, Mellodew et al. 2004) and using in vitro testing to select non-toxic labeling conditions (Brekke, Morgan et al. 2007), GRID was still shown to affect the therapeutic efficacy of transplanted cells (Modo, Beech et al. 2009). It is therefore paramount that any investigation into therapeutic efficacy of cell transplant that utilises cell tracking includes an unlabeled cell control for therapeutic outcome measures.

Eventually, utilising cell tracking in clinical trials would provide a wealth of data in terms of the exact location of cell delivery, cell migration, and interaction with the lesion which could be correlated with patient outcome to better inform experimental design for the next phase. However

there are several considerations. Firstly, since the majority of cell tracking applications do not provide additional therapeutic properties, their use must be carefully considered in terms of a risk-benefit analysis to the patients (Modo, Kolosnjaj-Tabi et al. 2013). Secondly, although many agents are approved for clinical use, the dose recommendations are based on dilution in a large volume of blood, and may need to be reconsidered in terms of maximal local concentration. And finally, agent characteristics must be optimised for clinical field strength and imaging parameters, which often differ substantially from those used experimentally.

3.5 Conclusions

GdAuNPs in this system appear to have several advantages for cell tracking in the brain. Specifically, they provide clear contrast on T1w images, while leaving T2w images unchanged to allow anatomical assessment. Additionally, the agent does not continue to show MR contrast after cell death or label host cells, thereby showing a low likelihood of false positive contrast. Although further in vivo testing is required to establish their long term tracking potential, GdAuNPs are a very promising candidate.

Chapter 4: The potential of ParaCEST for tracking multiple cell populations in vivo

4.1 Introduction

Current cell transplantation paradigms in clinical trials are based on the use of a single cell type, with the therapeutic mechanism thought to based more on beneficial effects on host tissue than active integration of the transplant. Improved behavioural outcomes after stroke have been observed after implantation of human neural stem cells even with a very limited amount of neuronal differentiation. However, although these treatments reduce symptoms, they do not result in a full recovery, and large lesions do not completely disappear, although reduction in their size has been observed (Smith, Stroemer et al. 2011). Therefore, a potential avenue of improved treatment would be to place neural stem cells directly into the lesion cavity with structural support in the form of biomaterials. This approach has already been shown to produce a primitive de novo tissue (Park, Teng et al. 2002, Bible, Chau et al. 2009). However, in order for the graft to survive long term, vascularisation is crucial (Bible, Qutachi et al. 2012). In islet grafts, adding endothelial cells to the graft has been shown to improve vascularization and functional outcome (Oh, Oh et al. 2013). There is therefore reason to believe that this approach may also be helpful in the context of tissue engineering in the CNS, such as ischemic stroke and TBI (Zhang, Zhang et al. 2013).

The requirement for multicomponent non-invasive monitoring is one that cannot be met by current techniques. Simultaneous use of T1 and T2 contrast agents has been suggested as a potential mechanism, and shown to be able to detect two cell populations within a biomaterial (Di Corato, Gazeau et al. 2013). However, this method potentially causes confusion with anatomical imaging, and has so far not been demonstrated with cells occupying the same voxel, as the effects of the two agents are likely to interact. Another option would be to use the same contrast agent to label both cell types. However, this would only allow tracking of the graft as a whole, rather than allowing independent imaging of separate populations.

Chemical exchange saturation transfer (CEST) offers several advantages over currently used methodology. Firstly, the contrast can be turned “on” and “off” due to the requirement for a

presaturation radiofrequency (RF) pulse to visualise the CEST target. Secondly, a number of CEST agents can potentially be combined if their chemical shifts are far enough apart, allowing selective visualisation of one target at a time. The basis of CEST is that the protons associated with the molecule of interest are in exchange with the bulk water, and these have distinct chemical shifts (**Figure 4.1**A). When an RF pulse at their specific resonance frequency is applied, only the protons of interest will flip and are then exchanged with the bulk water. This results in a decreased bulk water signal (**Figure 4.1**B). This is normally displayed as a z spectrum. Water is assigned a reference value of 0ppm, and the intensity of the water signal is plotted at each chemical shift after normalisation to a reference frequency without CEST effects (e.g. -300ppm). Thus any reduction in the bulk water signal caused by CEST results in a dip (**Figure 4.1**C, black line). Subtracting the intensity values at opposite sides of the water peak (e.g. Intensity at -18ppm – Intensity at +18ppm) gives an asymmetry value, which is the most common way of expressing CEST contrast (**Figure 4.1**C, grey line).

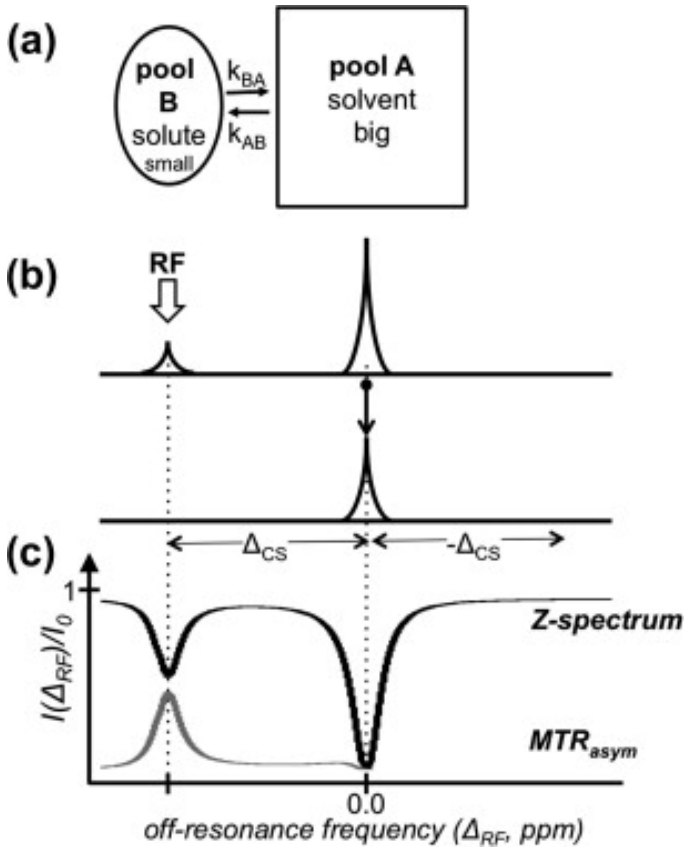

Figure 4.1 Schematic of CEST experiment. (a) Pool A (solvent) is in exchange with pool B (solute). (b) Pools A and B have distinct chemical shifts, with the difference of ΔCS. RF is applied on-resonance with pool B resulting in saturation transfer and signal decrease of pool A. (c) z-spectrum: normalized water intensity (I/I_0) vs. off-resonance frequency of the saturating RF (ΔRF). Water resonance is

assigned 0ppm value. MTRasym: z-spectrum asymmetry vs. RF off-resonance value. Vinogradov, Sherry et al. (2013)

CEST is so far most commonly used to detect endogenous molecules, such as glucose (Zu, Spear et al. 2014) or glycosaminoglycans (Saar, Zhang et al. 2012), which have relatively small chemical shifts, normally in the region of 1-5ppm. Paramagnetic CEST (paraCEST) refers to the use of paramagnetic compounds as the solute providing the chemical exchange with bulk water (Woods, Woessner et al. 2006). This allows a larger chemical shift than is found in endogenous molecules, allowing reduced noise. Lanthanide complexes are the most commonly used and have been used for applications such as pH and temperature mapping (McVicar, Li et al. 2013). Their potential for cell tracking was first investigated in vitro using Eu(dotamGly) and Tb(dotamGly), but was hampered by low biocompatibility and high power requirements (Aime, Carrera et al. 2005). Modified agents were then generated utilising the biocompatible HPDO3A chelate used in the clinical Gd agent ProHance. It was shown that these could be used to visualise two cell populations in vivo using MR spectrometry (Ferrauto, Castelli et al. 2012).

ParaCEST therefore provides the potential to label two cell populations and detect each one selectively and independently, whilst preserving anatomical imaging. Here we aim to test this potential in the context of tissue engineering for stroke. STROC05 human fetal neural stem cells (NSCs) have been shown to differentiate into the different neural and glial cells of the CNS (El Akabawy, Martinez-Medina et al. 2011), and to form a primitive neural tissue inside the lesion cavity (Bible, Dell'acqua et al. 2012). By implanting these cells with human cerebral microvascular endothelial cells, it may be possible to vascularise the graft and allow long-term survival. Here we assess uptake of two paraCEST agents, Eu-HPDO3A and Yb-HPDO3A, into the two cell types in order to assess whether the two agents can be selectively detected in vitro and in vivo after implantation into a stroke cavity.

4.2 Methods

4.2.1 Agent Synthesis

Agent Synthesis was performed by Giuseppe Ferrauto at University of Turin, Italy

HPDO3A ligand was kindly provided by Bracco Imaging S.p.A. (Colleretto Giacosa (TO), Italy). Yb_2O_3 and Eu_2O_3 were purchased from Sigma-Aldrich. The synthesis of Yb(III)- and Eu(III)-complexes was carried out mixing the lanthanide oxide Ln_2O_3 and the ligand HPDO3A (1:2 molar ratio) in water. The mixture has been let to react for 2 weeks under stirring and heating at 80°C. The purity of the compounds was around 90% as evaluated by measuring the bulk magnetic susceptibility (BMS) shifts of ^1H NMR resonance signals of solution (tert-butanol in water) containing the compound with the respect to the same solution without paramagnetic compound (Evans' Method) (Corsi, Platas-Iglesias et al. 2001).

4.2.2 Inductively Coupled Plasma Mass Spectrometry (ICP-MS)

ICP-MS was performed by Giuseppe Ferrauto at University of Turin, Italy

The Lanthanide content of cells was determined using inductively coupled plasma mass spectrometry (ICP-MS). Cells were collected in 0.1ml of PBS and destroyed by sonication. Then they were digested with concentrated HNO_3 (70%) under microwave heating (Milestone MicroSYNTH Microwave labstation equipped with an optical fibre temperature control and HPR-1000/6M six position high-pressure reactor, Bergamo, Italy). After the mineralization, each sample was taken with 2 mL of ultrapure water and analysed by ICP-MS by using a Thermo Scientific ELEMENT 2 ICP-MS -Finnigan, Rodano (MI). Three replicates of each sample solution were analysed. The concentration of protein was determined by the Bradford method using bovine serum albumin as standard.

4.2.3 Cell labeling

To assess the effect of different labeling methods and parameters on cell uptake and survival, labeled cells were labeled by electroporation or pinocytosis and assessed for agent presence, and for cell survival overnight.

4.2.3.1 Optimisation of Electroporation

The Eppendorf Multiporator was used for all electroporation experiments, and a theoretical set of conditions was calculated from the Eppendorf user guide, based on cell size (530V, 100µs, $3x10^6$ cells/ml) (Eppendorf 2006). Agents were dissolved in Hypoosmolar or Isoosmolar electroporation buffer (90mOsm and 280mOsm respectively, Eppendorf). In order to estimate the best parameters to test for each cell type, Since the paraCEST agents are not fluorescent, a proxy agent, Carboxyfluorescein (Sigma), was used to define ranges of conditions to test, since uptake could be assessed quickly within the lab, whereas samples containing paraCEST agents had to be sent to Turin for analysis. Using carboxyfluorescein, the effect of varying electroporation parameters on agent uptake and cell survival was assessed in each cell type. Voltages, pulse lengths, cell densities, agent concentration and buffer osmolarity were varied around the initial estimates to cover a broad range and identify ranges showing potential for maximising agent uptake, whilst minimising effects on cell survival. Concentrations of carboxyfluorescein were selected based on Di Gregorio, Ferrauto et al. (2013) and the agent's solubility in electroporation buffer, as the maximum concentration achievable was 5mM. The exact parameters used are shown in

. The controls for cell survival and to correct for background auto-fluorescence were cells that had not undergone electroporation.

Table 4.1 Electroporation conditions for carboxyfluorescein condition testing

Figure	Voltage (V)	Pulse length (µs)	Cell density (x 10^6 cells/ml)	Agent (mM)
A	100	100	3	1
	530			
	1000			
B	530	15	3	1
		100		
		300		
C	530	100	2	1
			3	
			4	
D	530	100	3	0.5
				1
				5

After electroporation, cells were plated onto coverslips and incubated overnight before fixing with PFA as in section 2.2.2.4 and mounting in Vectashield + DAPI. Fluorescence images were then taken as previously described (section 2.2.7) using consistent imaging parameters and obtaining all images in the same session in a randomised fashion to minimise variation. The number of DAPI cells was then counted as in section 2.2.4.2 to give a measure of cell survival, and the relative intensity in the green channel was measured using MATLAB (See Appendix 1). The intensity of each image was then divided by the number of cells to give Relative Fluorescence Units (RFU) per cell, which was used as an estimation of agent uptake. The results of this experiment are shown in **Figure 4.2**, and were used to inform the selection of parameters to test with the paraCEST agents.

Decreasing the voltage did not significantly affect cell survival for either cell type, but agent uptake was increased in both. Increasing the voltage had a dramatic effect on agent uptake for NSCs, but not ECs (**Figure 4.2**A). Increased voltage was therefore selected as a parameter to take forward for assessment for NSCs with paraCEST agent. However, since cell survival was also affected, the range was restricted to 530-750V to avoid the most extreme effects.

Decreasing the pulse length improved cell survival for NSCs, but uptake was also affected. Increasing pulse length severely affected NSC survival with only a moderate increase in uptake. However, for ECs there was an increase in uptake without a significant effect on survival (**Figure 4.2**B). Increased pulse length was therefore selected as a parameter to test for ECs with the paraCEST agent. Since survival was not significantly affected, the range of pulse lengths tested was extended to 100-500μs in order to maximise uptake effects.

Cell density did not appear to be a major factor with carboxyfluorescein, although lower cell density slightly decreased cell survival for both cell types (**Figure 4.2**C). However, a pilot imaging experiment with NSCs labeled with Eu (200mM, 530V, 100μs) showed similar CEST contrast and survival when electroporated at 3 or 9 x 10^6 cells/ml (**Figure 4.2**F). Cell densities of 3, 6 and 9 x 10^6 cells/ml were therefore also taken forward for further testing.

Increasing agent concentration increased agent uptake for both cell types, and affected cell survival (**Figure 4.2**D). However, direct parallels cannot be drawn with the paraCEST agents since the concentration range is so different. Ferrauto, Castelli et al. (2012) previously used 100mM of each agent for labeling via pinocytosis. For this reason, the paraCEST agents also

have large effects on the osmolarity of the electroporation solution, which has additional effects on cell survival and uptake (**Figure 4.2**E). Therefore the agent concentration was maximised within the limitation of maintaining isoosmolar conditions and kept constant at 200mM to give a final osmolarity in hypoosmolar buffer of 290mOsm, which approximates isoosmolar conditions for the cells.

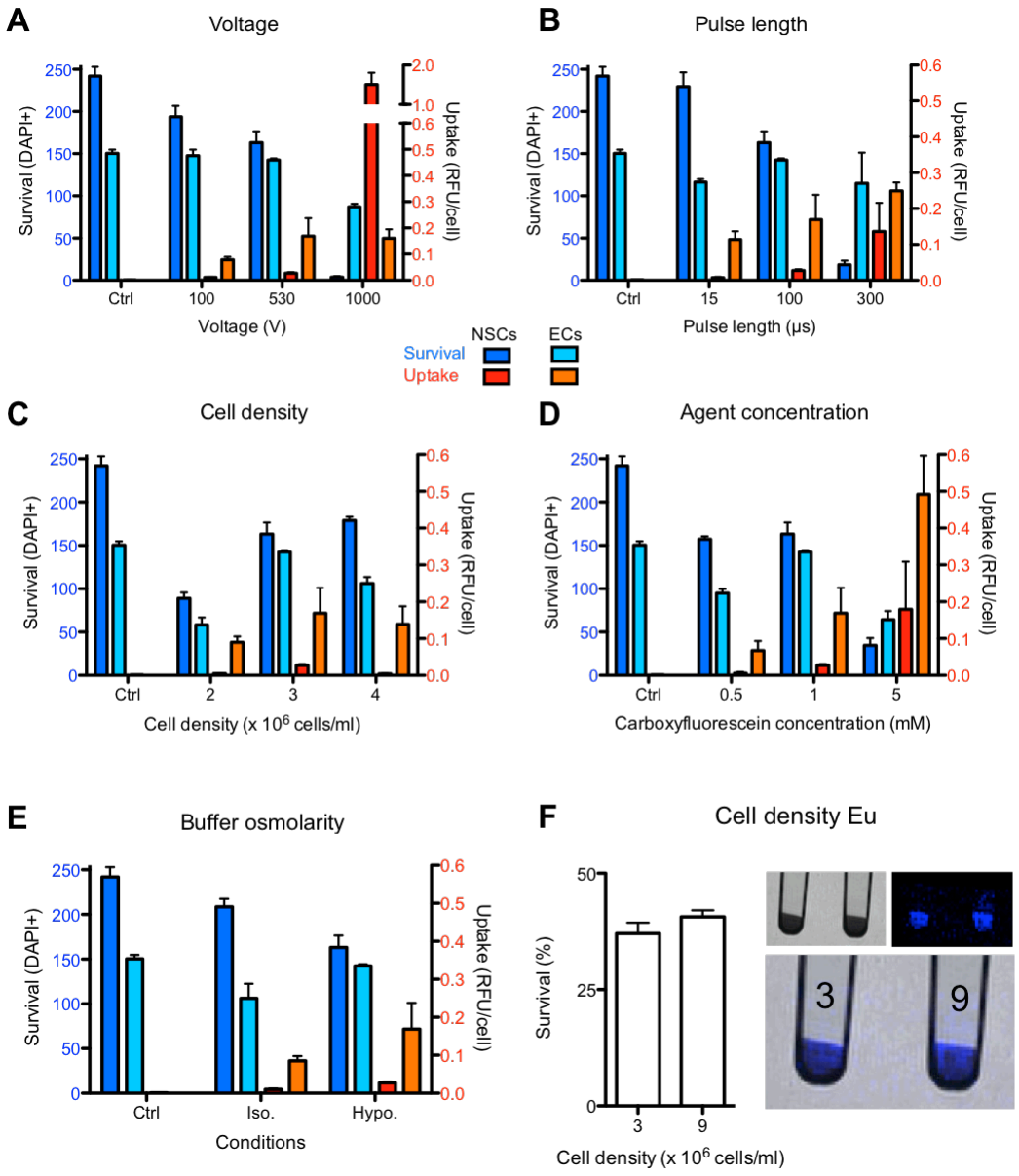

Figure 4.2 Preliminary assessment of electroporation parameters. Varying the voltage of the electroporation pulse (A) showed little effect of agent uptake in ECs (D3 cells, orange bars), but a dramatic increase in uptake for NSCs (STROC05, red bars), but also a decrease in survival. Increasing the length of the pulse (B) showed an increase in agent uptake into ECs, with no significant effect on cell survival, but for NSCs showed a small increase in agent uptake with a large drop in cell survival. Increasing the cell density during electroporation (C) appeared to have little effect on agent uptake, but increased cell

survival for both cell types. Increasing agent concentration (D) showed an increase in agent uptake for both cell types, but also a decrease in cell survival.

The conditions therefore taken forward to test with paraCEST agents were:

- Constant agent concentration of 200mM
- Cell densities of 3, 6 and 9 x 10^6 cells/ml for both cell types
- Voltages of 530, 650 and 750V for NSCs. Constant at 530V for ECs
- Pulse lengths of 100, 300 and 500µs for ECs. Constant at 100µs for NSCs.

4.2.3.2 Pinocytosis

To allow agent uptake via pinocytosis, the agent was dissolved in the cells' normal growth medium at the required concentration (50, 100 or 200mM) and pre-warmed to 37°C. A well of cells at around 60% confluence for NSCs or 80% confluence for ECs cells was selected, and the media aspirated and replaced with growth media containing dissolved agent. They were then incubated at 37°C, 5% CO_2 for the required incubation time of 12, 24 or 48 hours. N=3 per condition.

Assessment of cell survival, and sample collection for ICP-MS: For electroporation, cells were electroporated with agent and then placed into a 48 well plate at 150,000 cells/well and incubated overnight. For pinocytosis, cells were plated into 48 well plates at 150,000cells/well and allowed to attach overnight. The medium was then changed to include ParaCEST agent, and cells were incubated for the appropriate time. Unlabeled cells were grown alongside to control for the effect of time on cell number.

Monolayers were then rinsed three times with HBSS before being harvested with Accutase. A cell count was obtained using a haemocytometer (average of 3 counts) and a known volume of suspension was then analysed by ICP-MS. In order to calculate intracellular concentration, the total lanthanide content in moles was divided by the number of cells present in the suspension to provide moles/cell. This was then divided by the average volume of a cell (3.91pl) to provide the Molar concentration.

The results of this experiment are shown in **Figure 4.7**, and final conditions were then selected to take forward.

4.2.4 Cell preparation for imaging

Cells were harvested, resuspended in PBS and counted. They were then resuspended at 3 x 10^6 cells/ml in hypoosmolar electroporation buffer (Eppendorf) containing agent dissolved at 200mM. 400µl of suspension was then transferred to a 2mm electroporation cuvette, and 1 pulse was applied at 530V for 100µs. The mixture was then left in the cuvette for 15min at room temperature to allow diffusion of agent. The mixture was then carefully transferred to a coated flask containing pre-warmed proliferation medium with a dilution ratio of at least 1:10. Cells were incubated overnight before washing three times with HBSS and harvesting for in vitro imaging or cell transplantation.

Cells were prepared for phantoms as in section 3.2.7.1. Due to the CEST effects of gelatin, all MR imaging was performed on cell pellets in PBS. Where dilution of labeled cells was required to produce a particular ratio of labeled cells, unlabeled cells were used to occupy the required volume, rather than suspending in gel. Since the agent detection characteristics are affected by their incorporation into cells, cell viability during imaging acquisition is important. Therefore, the available scanning time for samples was determined by measuring cell viability by trypan blue exclusion after different scanning times, compared to pre-scan viability and an un-scanned control left at room temperature (**Figure 4.3**). There was no significant difference compared to pre-scan viability at 1.5, 3 or 5 hours, but after 7 hours viability was significantly reduced (61%, $p<0.0001$ by 2 way ANOVA). Scanning time for in vitro samples was therefore restricted to 5 hours or less.

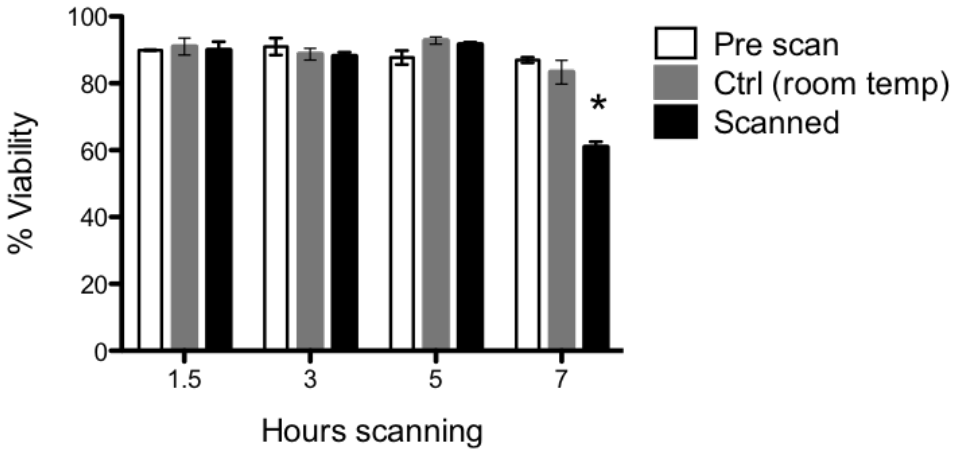

Figure 4.3 Cell viability during ParaCEST MRI. Cell viability remained consistent over 5 hours scanning time but was reduced at 7 hours.

4.2.5 MR Imaging

MRI sequences were designed and implemented by Wen Ling at University of Pittsburgh.

MR Images were acquired on a 9.4T horizontal bore Varian magnet equipped with Agilent VnmrJ 3.1 console. A volumetric birdcage quadrature coil was designed by Mike Modo and Wen Ling, and built by Virtumed LLC. It has a diameter of 30mm and effective length in the z direction of 25mm and can handle Radiofrequency (RF) power of up to 55μT/ 5sec input on a 250~300g rat.

The implementation of paraCEST imaging applications poses a number of challenges in terms of MRI:

B0 homogeneity: The fidelity of CEST contrast is very much dependent on B0 homogeneity, which refers to the field generated by the main magnet. Modern animal MRI scanners may have inherent variability ΔB0 ~100Hz (0.2ppm at 9.4T). This variation, plus tissue inhomogeneity, may cause CEST contrast error ~±0.5% for Eu agent. Given that the CEST contrast observed between labeled and unlabeled cells is ~1.0-1.5%, an error of 0.5% cannot be tolerated. To address this issue, an accurate Water Saturation Shift Referencing (WASSR) B0 field map was generated for each CEST scan. A typical rapid acquisition relaxation enhancement (RARE) spin–echo sequence was used (RARE factor of 32), with an echo time (TE) of 3.8 ms, and a relaxation time (TR) of 3s. The presaturation pulse is 1ms at 0.1μT, and the offset region is set between ±0.3ppm with 0.04ppm per step. The resultant data allowed generation of a z-spectrum for each voxel using spline-fitting. In order to obtain accurate water frequency for each voxel, a maximum symmetry algorithm was applied (Stancanello, Terreno et al. 2008). The resulting map was incorporated into the z-spectra calculation for CEST contrast on voxel-by-voxel basis.

B1 homogeneity: A high quality CEST image also requires high B1 homogeneity. This was addressed in the coil design, by using volumetric birdcage quadrature coil with two RF channels, 0º and 90º RF input phase simultaneously. This resulted in low B1 variation across the rat brain.

High Power requirement: Both paraCEST agents require RF input power >20μT (for Yb, ~56μT) with a pulse duration of 800ms-1200ms (100% duty cycle within this period). This is beyond the capacity of the average coil, but was addressed here by using high quality, high power capacitors in the building of the coil. The high power also has the potential to damage the magnet itself. The Varian system used here has a maximum input of 1kW, and all safety features to protect the

hardware have been removed. In order to avoid a high level of reflected power that could damage the hardware, but still fully utilise the input power, decoupling between the two RF channels in the quadrature coil was ~-40dB to allow effective coil loading for a 300g rat. Optimal tuning and matching after loading the sample is also of the utmost importance here. Even after taking the above measures, the high power increased the specific absorption rate (SAR), thereby generating heat in the sample. The SAR generated by a given sequence is proportional to B_1^2. A T2 weighted image can be generated by a RARE sequence where RF power ~10μT, 5% duty cycle (the percentage of the TR that the RF pulse is on), with a TR of 3s. To generate CEST contrast, an additional 1000ms pulse of 56μT was appended at the beginning of the sequence. This results in an RF power of 56μT with a 38% duty cycle. The SAR would therefore be 238 times [$(56/10)^2$ X (38/5) = 238] higher with the CEST pulse than the standard RARE protocol. This was a significant concern regarding animal safety. However, the use of a long TR, particularly for Yb (10s), allowed time for excess energy to dissipate between each excitation, so that the final protocol did not induce any excessive increase in animal temperature. This was measured at 37°C ± 1°C as measured by rectal probe (**Figure 4.4**), which is in line with FDA guidelines of maximum 1°C whole body heating due to SAR effects (Zaremba 2002). However, this resulted in a lengthy acquisition time.

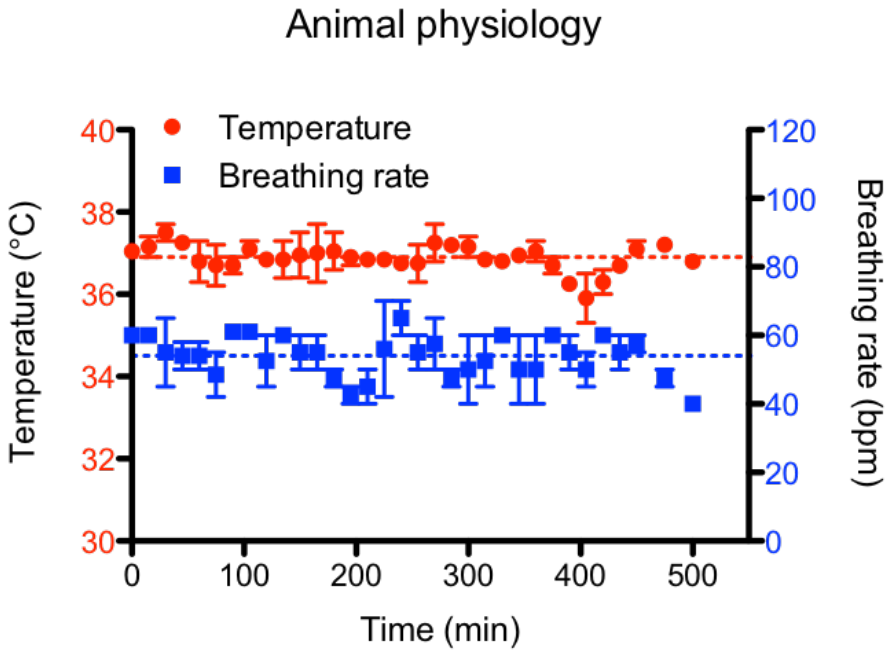

Figure 4.4 Animal temperature and breathing rate throughout paraCEST MRI.

Final MR Imaging Protocol:

T_2w images were acquired as in section 3.2.7

For acquisition of z spectra, a frequency offset range of ±110ppm was investigated, with an additional reference offset at ±300ppm. A typical RARE spin–echo sequence was used (RARE factor of 8 or 16 depending on the T_2 of the sample), with an echo time (TE) of 4.2 or 8.4ms, and a relaxation time (TR) of 3s for Eu and 8s for Yb. An isotropic 64×64 acquisition matrix with a FOV of 30x30mm and a slice thickness of 1mm were used. The whole sequence was preceded by a saturation scheme consisting of a continuous rectangular wave pulse. For EuHPDO3A, the presaturation pulse was 800ms long, with a RF B_1 intensity of 23μT. For YbHPDO3A, the presaturation pulse was 600ms, with a RF B_1 intensity of 56μT.

For in vivo experiments, the scanning time had to be kept within reasonable limits, so full z spectra were not acquired. Instead, a number of points were acquired around the specific chemical shift of the agent, along with reference points of 0 and -300ppm. For Eu, the offsets chosen were ±13.5ppm, ±16ppm, ±17ppm, ±18ppm, ±19ppm and ±20ppm. Yb has two exchange sites, one at 69ppm, and one at 97ppm. When targeting 69ppm, offsets selected were ±60ppm, ±67ppm, ±68ppm, ±69ppm, ±70ppm and ±71ppm. When targeting 97ppm, offsets were ±90ppm, ±95ppm, ±96ppm, ±97ppm, ±98ppm and ±100ppm.

The z-spectra were interpolated by smoothing splines to identify the zero-offset on a voxel-by-voxel basis of the bulk water and, then, to assess the correct ST% value over the entire range of frequency offsets investigated. Custom-made software, compiled in the MATLAB platform (MathWorks), was used (Raya, Dietrich et al. 2010). The extent of CEST effect is calculated as follows:

$$ST\% = (1 - (M_S/M_0)) \times 100$$

where M_s is the intensity of the bulk water NMR signal after the irradiation on resonance (Δω) of the mobile proton pool and M_0 is the intensity of the bulk water NMR signal after the irradiation at −Δω.

4.2.6 Magnetisation transfer (MT) simulation

In the current in vivo application of paraCEST, due to its extremely lengthy acquisition, it is not possible to experimentally obtain full z-spectra. However, the exchange between free bulk water pool and proton pool associated with Eu/Yb can be readily described by the Bloch-McConnell equation. Chemical/physical properties of both agents, and the tissue properties of the rat brain are either published or were obtained from in vitro experiments at the beginning of the project. As a result, numerically solving this equation to obtain full z-spectra will help us address some of the potential problems.

In MR theory, a homogenously mixed proton population with the same MR properties (T1,T2, exchange rate with other proton population, temperature, etc.) can be categorised as one pool. In our system, Eu associated protons and Yb associated protons are the two pools of interest. When in solution, the CEST effect is described purely by the exchange of these pools with the bulk free water. However, in the presence of cells or tissue, there is an additional pool of protons, which are those bound to biological molecules, such as those within cell membranes and extracellular matrix. The properties of this pool are quite different from the those of the free water pool. It has a very short T2 (~9.2μs in the rat brain, compared to ~40ms for bulk water), but it exchanges with free water pool. The additive result is that the tissue itself will respond to the CEST technique even in the absence of paraCEST agents. This is known as the magnetisation transfer (MT) effect, and can also be calculated using the Bloch-McConnell equation.

The Bloch-McConnell equation takes the form:

$$\frac{d}{dt}\begin{bmatrix} M_a \\ M_b \\ M_c \\ M_d \end{bmatrix} = \begin{bmatrix} \boldsymbol{L_a - K_{ab} - K_{ac} - K_{ad}} & \boldsymbol{K_{ba}} & \boldsymbol{K_{ca}} & \boldsymbol{K_{da}} \\ \boldsymbol{K_{ab}} & \boldsymbol{L_b - K_{ba}} & \mathbf{0} & \mathbf{0} \\ \boldsymbol{K_{ac}} & \mathbf{0} & \boldsymbol{L_c - K_{ca}} & \mathbf{0} \\ \boldsymbol{K_{ad}} & \mathbf{0} & \mathbf{0} & \boldsymbol{L_d - K_{da}} \end{bmatrix} \times \begin{bmatrix} M_a \\ M_b \\ M_c \\ M_d \end{bmatrix} + \begin{bmatrix} \frac{M_{0a}}{T_{1a}} \\ \frac{M_{0b}}{T_{1b}} \\ \frac{M_{0c}}{T_{1c}} \\ \frac{M_{0d}}{T_{1d}} \end{bmatrix}$$

Where $\mathbf{L_i}$, $\mathbf{K_{ij}}$, **0** are 3x3 matrices representing the physical properties of the corresponding pool; [Ma, Mb, Mc, Md]' are the answers are we are looking for; [M0a, M0b, M0c, M0d]' are the initial state of [Ma, Mb, Mc, Md]' before CEST begins. $\mathbf{L_a}$, $\mathbf{L_b}$, $\mathbf{L_c}$ and $\mathbf{L_d}$ are the free water pool, Eu proton pool, Yb proton pool, and biomolecule-bound water proton pool respectively. $\mathbf{K_{ab}}$, $\mathbf{K_{ac}}$, and $\mathbf{K_{ad}}$ are the exchange rates from free water to Eu proton pool, Yb proton pool, and biomolecule-

bound water proton pool respectively, and $\mathbf{K_{ba}}$, $\mathbf{K_{ca}}$, and $\mathbf{K_{da}}$ are the backward exchange rate from the same pools to the free water pool. The exchange directly between the Eu proton pool, Yb proton pool, and biomolecule-bound water proton pool are effectively **0**.

Although the details of solving the equation is beyond the scope of thesis, please note that all the important physical properties are reported ($\mathbf{L_a}$, $\mathbf{L_d}$, $\mathbf{K_{ad}}$/ $\mathbf{K_{da}}$ (Stanisz, Odrobina et al. 2005)), or measured in our lab using methods previously described ($\mathbf{K_{ab}}$/$\mathbf{K_{ba}}$, $\mathbf{K_{ac}}$/$\mathbf{K_{ca}}$ (Dixon, Ren et al. 2010)), or have little influence on the outcomes of interest and are assumed with reasonable values ($\mathbf{L_b}$, $\mathbf{L_c}$ (Li, Hudson et al. 2008)). All the RF conditions are set as used for experiments. All input values used are given in Appendix 2. The Bloch-McConnell equations are solved between ±120ppm on 1ppm basis, ±300ppm are solved as a reference for z-spectrum normalization. The Mza was collected to form z-spectra as shown in Figure 4.9. All the input parameters and detailed form of **L**, **K**, **0**, **M** are listed in Appendix 2.

4.2.7 Middle Cerebral Artery Occlusion (MCAO) Surgery

Animals used were male Sprague-Dawley rats, kept on a 12 hour light/dark cycle, and given food and water ad libitum. Animals arrived at 180-200g and were allowed one week to acclimatize before undergoing MCAo surgery at 240-260g.

An adaptation of the protocol used by Longa et. al. (1989) and Modo et. al. (2000) was used. Animals were anesthetized using Isoflurane (4% for induction, 2% for maintenance), and a rostro-caudal incision was made above the trachea. The right common carotid artery was then exposed, and the internal carotid was cleaned until the bifurcation with the pterygopalatine artery was visible. The right common carotid was permanently ligated with a suture, and a coated filament (Doccol) was inserted through a small incision in the carotid trunk into the internal carotid artery and advanced up past the pterygopalatine to the bifurcation with the middle cerebral artery. The correct positioning of the filament was judged by distance (~18-20mm) and the feel of resistance, at which point it was secured in place and the animal was allowed to recover. After the occlusion time of 70min, the animal was re-anesthetized as before and the filament retracted as far as the carotid bifurcation, where the tip permanently remained and excess was trimmed off. The wound was then sutured and the animal was given IP Buprenex (0.05mg/kg) and topical analgesic cream (2.5% Lidocaine, 2.5% Prilocaine, Sandoz) for analgesia, as well as 5ml Plasmalyte IP to help with rehydration. Animals were then weighed daily and their wellbeing monitored using basic

neurological and distress scales until they regained their pre-op weight (Modo, Stroemer et al. 2000). Buprenex (0.05mg/kg) was administered every 12 hours for 72 hours following the procedure and then as necessary, and both wet and dry food was provided, and intake monitored.

4.2.8 Stereotactic Injection

The MCAO model produces animals with very varied lesions (Smith, Stroemer et al. 2011). In order to fill the lesion with cells as an approach to tissue engineering, it is necessary to know the volume of the lesion (Bible, Chau et al. 2009), and also to remove the extracellular fluid currently occupying it so as to achieve homogenous distribution of injected material throughout the cavity and avoid unnecessary increases in intracranial pressure during surgery (Massensini, Medberry et al. 2014).

4.2.8.1 Derivation of injection coordinates using MRI

T2w images (0.156x0.156x0.5mm voxel size) were examined in Jim 6.0 (Xinapse), and a region of interest (ROI) was drawn in a damaged slice on the contralateral hemisphere, including striatum, cortex and corpus callosum, but avoiding ventricles. The Image was then masked at the average intensity of this ROI + 1 standard deviation (Stille, Smith et al. 2013). This allowed clear delineation of the hyperintense lesion area. ROIs were then drawn around these hyperintense areas, and the lesion volume was calculated .

The drainage site was selected as the most dorsal point of the lesion, and the injection point as the most ventral (**Figure 4.5**A), and distance between them (AP/L) was required to be at least 1.5mm to allow for two burr holes in the skull. The MR images were compared with the Allen brain atlas to identify Bregma, and the anterior/posterior coordinates of each site were deduced based on the number of 0.5mm slices from Bregma to the target slice. Lateral and ventral distances were measured in Jim from the midline and dura respectively (Massensini, Medberry et al. 2014).

4.2.8.2 Injection/drainage procedure

2-4 weeks after MCAO, animals were anesthetized with Isoflurane (4% for induction, 2% for maintenance) and placed in a stereotactic frame (Kopf). A rostro-caudal incision was made to expose the skull, and two burr holes were made at the coordinates derived from the animal's MR images (**Figure 4.5**B). A sterile disposable 23G needle was inserted slowly by hand into the drainage site, and the Hamilton needle containing the injectate was inserted into the injection site.

The material was then injected using a micro pump (Micro4, WPI) at 5µl/min to a total volume equal to the calculated volume of the lesion. Extracellular fluid was observed emerging from the drainage needle (**Figure 4.5**C).

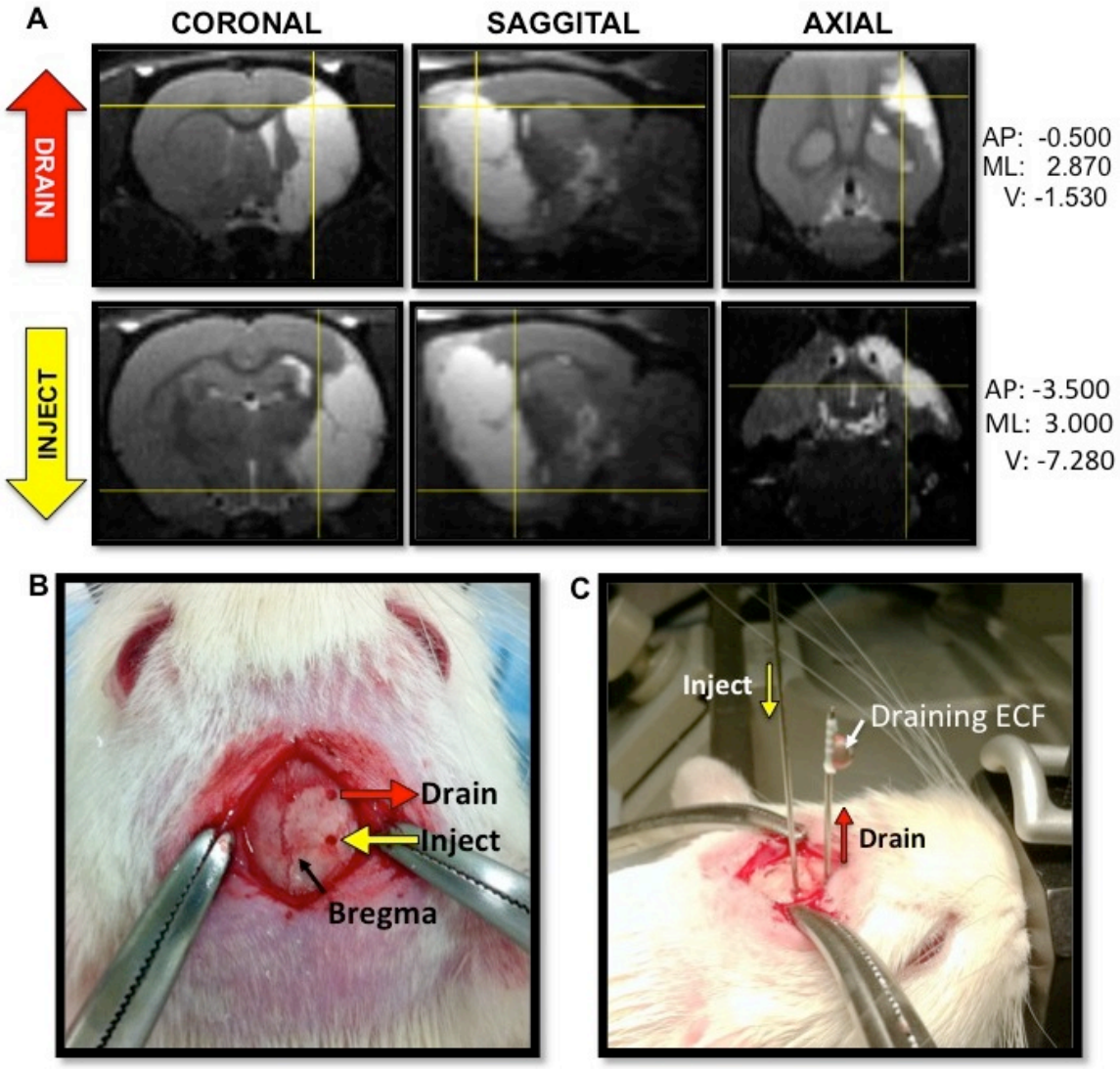

Figure 4.5 Injection/Drainage. Injection and drainage sites are chosen according to the topology of the lesion (A). Two burr holes are drilled in the skull (B) and ECF can be observed draining from the needle during injection (C). Figure and optimization of technique by Andre Massensini

4.3 Results

4.3.1 Agent characteristics

In order to verify that the two paraCEST agents, Eu-HPDO3A and Yb-HPDO3A (hereafter Eu and Yb) could be reliably and separately detected by MRI, solution phantoms were imaged. Complete z spectra were acquired for each agent (10mM) from -120 to 120ppm at 0.5ppm intervals to ascertain the range of offsets required for detection of each agent. Eu has a single exchange site corresponding to a peak at 18ppm, whereas Yb has two exchange sites, corresponding to peaks at 69 and 97ppm (**Figure 4.6**A).

Images were then acquired with presaturation pulses at the required ppm (16-20 for Eu and 66-71 and 96-101 for Yb, with 1ppm steps; Reference at 0 and -300ppm) of solutions at different concentrations of Eu and Yb agents in PBS, separately and combined. The relationship between concentration and asymmetry is linear for both agents, with Yb requiring a higher concentration for the same magnitude of contrast. This does not appear to be altered by mixing the agents in the same solution (**Figure 4.6**B). There is some background evident in the 5mM Yb solution at 18ppm, which is likely due to the presence of unspecific exchange sites on the HPDO3A chelate. However, the signal from the Eu solution is much stronger, showing that chelate exchange sites should not have a significant effect in comparison to the specific signal.

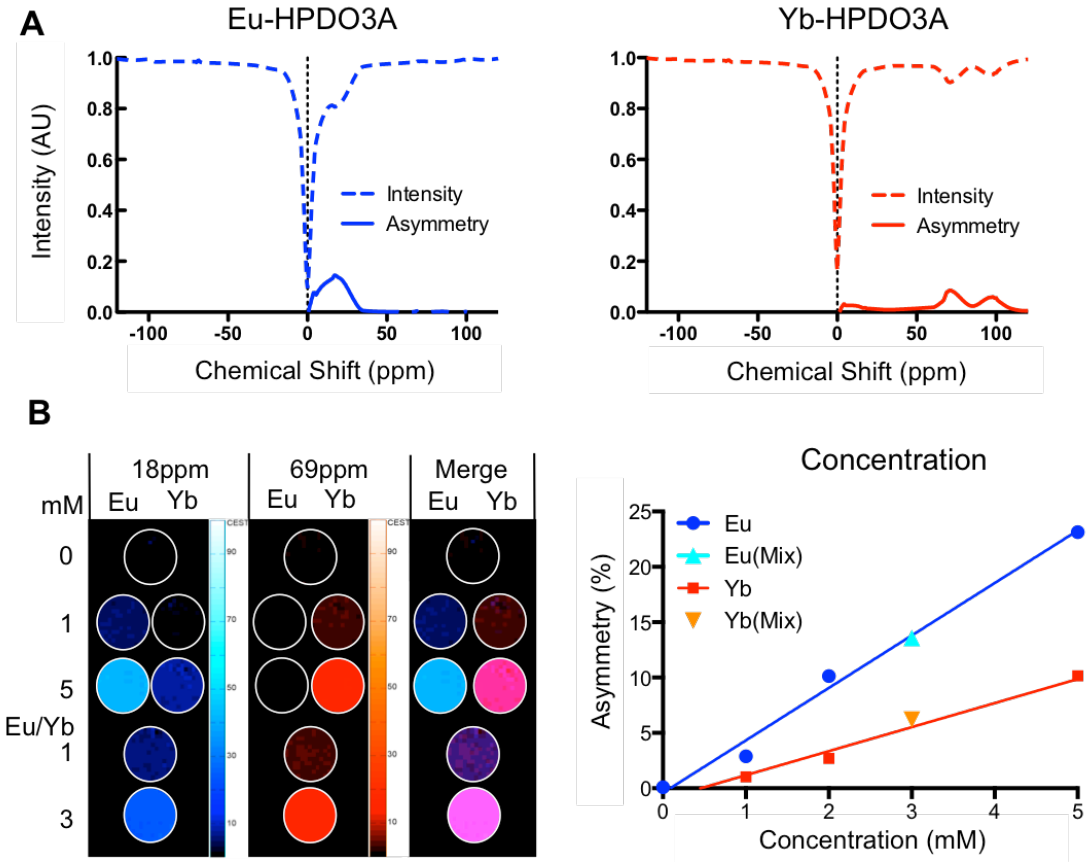

Figure 4.6 Agent characteristics in solution. Z spectra of agent solutions showing signal intensity compared to the reference at -120ppm, and asymmetry, which is the subtraction of the intensity at each chemical shift from it's corresponding negative (A). MR images of solutions at different concentrations at the relevant chemical shifts show a linear relationship between concentration and asymmetry (B)

4.3.2 Cell uptake

The concentration of paraCEST agent required for detection is very high. Gadolinium can be detected in the μM range (see Chapter 3), whereas mM concentrations are required for paraCEST detection. Therefore, optimising agent uptake with respect to intracellular concentration and cell survival is of the utmost importance. Pinocytosis and electroporation have both been used to label cells with Gd-HPDO3A, where the most effective method appeared to be largely cell type dependent (Di Gregorio, Ferrauto et al. 2013). Neural stem cells (NSCs) and endothelial cells (ECs) were each labeled with one paraCEST agent under a variety of pinocytosis and electroporation conditions. Since NSCs are generally more susceptible to toxicity than ECs, and Eu appears to provide better contrast at lower concentrations, Eu was selected for uptake into NSCs, and Yb into ECs. Labeled cells were then harvested and analysed for lanthanide

content by inductively coupled plasma mass spectrometry (ICP-MS). The number of cells harvested was used as a measure of survival.

For pinocytosis, agents were dissolved in the cells' normal growth medium at 50, 100 or 200mM and incubated for 12, 24 or 48 hours. For both NSCs and ECs, intracellular agent concentration was higher with increasing concentration and incubation time (**Figure 4.7**A). Cell survival showed the opposite response, decreasing with increased concentration and incubation time (**Figure 4.7**B).

For electroporation, an initial range of conditions for testing was determined for each cell type using a fluorescent proxy agent, carboxyfluorescein (see section 4.2.3.1). Cells were suspended at 3, 6 or 9 million cells/ml in electroporation buffer with agent at 200mM and electroporated. Cell uptake and survival was measured as for pinocytosis. For both cell types, using harsher electroporation conditions (higher voltage or pulse length) increased agent uptake, although there was a larger effect in ECs. Cell density decreased uptake in NSCs, but had no effect on ECs (**Figure 4.7**C). As with pinocytosis, cell survival showed the opposite pattern to cell uptake, with harsher conditions resulting in decreased survival in both cell types. Cell density increased survival in NSCs, but not ECs (**Figure 4.7**D).

It is unclear from these results whether the decreases in cell survival are due to the presence of more agent within the cell, or to exposure to toxic conditions during the labeling protocol. If the imaging approach is feasible, further experiments will be required to determine effects on survival over time, as well as other parameters, such as proliferation and differentiation. Based on these data and preliminary imaging experiments shown in **Figure 4.2** and **Figure 4.8**, the conditions taken forward were electroporation at 530V, 100μs and 3 x 10^6 cells per ml (**Figure 4.7**, purple arrows). This gives cell pellets with a concentration of 6.8mM for Eu-NSCs and 9.5mM for Yb-ECs. The survival shown here when applied to large numbers of cells to produce pellets for imaging equates to 20% of electroporated Eu-NSCs and 62% of Yb-ECs surviving.

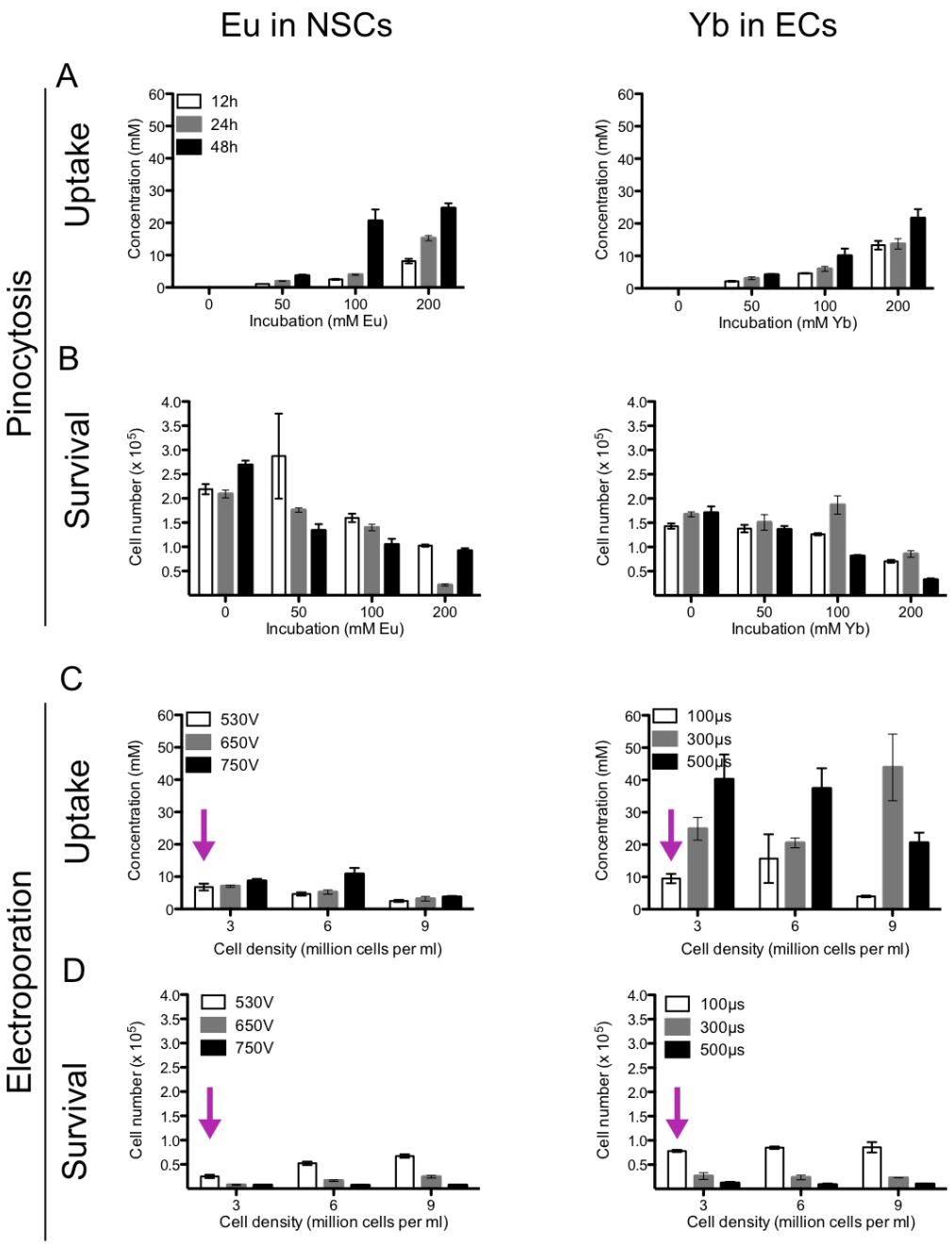

Figure 4.7 Cell uptake and survival after labeling. With pinocytosis, uptake was increased in both cell types by increasing concentration ($F=132$, $p<0.0001$ for NSCs and $F=101$, $p<0.0001$ for ECs) and incubation time ($F=72$, $p<0.0001$ for NSCs and $F=12$, $p<0.001$ for ECs), with a significant interaction between time and concentration ($F=20$, $p<0.0001$ for NSCs and $F=13$, $p<0.05$ for ECs) (**A**). Survival was decreased in both cell types by increasing concentration ($F=29$, $p<0.0001$ for NSCs and $F=64$, $p<0.0001$ for ECs) and incubation time ($F=6$, $p<0.01$ for NSCs and $F=22$, $p<0.0001$ for ECs), with a significant interaction between time and concentration ($F=4$, $p<0.01$ for NSCs and $F=8$, $p<0.001$ for ECs) (**B**). For electroporation in NSCs, uptake was increased by increasing voltage ($F=12$, $p<0.001$) and decreased by increasing cell density ($F=24$, $p<0.0001$). For ECs, uptake by electroporation was increased by increasing pulse length ($F=13$, $p<0.0001$), but was not affected by cell density ($F=0.1$, $p=0.90$) (**C**). In NSCs, survival after electroporation was decreased by increasing voltage ($F=259$, $p<0.0001$) but increased by increasing cell density ($F=55$, $p<0.0001$). For ECs, survival after electroporation was decreased by increasing pulse length ($F=197$, $p<0.0001$), but was not affected by cell density ($F=0.02$, $p=0.98$) (**D**). Purple arrows indicate conditions taken forward.

4.3.3 In vitro cell imaging

The uptake method has previously been shown to affect MRI detection independently of concentration due to the intracellular localisation of agent (Di Gregorio, Ferrauto et al. 2013). Since ParaCEST agents are highly pH sensitive (Delli Castelli, Terreno et al. 2011), localisation to the endosomes and subsequent fusion of the endosomes with low pH lysosomes is likely to reduce detection. To assess this in the current experiment, ECs were labeled with Yb via pinocytosis and electroporation to give cell pellets with similar intracellular concentrations. Cells were labeled by pinocytosis at 100mM incubation concentration for 48h, giving a concentration of 10.1mM, and via electroporation at 200mM, 530V, 100μs and 3 x 10^6 cells per ml to give a concentration of 9.5mM. These two cell pellet samples were then imaged at 9.4T to compare the contrast level for each method.

Despite having similar concentrations, the cells generated using electroporation gave a stronger signal at 97ppm than those generated using pinocytosis (**Figure 4.8**A). The agents have a strong T2 shortening effect, which is greater for cells labeled by pinocytosis than electroporated cells, although this is not statistically significant (**Figure 4.8**B). This does not interfere with agent detection, provided a very short TE is used (<10ms), but may interfere with anatomical imaging for in vivo applications. Z spectra were generated using image acquisitions at 66-71 and 95-100ppm at 1ppm per step, with reference images at 0 and -300ppm, with remaining data points fitted using smoothing splines (section 4.2.5). Electroporated cells had slightly higher contrast than pinocytosis labeled cells at both exchange sites (**Figure 4.8**C). The site showing the most contrast was 97ppm, the opposite of agent solution, where the higher contrast is seen at 69ppm.

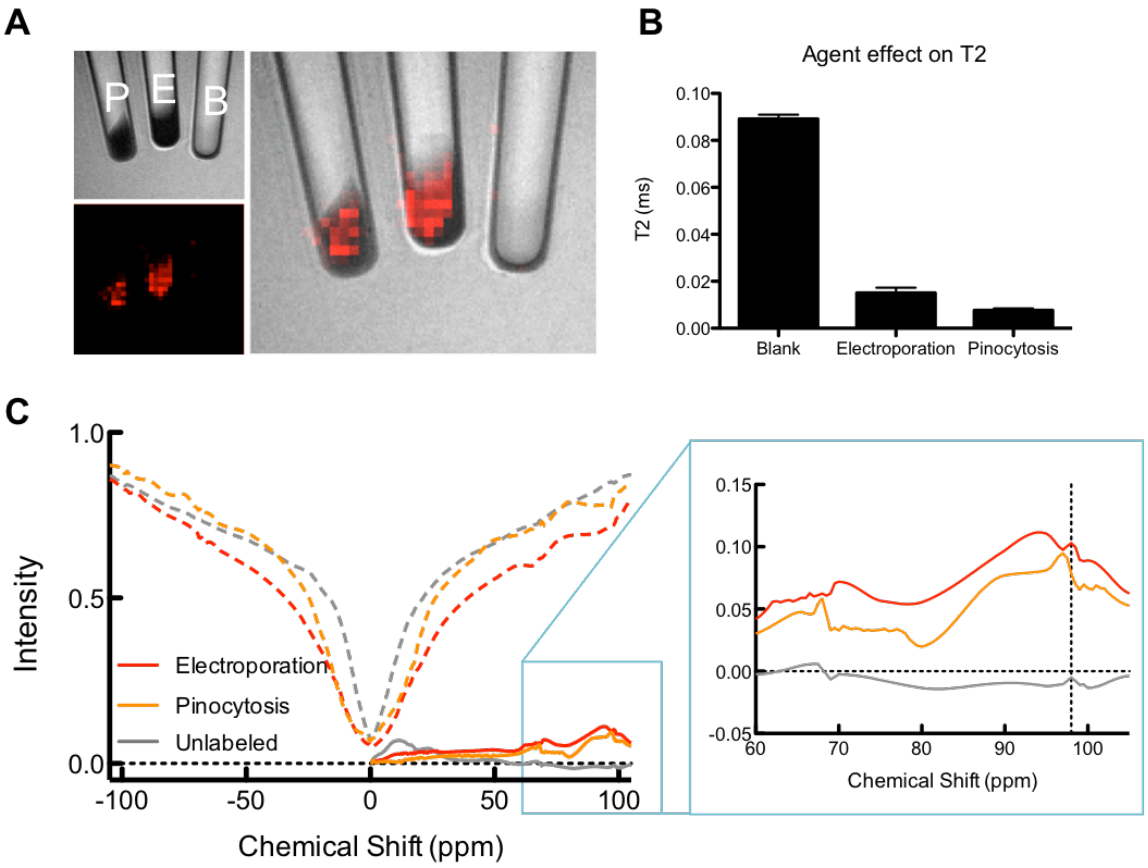

Figure 4.8 MRI detection of cells labeled via pinocytosis or electroporation. Cells labeled via electroporation showed a stronger contrast at 97ppm than those labeled via pinocytosis (**A**). The T2 of the cell pellet was much shorter for labeled compared to unlabeled cells, and was even shorter for pinocytosis cells than electroporated cells. Data is shown as mean ± stdev representing variation within the image (B). The z spectra shows increased contrast for electroporated (0.11) compared to pinocytosis (0.083)

4.3.4 Magnetisation Transfer (MT) Effects

Comparing the shapes of the z spectra in the previous experiments, a clear difference can be seen between those acquired in solution (**Figure 4.6**) and in cells (**Figure 4.8**). Spectra acquired in solution have a narrow water peak at 0ppm with clearly defined peaks associated with each agent, whereas in cells the water peak becomes much wider. This is thought to be due to the magnetisation transfer (MT) effect. This occurs due to the matrix-like nature of biological structures, such as cell membranes, cytoskeletons end extracellular matrix. Excitation of bulk water in this scenario can be transferred through large biological molecules to other protons slightly off-resonance; thereby causing a widening of the water peak. To assess whether this is the cause of the differences observed, the four-pool (free water, Eu, Yb, MT) Bloch-McConnell equation was solved numerically in MATLAB using the experimental conditions and tissue

properties for the four pools. The agent concentration is set as 10mM. The solution z spectra show the asymmetry peaks for the exchange sites at 18ppm for Eu and at 69 and 97ppm for Yb (**Figure 4.9**A). Brain tissue without agent under the detection conditions for each agent shows a much wider peak, but no asymmetry as the signal is non-specific. The widening of the peak is slightly more apparent for Yb, due to the higher power used (**Figure 4.9**B). When the agent is added to brain tissue, the amount of contrast is reduced. This is much more noticeable for Eu, as the exchange site is much closer to water, within the region where MT effects are strongest. For Yb, the exchange site at 69ppm is affected more strongly than that at 97ppm, supporting the experimental data and showing that 97ppm should be the site to target for in vivo detection (**Figure 4.9**C).

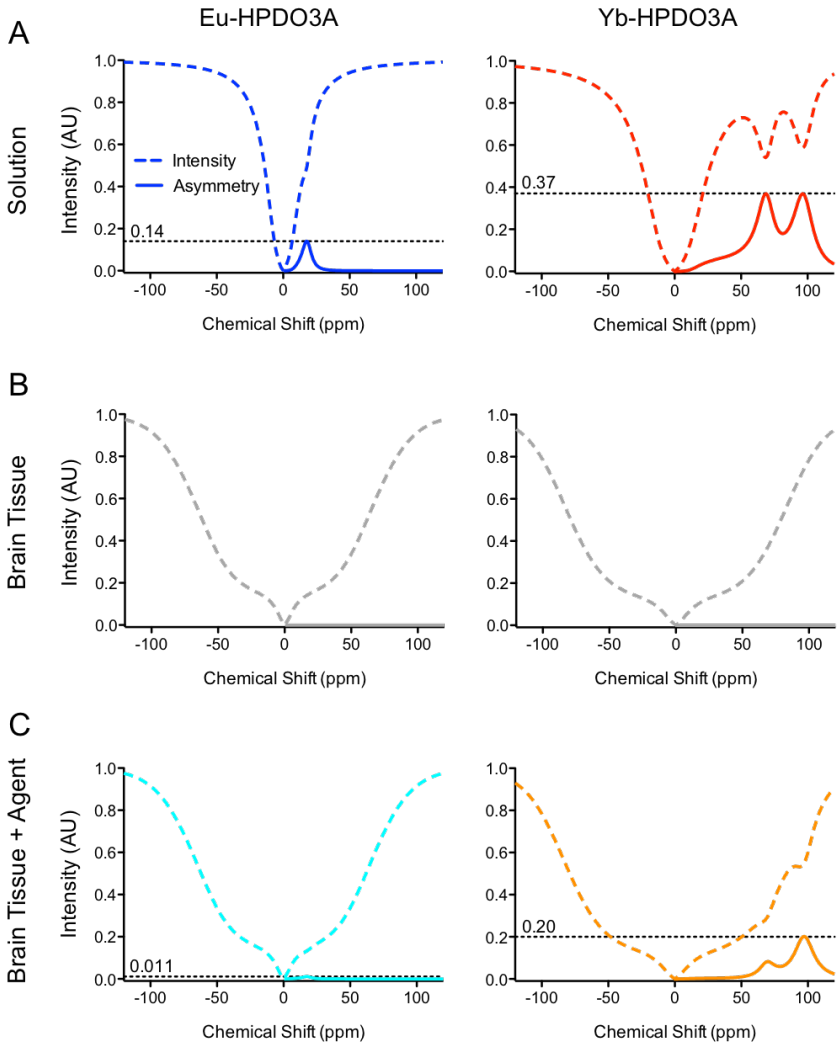

Figure 4.9 Magnetisation Transfer (MT) Effect simulation. Numerical calculation of Bloch-McConnell equation shows similar z spectra to experimentally acquired data of agent in solution (A). MT effects in brain tissue widen the water peak (B), resulting in decreased agent contrast (C).

4.3.5 Feasibility of dual population detection

MT effects result in a large reduction in contrast. Therefore the feasibility of dual population detection must be considered. Cell pellets of Eu-NSCs and Yb-ECs were imaged and the amount of contrast was determined for each agent in order to predict a cell ratio where both agents could be detected.

Eu-NSCs showed only a very small amount of contrast at 0.011, or 1.1% (**Figure 4.10**A). Yb-ECs, however, showed much better contrast at 97ppm at 1.2 or 12% (**Figure 4.10**B). Cells were therefore mixed at a ratio of 4:1:1 EuNSCs:YbECs:Blank cells. Blank cells were included to allow volume for the liquid vehicle that would dilute cells injected in vivo. Imaging of the mixture showed that both agents could still be detected, with Eu contrast at 1.1% above blank cells, and Yb contrast at 2.4% above blank (**Figure 4.10**C). Since CEST-MRI is an inherently low-sensitivity technique, image averaging is often used to improve contrast (Akansu, Serdijn et al. 2010). 15 averages were acquired for Eu, and the contrast was increased slightly from 1.1 to 1.2% (**Figure 4.10**D). However, the time constraints imposed by cell viability and the long TR required to offset SAR effects limit the number of averages that can be obtained.

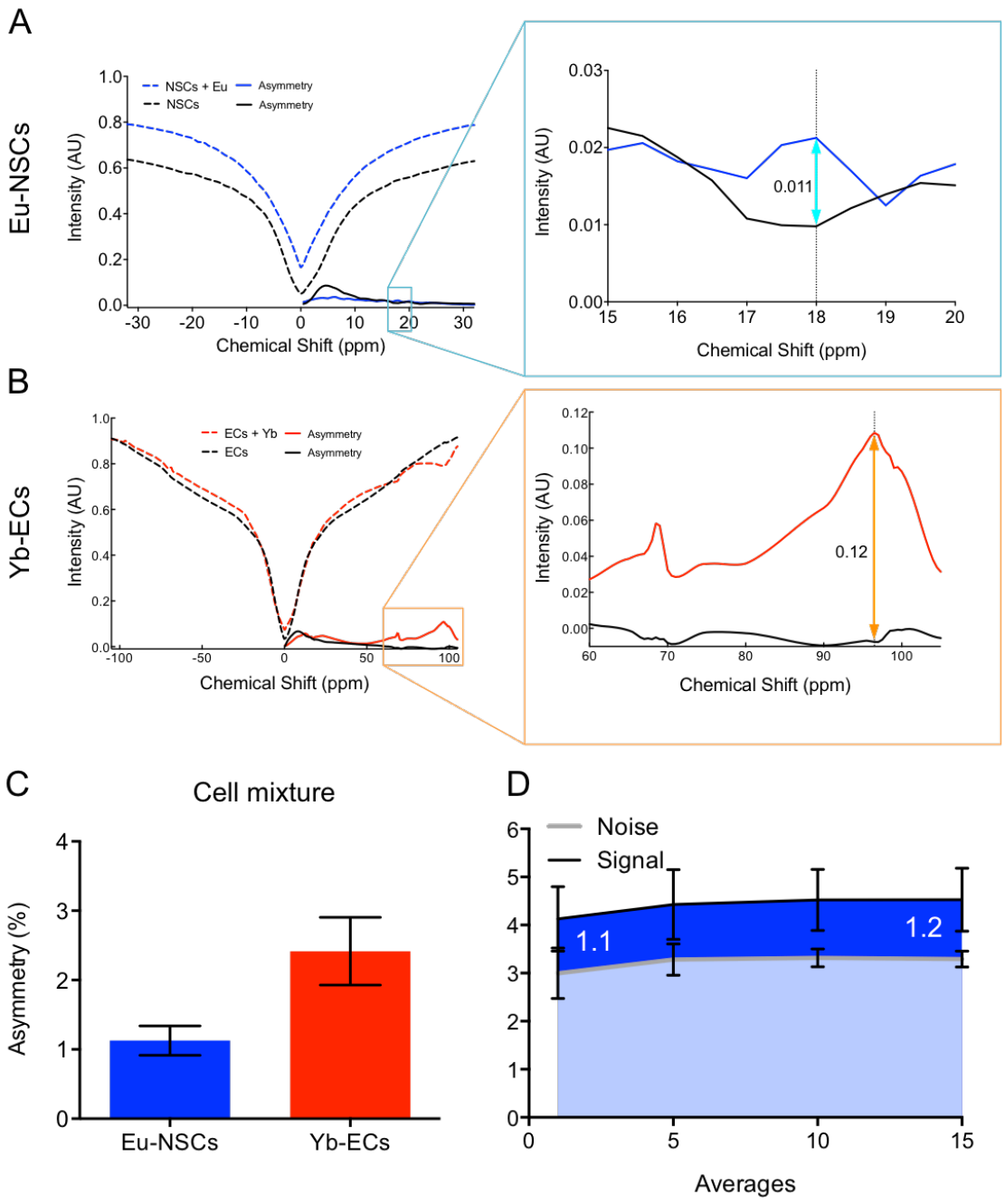

Figure 4.10 Cell ratio. Cell pellets were imaged to assess the contrast available from each agent, Eu 0.011 (A) and Yb 0.12 (B). Eu-NSCs, Yb-ECs and blank cells were then mixed in the ratio 4:1:1, and both cell types were detectable (C). Image averaging was used to improve contrast, but only a modest increase could be seen within the time constraints (D).

4.3.6 In vivo imaging

A potential application of paraCEST imaging would be to visualise two cell populations in vivo in the context of tissue engineering. Ischemic stroke results in a loss of tissue, leaving a fluid filled cyst. Cell therapies have shown promise in stroke, reducing lesion volume and improving motor

recovery. However, complete recovery has not been shown, making tissue engineering within the cavity an attractive avenue to pursue. NSCs and ECs were implanted directly into the lesion 2-4 weeks after middle cerebral artery occlusion (MCAO) surgery, and images were acquired the following day.

The first implantation of labeled cells was performed before the problem of MT effects had been accounted for. Since Yb at 69ppm appeared to have better contrast (**Figure 4.6**A), and requires lower RF irradiation power, the Yb at 69 ppm was chosen. RF power = 46μT, and RF duration = 800ms. Cells were labeled by electroporation (200mM, 530V, 100μs), and implanted at a ratio of 10:6 Yb-ECs:Eu-NSCs at a total density of 200,000 cells/μl. This gives a predicted concentration in the lesion of 4.75mM Yb and 2.04mM Eu. Images revealed sufficient contrast to visualise both agents within the lesion (**Figure 4.11**A). However, with the image threshold at the noise level of the contralateral hemisphere, it can be seen that rather than a continuous area of contrast, individual pixels are visible. This shows that the contrast is at the low limit of detection in comparison to background. After optimization of the sequence, unlabeled cells were transplanted in order to assess whether differences between the transplant area and contralateral hemisphere were sufficient to produce false positive contrast (**Figure 4.11**B).

To get a numerical value for contrast, the asymmetry was measured for each voxel within the ROIs selected on the T2 images. This was then plotted as mean asymmetry ± standard deviation (**Figure 4.11**C). For the labeled cell transplant, contrast was significantly higher in the transplant site compared to the contralateral hemisphere for both agents. The difference for Eu was small but significant ($p<0.001$), with high background at 2.2%, and signal at 2.5%. For Yb, the difference was larger at 1.5% signal compared to 0.8% background, reflecting the reduced noise at a higher ppm, and increased signal due to the higher concentration. For the unlabeled cell transplant, the Eu asymmetry for the transplant site was slightly lower then the contralateral side (Signal 1.4%, background 1.5%), but not significantly different ($p=0.62$). For Yb, signal was -1.0%, and background -2.0%. There was a significant difference ($p<0.001$) here, showing that the differences between the lesion transplant and healthy tissue are sufficient to produce a false positive Yb contrast. This is due to MT asymmetry, and the difference in the biomolecule bound proton pool between healthy tissue and newly transplanted cells, which are in suspension without extracellular matrix. This could potentially be improved by transplanting cells within an ECM hydrogel to reduce differences between the transplant and healthy tissue.

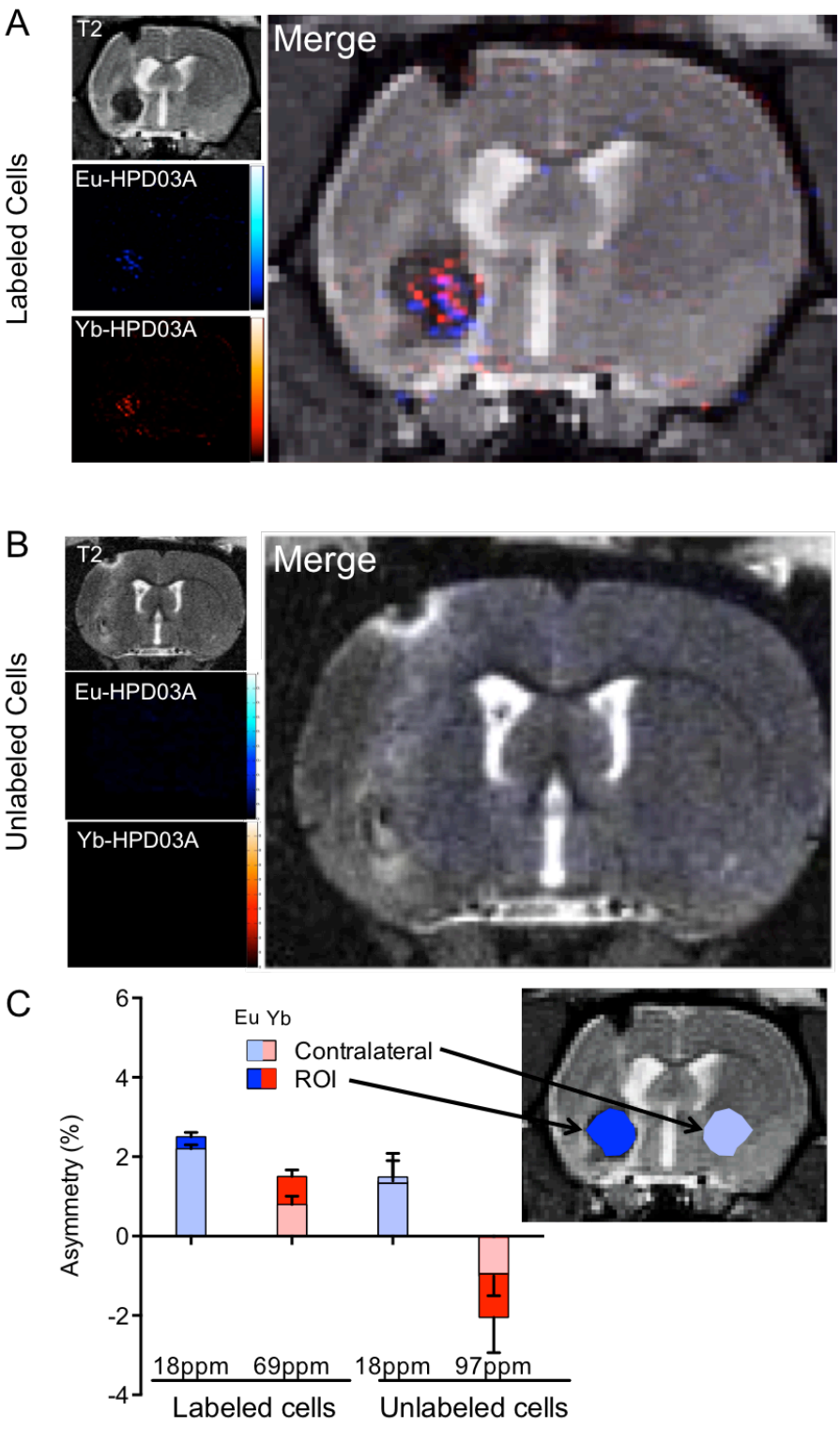

Figure 4.11 In vivo images acquired 1 day after transplantation into the stroke lesion of either labeled (A) or unlabeled cells (B). The mean contrast for each ROI was plotted as mean ± stdev and t tests were used to compare transplant site with the contralateral hemisphere. For labeled cells, contrast was significantly higher in the transplant site for both Eu ($p<0.001$) and Yb ($p<0.001$). For unlabeled cells, contrast was not significantly different for Eu ($p=0.62$), but was different for Yb ($p<0.001$) (C)

4.4 Discussion

ParaCEST MRI offers exciting possibilities for tracking multiple cell populations over time, which is becoming an increasingly important consideration for tissue engineering applications. We here tested the potential of two paraCEST agents, Eu-HPDO3A and Yb-HPDO3A, for cell identification in a stroke model. Agents could be detected independently in solution, but their detection when inside cells was hampered by magnetization transfer (MT) effects. In vivo, Eu labeled cells could be detected, but at the RF power required for Yb, the MT asymmetry in healthy tissue was high, masking differences due to cell labeling.

4.4.1 Limitations of methodology

Due to the technical challenges, this project was much more time consuming than expected. As a result, the methodology leaves much to be desired. Firstly, the final in vivo images were obtained from only one rat in each group. Particularly given the small effect size and the high level of unspecific signal from MT asymmetry, replicates would be required to confirm the result that Eu-(but not Yb-)labeled cells can be reliably detected in vivo. Cell pellet experiments were also n=1 for each specific comparison, but these results taken together with optimisation experiments provide some level of confidence that cell pellet detection is reliable for both agents. However, further replicates would of course still be desirable.

The other major issue relates to biological relevance. Due to the low sensitivity of paraCEST, the cell mixture injected was based on maximising the concentration of both agents rather than the most promising biological paradigm. Cells were injected at 200,000 cells/µl, which is much more dense than the host brain tissue, but allowed for a higher agent concentration. The NSC:EC ratio was also adjusted based on optimal imaging conditions rather than optimal biology for tissue formation. However, this study was designed to explore the suitability of these agents for imaging these two cell populations, rather than to examine the biological processes. If further work were to be done on this project with an improved agent design, these aspects would need to be taken into account, as well as a more thorough assessment of the functionality of labeled cells. The electroporation process decreased cell survival and it is therefore likely that there were detrimental effects on surviving cells that were not picked up with the assay undertaken here. A more thorough characterisation should include differentiation of NSCs as well as a matrigel tube formation assay for ECs and long term survival for both cell types.

4.4.2 Challenges in paraCEST imaging

The major challenge encountered here was MT effects, of which there are two aspects. Firstly, conventional MT refers to the widening of the water peak, as shown in **Figure 4.9**, whereby magnetisation is transferred through large biological molecules, reducing the specificity of excitation. The second type is MT asymmetry, which is thought to arise from a shift difference between the solid-like macromolecular chemical shift centre and bulk water resonance (Hua, Jones et al. 2007), and is likely responsible for the negative asymmetry values seen in Yb background in vivo. These cause a reduction in contrast compared to the same concentration in solution, and further exacerbate the problem of a high detection threshold. Increasing the power of the saturation pulse can increase contrast, but also increases MT effects, in addition to sample heating. Improving intracellular concentration or the CEST properties of the agents are therefore attractive options to improve detection. We have shown here that intracellular concentration can be increased, but that it comes at a high cost of cell survival. The electroporation conditions used for imaging gave 1.6-2.2 x 10^6 Ln/cell, which is similar to that achieved by others using Gd in the same chelate (Di Gregorio, Ferrauto et al. 2013). It is therefore evident that a change in the agent would be required to further increase uptake, such as conjugation to nanoparticles. This may also provide opportunities to manipulate the chemistry, such that the exchange rate could be optimised, which would further improve contrast (Siriwardena-Mahanama and Allen 2013). However, altering the exchange rate appears to be less straightforward for paraCEST agents than traditional MR contrast agents. A recent study aimed to conjugate EuDOTA-$(gly)_4$ to silica nanoparticles to reduce the exchange rate, but found instead that the signal was quenched by excess amino protons on the particle surface (Evbuomwan, Merritt et al. 2012). It seems therefore that significant advances are required before uptake and exchange rate can be improved in this manner, and that suitable materials must be chosen with the utmost care.

A recent publication shows a related technique of highly shifted proton MR imaging (Schmidt, Nippe et al. 2014), where lanthanide based agents with a large chemical shift are directly detected using attached methyl groups. This technique potentially has much improved sensitivity, with in vitro detection at 25μM, compared to ~2mM required here for paraCEST, and may therefore be a more promising avenue for this application. However, there is additional equipment required for imaging, which may hamper any clinical translation.

4.4.3 Alternative uses of CEST

An alternative approach to cell tracking is the use of a CEST reporter gene. By over-expressing hPRM1, Bar-Shir, Liu et al. (2014) could detect HEK293 cells in a 3D culture system. When compared to wild type cells, the difference in contrast was ~0.2%, similar to the contrast achieved here with Eu. However, the chemical shift of hPRM1 is 1.5ppm, meaning that a very low power of 3.6μT can be used. This potentially reduces heating effects and may therefore allow the use of a much shorter TR, which could significantly reduce scanning time, or allow more averages to be obtained. They note, however, that this was only in vitro, and contrast in vivo may be somewhat different.

Tissue engineering poses unique challenges to the imaging field, and CEST MRI may have other applications besides cell tracking. Vascularization of the graft is a key process, and targeted lipoCEST may be one way to image this. Flament, Geffroy et al. (2013) used intravenous RGD-lipoCEST to target $\alpha_u\beta_3$ integrin, which is upregulated during tumour vascularisation. Using this approach, they were able to visualise increased contrast in the tumour compared to the contralateral hemisphere. However, the expression level of angiogenesis markers in transplants has not been widely assessed and the levels may be significantly lower than tumorigenesis. Attempts to use molecular MRI to visualise post-stroke increases in PECAM-1 expression using MPIOs have not been successful (Deddens, van Tilborg et al. 2013).

4.5 Conclusions

We here assessed the potential of paraCEST for detection of multiple cell populations. The agents Eu-HPDO3A and Yb-HPDO3A can be selectively detected in solution, and can label calls via pinocytosis or electroporation. When separate populations of cells are labeled with the two agents, these can be selectively detected in vitro. However, the presence of MT effects reduce the contrast compared to detection in solution. In vivo, MT asymmetry is an even larger problem, as the difference between newly transplanted cells and healthy tissue including extracellular matrix is large enough to generate false positive contrast at the high RF power required for Yb detection. At the lower power required for detection of Eu-labeled cells however, a small but significant difference was observed compared to unlabeled transplant. This demonstrates that paraCEST imaging of multiple populations does have potential, but further replicates would be required to verify this, and significant changes in agent chemistry are required before they become applicable to tissue engineering.

Chapter 5: Discussion

In this thesis, current and novel methods for identifying transplanted cells have been assessed. As transplants become more sophisticated, the demands on identification methods increase. We have here shown some of the strengths of current methods, as well as their limitations for more complex environments.

5.1 Exogenous labels for identification of transplanted cells

Exogenous labels refers to labels added to a population of cells prior to transplantation, and applies both to histological labels, such as Hoechst and PKH26, and also to those used for in vivo imaging methods, such as iron oxide and gadolinium labels for MRI.

The primary concern with exogenous labels is their potential for errant labeling of host cells. This problem has been demonstrated for Hoechst (Iwashita, Crang et al. 2000), where Hoechst was found both to label a region of host cells surrounding the graft, and to persist after transplanted cells were no longer present. BrdU was considered more reliable in this respect due to its cellular incorporation only occurring during DNA synthesis and it being permanently integrated into DNA. However, in the injured brain, DNA synthesis is occurring during damage repair, as well as gliosis. Consequently, BrdU has been shown in host cells after transplantation of live cells, dead cells or label alone (Burns, Ortiz-Gonzalez et al. 2006). It is therefore clear that these labels are taken up by host cells, and that the presence of free label must be minimized. This problem becomes exacerbated in the context of MRI, where Gd-based labels in solution have a larger effect on relaxivity than labels within cells (Kok, Hak et al. 2009).

By allowing 24 hours between completion of labeling and cell transplantation, as recommended by Lassailly, Griessinger et al. (2010), we here showed very little leakage of exogenous labels (i.e. false positive) for BrdU, PKH26, and Qtracker in vivo. What was observed instead was a significant number of false negatives, where transplanted cells were negative for the exogenous label. This highlights the difficulties in relying on previously published data to select a label for a specific application. The labeling protocol, cell type and in vivo model are all likely to have significant effects on label reliability.

Cell survival after transplantation currently remains low, meaning that the majority of transplanted cells will die (Smith, Stroemer et al. 2011). The eventual fate of a label after cell death requires investigation, as has been demonstrated by transplantation of SPIO labeled cells in immune competent and immune deficient mice, where signal was shown to persist more strongly in immune-competent mice where the transplant was rejected and cells died (Berman, Galpoththawela et al. 2011). The use of reporter genes, such as ferritin, have been shown to overcome this problem (Naumova, Balu et al. 2014). However, for Gadolinium this may not be an issue since the chelated molecule is smaller and able to diffuse away from the graft site more easily upon cell death (Guenoun, Ruggiero et al. 2013). This was corroborated by the data shown here, where GdAuNP MR contrast was no longer visible after cell death.

5.2 Challenges in cell tracking

The primary challenge in cell tracking remains that of the observer effect, where the attempt to observe the behaviour of the cells by applying labels can alter that behaviour. Some studies still rely solely on cell toxicity and proliferation tests to assess the suitability of a tracking method. However, measuring long-term survival and phenotypic effects are vital in order to avoid affecting the therapeutic efficacy of a graft. Our work showed that even commonly used histological labels showing no acute effect on cell viability can have significant effects on cell survival even one week later. Extending this measure to a three week differentiation protocol as used by El Akabawy, Martinez-Medina et al. (2011) would allow us to ascertain whether the phenotypic effects can be negated by the use of small molecules to direct differentiation, or whether the differences are magnified by the longer time course.

In order to take any cell tracking method forward for use in a therapeutic efficacy study, the predicted therapeutic mechanism of the implant should be taken into consideration. For studies aiming to achieve integration and long-term survival of grafted cells, assessment should be extended to include synapse formation and generation of action potentials (Sekar, Kizana et al. 2007).

However, in vitro models cannot accurately model all the environmental conditions that cells may encounter in vivo and as such, unexpected effects may still occur even after rigorous testing. The inclusion of an unlabeled cell control therefore unfortunately remains necessary to establish the absence of label effects (Modo, Beech et al. 2009). This begins to erode the utility of cell labeling,

as the workload is essentially doubled for each study with a new label, and thereafter every time the cell line, label or animal model is altered. Finding endogenous markers of transplanted cells therefore becomes much more appealing. However, this is much easier for histological labels than for MRI. Histology's high resolution allows it to take advantage of small differences, such as cell gender, as the presence of a Y chromosome can be visualised using in situ hybridisation (ISH) (Hruban, Long et al. 1993). The use of cell type specific proteins, however, should be undertaken with care. In the context of regenerative medicine, significant changes in transplanted cells are expected and as such a marker labeling the whole population in vitro may not necessarily be as reliable over time in vivo.

Cell tracking in vivo has additional challenges to overcome. Particularly for the brain, the presence of the skull means that non-invasive cell visualisation must rely on modalities with much lower sensitivity and resolution. The careful design of contrast agents can provide great improvements. The GdAuNP agent used here was designed specifically for good cell uptake and compatibility, and use at high field after feedback from experiments with GRID (Brekke, Morgan et al. 2007, Modo, Beech et al. 2009), and showed potential for reliable cell identification. The paraCEST agents are somewhat newer and have not been optimised for this system, and our experiments showed that they are not yet reliable. However, the data generated here can be used to inform improved design of the next generation of agent.

5.3 Imaging tissue engineering

Although tracking individual transplant components can provide valuable data, there are other parameters to consider in tissue engineering. An additional challenge is to indicate if implanted cells have generated an appropriate type of tissue. Establishing if a tissue is developing is significantly more challenging than establishing if implanted cells have differentiated into one appropriate neuronal phenotype, which can be achieved using MRS (Chung, El Akabawy et al. 2013). The primary question is whether a tissue has developed with appropriate diffusion barriers (e.g. ECM, axons), as these are essential to keep the tissue together. Their presence can be visualised using diffusion-weighted MRI (Bible, Dell'acqua et al. 2012). However, diffusion barriers also limit the flow of extracellular fluid typically found inside the lesion cavity, potentially reducing the supply of nutrients to grafted tissue. It is therefore important to ensure delivery of nutrients and oxygen to the de novo tissue by angiogenesis, as well as arteriogenesis. Monitoring the

emergence of an appropriate blood supply to this area is consequently crucial for its long-term survival (Boehm-Sturm, Farr et al. 2013). Perfusion MRI can demonstrate appropriate flow of blood to the area, whereas MR angiography can visualize the presence of major blood vessels (Seevinck, Deddens et al. 2010). However, all these aspects are also present in tumours and therefore the site-appropriateness of the de novo tissue also requires interrogation.

Replacing lost striatal tissue with a new tissue that has the biochemical properties of the original tissue does not necessarily translate into recovery, as cells must also integrate into neural networks of the host brain. Glial scarring and the lack of appropriate axonal connections can potentially form a tissue that is not connected. Therefore appropriate in vivo methods need to be developed to establish if the newly formed tissue is responsive to input from the host brain and vice versa that the regrown striatum can indeed elicit activity in the host brain. Pharmacological MRI is one means to investigate if the new striatum is specifically responsive to agents that stimulate striatal neuron activity (Chen, Brownell et al. 1999, Roberts, Price et al. 2007). After fetal tissue transplants, functional MRI has, for instance, also been used to demonstrate the integration of the new tissue with host activity (Bluml, Kopyov et al. 1999). It is also conceivable that if a new tissue is integrated with the brain it will fire spontaneously and in the absence of a regulatory feedback can be the focal point for epileptic discharges. Electroencephalography (EEG) can help to establish if inappropriate discharges are indeed occurring, in the absence of behavioural manifestations. Appropriate monitoring of the functional integration of cells will also be important to ensure the safety of this approach.

Although the connections between new and existing tissue are thought to be essential to provide an integration into networks that produce behaviour, merely establishing physical synaptic connections is unlikely to be sufficient to ensure that this new tissue is indeed functionally integrated (Hicks, Hewlett et al. 2007). As during development, these new neurons are likely to be a “blank slate” and they will require functional activity from other cells to establish and maintain a functional integration (Dobrossy, Busse et al. 2010). Rehabilitative training specifically geared towards integrating these newly established cells and connections is likely to be a major requirement to ensure the efficacy of this approach. It is likely that the rehabilitative needs of this tissue are very different from those currently employed to promote recovery after stroke. Rehabilitation after stroke is geared towards promoting plasticity in remaining brain regions, but is

not necessarily appropriate to train a new tissue or guarantee its integration with other brain regions. Therefore significant challenges remain ahead.

In summary, we here highlight some of the issues that remain even when using simple histological dyes to identify transplanted cells, and recommend diligent assessment of their cellular effects and reliability before use. The results shown here and elsewhere demonstrate the high variability in reliability between labels, cell types, labeling protocols and in vivo models, and demonstrate the need for highly individualised assessment of cell labeling for each proposed application. We also introduce GdAuNPs as an MRI contrast agent providing highly specific cell detection on T1 weighted images without interfering with T2 weighted anatomical imaging, demonstrating a significant improvement compared to previous Gd labels, although its utility in tracking over time remains to be assessed. Finally, we introduce paraCEST as a technique with the potential to image multiple transplant components for tissue engineering. However, we here show that there are issues with background signal, and that significant improvements are required before this technique becomes applicable to tissue engineering. In the context of regenerative medicine and increasingly complex transplants, it seems that labeling transplant components comes with a high cost in terms of cellular effects, and therefore potentially therapeutic efficacy, whereas monitoring tissue formation and graft activity are potentially free of this cost. Future study designs must take this into account to assess whether the additional data generated is sufficient recompense.

Appendix 1: MATLAB script for reading intensity of fluorescence images

```
function []=readmeancolor(pathin)

pwd

cd(pathin)

A=dir;

Asize=length(A)

for i=1:Asize

    if ~isdir(A(i).name)

       DATA=[];

       DATA=imread(A(i).name);

       R=DATA(:,:,1);

       G=DATA(:,:,2);

       B=DATA(:,:,3);

       Ri=mean(R(:));

       Gi=mean(G(:));

       Bi=mean(B(:));

       disp([A(i).name,'    ',num2str(Ri),'     ',num2str(Gi),'      ',num2str(Bi)])

    end

end
```

Appendix 2: Parameters and matrix forms of the Bloch-McConnell equation

The Bloch-McConnell equation takes the form:

$$\frac{d}{dt}\begin{bmatrix} M_a \\ M_b \\ M_c \\ M_d \end{bmatrix} = \begin{bmatrix} \boldsymbol{L_a - K_{ab} - K_{ac} - K_{ad}} & \boldsymbol{K_{ba}} & \boldsymbol{K_{ca}} & \boldsymbol{K_{da}} \\ \boldsymbol{K_{ab}} & \boldsymbol{L_b - K_{ba}} & \mathbf{0} & \mathbf{0} \\ \boldsymbol{K_{ac}} & \mathbf{0} & \boldsymbol{L_c - K_{ca}} & \mathbf{0} \\ \boldsymbol{K_{ad}} & \mathbf{0} & \mathbf{0} & \boldsymbol{L_d - K_{da}} \end{bmatrix} \times \begin{bmatrix} M_a \\ M_b \\ M_c \\ M_d \end{bmatrix} + \begin{bmatrix} \frac{M_{0a}}{T_{1a}} \\ \frac{M_{0b}}{T_{1b}} \\ \frac{M_{0c}}{T_{1c}} \\ \frac{M_{0d}}{T_{1d}} \end{bmatrix}$$

$$L_i = \begin{bmatrix} -\frac{1}{T_{2i}} & -\Delta\omega_i & 0 \\ +\Delta\omega_i & -\frac{1}{T_{2i}} & +\omega_i \\ 0 & -\omega_i & -\frac{1}{T_{2i}} \end{bmatrix}$$

$$K_{ij} = \begin{bmatrix} k_{ij} & 0 & 0 \\ 0 & k_{ij} & 0 \\ 0 & 0 & k_{ij} \end{bmatrix}$$

$$\mathbf{0} = \begin{bmatrix} 0 & 0 & 0 \\ 0 & 0 & 0 \\ 0 & 0 & 0 \end{bmatrix}$$

$$M_i = \begin{bmatrix} M_{ix} \\ M_{iy} \\ M_{iz} \end{bmatrix}$$

$M_{0i} = \begin{bmatrix} 0 \\ 0 \\ p_i \end{bmatrix}$ is the initial state of M_i.

Here T_{1i}, T_{2i} are relaxation parameters of each pool; $\Delta\omega_i$ is saturation offsets of each pool; ω_i is RF amplitude; k_{ij} is the exchange rate from pool i to pool j; p_i is the ratio of each pool, and $p_a + p_b + p_c + p_d = 1$; k_{ij} and k_{ji} are related by pool ratio, e.g. $p_i \times k_{ij} = p_j \times k_{ji}$.

Table of parameters, showing all input values used:

Water pool:	Free	Biol. Mol	Eu 18ppm	Yb 69ppm	Yb 97ppm
T1 (s)	1.4	0.1	0.77	0.77	0.77
T2 (s)	0.04	0.0000092	0.033	0.033	0.033
Δωi (offset, ppm)	0	0	18	69	97
Ratio	0.92	0.08	0.0001	0.0001	0.0001
k to free water (measured, s-1)	-	50	5,000	10,000	15,000
k from free water (calculated, s-1)	-	4.35	0.54	1.09	1.63
RF power (μT)	-	-	28	48	48
RF duration (s)	-	-	0.8	1	1

References

Adamczak, J and Hoehn, M (2012). "In vivo imaging of cell transplants in experimental ischemia." Prog Brain Res **201**: 55-78.

Adamczak, JM, Schneider, G, Nelles, M, Que, I, Suidgeest, E, van der Weerd, L, Lowik, C and Hoehn, M (2014). "In vivo bioluminescence imaging of vascular remodeling after stroke." Front Cell Neurosci **8**: 274.

Agashi, K, Chau, DY and Shakesheff, KM (2009). "The effect of delivery via narrow-bore needles on mesenchymal cells." Regenerative medicine **4**(1): 49-64.

Ahmed, M and Masaryk, TJ (2004). "Imaging of acute stroke: state of the art." Semin Vasc Surg **17**(2): 181-205.

Aime, S, Carrera, C, Delli Castelli, D, Geninatti Crich, S and Terreno, E (2005). "Tunable imaging of cells labeled with MRI-PARACEST agents." Angew Chem Int Ed Engl **44**(12): 1813-1815.

Akansu, AN, Serdijn, WA and Selesnick, IW (2010). "Emerging applications of wavelets: A review." Physical Communication **3**(1): 1-18.

Alvarez-Buylla, A, Herrera, DG and Wichterle, H (2000). "The subventricular zone: source of neuronal precursors for brain repair." Prog Brain Res **127**: 1-11.

An, H, Liu, Q, Chen, Y, Vo, KD, Ford, AL, Lee, JM and Lin, W (2012). "Oxygen metabolism in ischemic stroke using magnetic resonance imaging." Transl Stroke Res **3**(1): 65-75.

Anilkumar, P, Wang, X, Cao, L, Sahu, S, Liu, J-H, Wang, P, Korch, K, Tackett Ii, KN, Parenzan, A and Sun, Y-P (2011). "Toward quantitatively fluorescent carbon-based "quantum" dots." Nanoscale **3**(5): 2023-2027.

Arvidsson, A, Collin, T, Kirik, D, Kokaia, Z and Lindvall, O (2002). "Neuronal replacement from endogenous precursors in the adult brain after stroke." Nature medicine **8**(9): 963-970.

Badin, RA, Modo, M, Cheetham, M, Thomas, DL, Gadian, DG, Latchman, DS and Lythgoe, MF (2009). "Protective effect of post-ischaemic viral delivery of heat shock proteins in vivo." J Cereb Blood Flow Metab **29**(2): 254-263.

Balsara, RD, Chapman, SE, Sander, IM, Donahue, DL, Liepert, L, Castellino, FJ and Leevy, WM (2014). "Non-invasive imaging and analysis of cerebral ischemia in living rats using positron emission tomography with 18F-FDG." J Vis Exp(94).

Bang, OY, Lee, JS, Lee, PH and Lee, G (2005). "Autologous mesenchymal stem cell transplantation in stroke patients." Ann Neurol **57**(6): 874-882.

Bar-Shir, A, Liu, G, Chan, KW, Oskolkov, N, Song, X, Yadav, NN, Walczak, P, McMahon, MT, van Zijl, PC, Bulte, JW and Gilad, AA (2014). "Human protamine-1 as an MRI reporter gene based on chemical exchange." ACS Chem Biol **9**(1): 134-138.

Bell, BA, Symon, L and Branston, NM (1985). "CBF and time thresholds for the formation of ischemic cerebral edema, and effect of reperfusion in baboons." J Neurosurg **62**(1): 31-41.

Berman, SC, Galpoththawela, C, Gilad, AA, Bulte, JW and Walczak, P (2011). "Long-term MR cell tracking of neural stem cells grafted in immunocompetent versus immunodeficient mice reveals distinct differences in contrast between live and dead cells." Magn Reson Med **65**(2): 564-574.

Bernau, K, Lewis, CM, Petelinsek, AM, Benink, HA, Zimprich, CA, Meyerand, ME, Suzuki, M and Svendsen, CN (2014). "In vivo tracking of human neural progenitor cells in the rat brain using bioluminescence imaging." J Neurosci Methods **228**: 67-78.

Bible, E, Chau, DY, Alexander, MR, Price, J, Shakesheff, KM and Modo, M (2009). "Attachment of stem cells to scaffold particles for intra-cerebral transplantation." Nat Protoc **4**(10): 1440-1453.

Bible, E, Chau, DY, Alexander, MR, Price, J, Shakesheff, KM and Modo, M (2009). "The support of neural stem cells transplanted into stroke-induced brain cavities by PLGA particles." Biomaterials **30**(16): 2985-2994.

Bible, E, Dell'acqua, F, Solanky, B, Balducci, A, Crapo, PM, Badylak, SF, Ahrens, ET and Modo, M (2012). "Non-invasive imaging of transplanted human neural stem cells and ECM scaffold remodeling in the stroke-damaged rat brain by (19)F- and diffusion-MRI." Biomaterials **33**(10): 2858-2871.

Bible, E, Qutachi, O, Chau, DY, Alexander, MR, Shakesheff, KM and Modo, M (2012). "Neovascularization of the stroke cavity by implantation of human neural stem cells on VEGF-releasing PLGA microparticles." Biomaterials **33**(30): 7435-7446.

Bihel, E, Pro-Sistiaga, P, Letourneur, A, Toutain, J, Saulnier, R, Insausti, R, Bernaudin, M, Roussel, S and Touzani, O (2010). "Permanent or transient chronic ischemic stroke in the non-human primate: behavioral, neuroimaging, histological, and immunohistochemical investigations." J Cereb Blood Flow Metab **30**(2): 273-285.

Bluml, S, Kopyov, O, Jacques, S and Ross, BD (1999). "Activation of neurotransplants in humans." Exp Neurol **158**(1): 121-125.

Boehm-Sturm, P, Farr, TD, Adamczak, J, Jikeli, JF, Mengler, L, Wiedermann, D, Kallur, T, Kiselev, V and Hoehn, M (2013). "Vascular changes after stroke in the rat: a longitudinal study using optimized magnetic resonance imaging." Contrast Media Mol Imaging **8**(5): 383-392.

Boehm-Sturm, P, Mengler, L, Wecker, S, Hoehn, M and Kallur, T (2011). "In vivo tracking of human neural stem cells with 19F magnetic resonance imaging." PLoS One **6**(12): e29040.

Boltze, J, Schmidt, UR, Reich, DM, Kranz, A, Reymann, KG, Strassburger, M, Lobsien, D, Wagner, DC, Forschler, A and Schabitz, WR (2012). "Determination of the therapeutic time window for human umbilical cord blood mononuclear cell transplantation following experimental stroke in rats." Cell transplantation **21**(6): 1199-1211.

Borlongan, CV, Tajima, Y, Trojanowski, JQ, Lee, VM and Sanberg, PR (1998). "Transplantation of cryopreserved human embryonal carcinoma-derived neurons (NT2N cells) promotes functional recovery in ischemic rats." Exp Neurol **149**(2): 310-321.

Brekke, C, Morgan, SC, Lowe, AS, Meade, TJ, Price, J, Williams, SC and Modo, M (2007). "The in vitro effects of a bimodal contrast agent on cellular functions and relaxometry." NMR Biomed **20**(2): 77-89.

Brown, DB and Stanfield, BB (1989). "The use of bromodeoxyuridine-immunohistochemistry to identify transplanted fetal brain tissue." J Neural Transplant **1**(3-4): 135-139.

Brownell, AL, Chen, YI, Yu, M, Wang, X, Dedeoglu, A, Cicchetti, F, Jenkins, BG and Beal, MF (2004). "3-Nitropropionic acid-induced neurotoxicity--assessed by ultra high resolution positron emission tomography with comparison to magnetic resonance spectroscopy." J Neurochem **89**(5): 1206-1214.

Bubnic, SJ, Nagy, A and Keating, A (2005). "Donor hematopoietic cells from transgenic mice that express GFP are immunogenic in immunocompetent recipients." Hematology **10**(4): 289-295.

Buhnemann, C, Scholz, A, Bernreuther, C, Malik, CY, Braun, H, Schachner, M, Reymann, KG and Dihne, M (2006). "Neuronal differentiation of transplanted embryonic stem cell-derived precursors in stroke lesions of adult rats." Brain **129**(Pt 12): 3238-3248.

Burns, TC, Ortiz-Gonzalez, XR, Gutierrez-Perez, M, Keene, CD, Sharda, R, Demorest, ZL, Jiang, Y, Nelson-Holte, M, Soriano, M, Nakagawa, Y, Luquin, MR, Garcia-Verdugo, JM, Prosper, F, Low, WC and Verfaillie, CM (2006). "Thymidine analogs are transferred from prelabeled donor to

host cells in the central nervous system after transplantation: a word of caution." Stem Cells **24**(4): 1121-1127.

Byers, B, Lee, HJ, Liu, J, Weitz, AJ, Lin, P, Zhang, P, Shcheglovitov, A, Dolmetsch, R, Pera, RR and Lee, JH (2015). "Direct in vivo assessment of human stem cell graft-host neural circuits." Neuroimage **114**: 328-337.

Cabella, C, Crich, SG, Corpillo, D, Barge, A, Ghirelli, C, Bruno, E, Lorusso, V, Uggeri, F and Aime, S (2006). "Cellular labeling with Gd(III) chelates: only high thermodynamic stabilities prevent the cells acting as 'sponges' of Gd3+ ions." Contrast media & molecular imaging **1**(1): 23-29.

Caldwell, MA, He, X and Svendsen, CN (2005). "5-Bromo-2'-deoxyuridine is selectively toxic to neuronal precursors in vitro." The European journal of neuroscience **22**(11): 2965-2970.

Caravan, P, Farrar, CT, Frullano, L and Uppal, R (2009). "Influence of molecular parameters and increasing magnetic field strength on relaxivity of gadolinium- and manganese-based T1 contrast agents." Contrast Media Mol Imaging **4**(2): 89-100.

Carmichael, ST, Archibeque, I, Luke, L, Nolan, T, Momiy, J and Li, S (2005). "Growth-associated gene expression after stroke: evidence for a growth-promoting region in peri-infarct cortex." Exp Neurol **193**(2): 291-311.

Carmichael, ST, Wei, L, Rovainen, CM and Woolsey, TA (2001). "New patterns of intracortical projections after focal cortical stroke." Neurobiol Dis **8**(5): 910-922.

Castanheira, P, Torquetti, LT, Magalhas, DR, Nehemy, MB and Goes, AM (2009). "DAPI diffusion after intravitreal injection of mesenchymal stem cells in the injured retina of rats." Cell Transplant **18**(4): 423-431.

Chen, G, Hu, YR, Wan, H, Xia, L, Li, JH, Yang, F, Qu, X, Wang, SG and Wang, ZC (2010). "Functional recovery following traumatic spinal cord injury mediated by a unique polymer scaffold seeded with neural stem cells and Schwann cells." Chin Med J (Engl) **123**(17): 2424-2431.

Chen, LX, Ma, SM, Zhang, P, Fan, ZC, Xiong, M, Cheng, GQ, Yang, Y, Qiu, ZL, Zhou, WH and Li, J (2015). "Neuroprotective effects of oligodendrocyte progenitor cell transplantation in premature rat brain following hypoxic-ischemic injury." PLoS One **10**(3): e0115997.

Chen, MY, Hoffer, A, Morrison, PF, Hamilton, JF, Hughes, J, Schlageter, KS, Lee, J, Kelly, BR and Oldfield, EH (2005). "Surface properties, more than size, limiting convective distribution of virus-sized particles and viruses in the central nervous system." J Neurosurg **103**(2): 311-319.

Chen, YI, Brownell, AL, Galpern, W, Isacson, O, Bogdanov, M, Beal, MF, Livni, E, Rosen, BR and Jenkins, BG (1999). "Detection of dopaminergic cell loss and neural transplantation using pharmacological MRI, PET and behavioral assessment." Neuroreport **10**(14): 2881-2886.

Chung, YL, El Akabawy, G, So, PW, Solanky, BS, Leach, MO and Modo, M (2013). "Profiling metabolite changes in the neuronal differentiation of human striatal neural stem cells using 1H-magnetic resonance spectroscopy." Neuroreport **24**(18): 1035-1040.

Cifu, DX and Stewart, DG (1999). "Factors affecting functional outcome after stroke: A critical review of rehabilitation interventions." Archives of Physical Medicine and Rehabilitation **80**(5): S35-S39.

Ciofani, G, Raffa, V, Pizzorusso, T, Menciassi, A and Dario, P (2008). "Characterization of an alginate-based drug delivery system for neurological applications." Med Eng Phys **30**(7): 848-855.

Corsi, DM, Platas-Iglesias, C, Bekkum, Hv and Peters, JA (2001). "Determination of paramagnetic lanthanide(III) concentrations from bulk magnetic susceptibility shifts in NMR spectra." Magnetic Resonance in Chemistry **39**(11): 723-726.

Cramer, SC and Chopp, M (2000). "Recovery recapitulates ontogeny." Trends in Neurosciences **23**(6): 265-271.

Dabbousi, BO, Rodriguez-Viejo, J, Mikulec, FV, Heine, JR, Mattoussi, H, Ober, R, Jensen, KF and Bawendi, MG (1997). "(CdSe)ZnS Core,àíShell Quantum Dots:,Äâ Synthesis and Characterization of a Size Series of Highly Luminescent Nanocrystallites." The Journal of Physical Chemistry B **101**(46): 9463-9475.

Daniel, MC and Astruc, D (2004). "Gold nanoparticles: assembly, supramolecular chemistry, quantum-size-related properties, and applications toward biology, catalysis, and nanotechnology." Chemical reviews **104**(1): 293-346.

Deddens, LH, van Tilborg, GA, van der Toorn, A, de Vries, HE and Dijkhuizen, RM (2013). "PECAM-1-targeted micron-sized particles of iron oxide as MRI contrast agent for detection of vascular remodeling after cerebral ischemia." Contrast Media Mol Imaging **8**(5): 393-401.

Delli Castelli, D, Terreno, E and Aime, S (2011). "Yb(III)-HPDO3A: a dual pH- and temperature-responsive CEST agent." Angew Chem Int Ed Engl **50**(8): 1798-1800.

Detante, O, Valable, S, de Fraipont, F, Grillon, E, Barbier, EL, Moisan, A, Arnaud, J, Moriscot, C, Segebarth, C, Hommel, M, Remy, C and Richard, MJ (2012). "Magnetic resonance imaging and fluorescence labeling of clinical-grade mesenchymal stem cells without impacting their phenotype: study in a rat model of stroke." Stem cells translational medicine **1**(4): 333-341.

Di Corato, R, Gazeau, F, Le Visage, C, Fayol, D, Levitz, P, Lux, F, Letourneur, D, Luciani, N, Tillement, O and Wilhelm, C (2013). "High-Resolution Cellular MRI: Gadolinium and Iron Oxide Nanoparticles for in-Depth Dual-Cell Imaging of Engineered Tissue Constructs." ACS Nano **7**(9): 7500-7512.

Di Gregorio, E, Ferrauto, G, Gianolio, E and Aime, S (2013). "Gd loading by hypotonic swelling: an efficient and safe route for cellular labeling." Contrast Media Mol Imaging **8**(6): 475-486.

Dirnagl, U (2006). "Bench to bedside: the quest for quality in experimental stroke research." J Cereb Blood Flow Metab **26**(12): 1465-1478.

Dixon, WT, Ren, J, Lubag, AJ, Ratnakar, J, Vinogradov, E, Hancu, I, Lenkinski, RE and Sherry, AD (2010). "A concentration-independent method to measure exchange rates in PARACEST agents." Magn Reson Med **63**(3): 625-632.

Dobrossy, M, Busse, M, Piroth, T, Rosser, A, Dunnett, S and Nikkhah, G (2010). "Neurorehabilitation with neural transplantation." Neurorehabilitation and neural repair **24**(8): 692-701.

Durand, RE and Olive, PL (1982). "Cytotoxicity, Mutagenicity and DNA damage by Hoechst 33342." The journal of histochemistry and cytochemistry : official journal of the Histochemistry Society **30**(2): 111-116.

El Akabawy, G, Martinez-Medina, L, Jeffries, AR, Price, J and Modo, M (2011). "Purmorphamine increases DARPP-32 differentiation in human striatal neural stem cells through the hedgehog pathway." Stem Cells Dev.

El-Akabawy, G, Rattray, I, Johansson, SM, Gale, R, Bates, G and Modo, M (2012). "Implantation of undifferentiated and pre-differentiated human neural stem cells in the R6/2 transgenic mouse model of Huntington's disease." BMC Neurosci **13**: 97.

Elmadbouh, I, Chen, Y, Louedec, L, Silberman, S, Pouzet, B, Meilhac, O and Michel, JB (2005). "Mesothelial cell transplantation in the infarct scar induces neovascularization and improves heart function." Cardiovasc Res **68**(2): 307-317.

Eppendorf, A (2006). Multiporator Basic Applications Manual. Hamburg.

Evbuomwan, OM, Merritt, ME, Kiefer, GE and Dean Sherry, A (2012). "Nanoparticle-based PARACEST agents: the quenching effect of silica nanoparticles on the CEST signal from surface-conjugated chelates." Contrast Media Mol Imaging **7**(1): 19-25.

Fan, Y, Shen, F, Frenzel, T, Zhu, W, Ye, J, Liu, J, Chen, Y, Su, H, Young, WL and Yang, GY (2010). "Endothelial progenitor cell transplantation improves long-term stroke outcome in mice." Ann Neurol **67**(4): 488-497.

Ferrauto, G, Castelli, DD, Terreno, E and Aime, S (2012). "In vivo MRI visualization of different cell populations labeled with PARACEST agents." Magnetic resonance in medicine : official journal of the Society of Magnetic Resonance in Medicine / Society of Magnetic Resonance in Medicine.

Flament, J, Geffroy, F, Medina, C, Robic, C, Mayer, JF, Meriaux, S, Valette, J, Robert, P, Port, M, Le Bihan, D, Lethimonnier, F and Boumezbeur, F (2013). "In vivo CEST MR imaging of U87 mice brain tumor angiogenesis using targeted LipoCEST contrast agent at 7 T." Magn Reson Med **69**(1): 179-187.

Gheber, LA and Edidin, M (1999). "A model for membrane patchiness: lateral diffusion in the presence of barriers and vesicle traffic." Biophysical journal **77**(6): 3163-3175.

Ghysen, A, Dambly-Chaudiere, C, Jan, LY and Jan, YN (1993). "Cell interactions and gene interactions in peripheral neurogenesis." Genes Dev **7**(5): 723-733.

Gildehaus, FJ, Haasters, F, Drosse, I, Wagner, E, Zach, C, Mutschler, W, Cumming, P, Bartenstein, P and Schieker, M (2011). "Impact of indium-111 oxine labelling on viability of human mesenchymal stem cells in vitro, and 3D cell-tracking using SPECT/CT in vivo." Mol Imaging Biol **13**(6): 1204-1214.

Giljohann, DA, Seferos, DS, Patel, PC, Millstone, JE, Rosi, NL and Mirkin, CA (2007). "Oligonucleotide loading determines cellular uptake of DNA-modified gold nanoparticles." Nano letters **7**(12): 3818-3821.

Gillies, RJ, Barry, JA and Ross, BD (1994). "In vitro and in vivo 13C and 31P NMR analyses of phosphocholine metabolism in rat glioma cells." Magn Reson Med **32**(3): 310-318.

Gladstone, DJ, Black, SE, Hakim, AM, Heart and Stroke Foundation of Ontario Centre of Excellence in Stroke, R (2002). "Toward wisdom from failure: lessons from neuroprotective stroke trials and new therapeutic directions." Stroke **33**(8): 2123-2136.

Gobbel, GT, Kondziolka, D, Fellows-Mayle, W and Uram, M (2010). "Cellular transplantation for the nervous system: impact of time after preparation on cell viability and survival." Journal of neurosurgery **113**(3): 666-672.

Gobbel, GT, Kondziolka, D, Fellows-Mayle, W and Uram, M (2010). "Manual vs automated delivery of cells for transplantation: accuracy, reproducibility, and impact on viability." Neurosurgery **67**(6): 1662-1668; discussion 1668.

Gomez, N, Lu, Y, Chen, S and Schmidt, CE (2007). "Immobilized nerve growth factor and microtopography have distinct effects on polarization versus axon elongation in hippocampal cells in culture." Biomaterials **28**(2): 271-284.

Grabowski, M, Johansson, BB and Brundin, P (1995). "Neocortical grafts placed in the infarcted brain of adult rats: few or no efferent fibers grow from transplant to host." Exp Neurol **134**(2): 273-276.

Guenoun, J, Ruggiero, A, Doeswijk, G, Janssens, RC, Koning, GA, Kotek, G, Krestin, GP and Bernsen, MR (2013). "In vivo quantitative assessment of cell viability of gadolinium or iron-labeled cells using MRI and bioluminescence imaging." Contrast Media Mol Imaging **8**(2): 165-174.

Guzman, R, Bliss, T, De Los Angeles, A, Moseley, M, Palmer, T and Steinberg, G (2008). "Neural progenitor cells transplanted into the uninjured brain undergo targeted migration after stroke onset." J Neurosci Res **86**(4): 873-882.

Hasenberg, A, Hasenberg, M, Mann, L, Neumann, F, Borkenstein, L, Stecher, M, Kraus, A, Engel, DR, Klingberg, A, Seddigh, P, Abdullah, Z, Klebow, S, Engelmann, S, Reinhold, A, Brandau, S, Seeling, M, Waisman, A, Schraven, B, Gothert, JR, Nimmerjahn, F and Gunzer, M (2015). "Catchup: a mouse model for imaging-based tracking and modulation of neutrophil granulocytes." Nat Methods **12**(5): 445-452.

Health, USNIo. "Registry of Clinical Studies of Human participants." Retrieved 8/6/2014, from http://www.clinicaltrials.gov.

Heinrich, C, Blum, R, Gascon, S, Masserdotti, G, Tripathi, P, Sanchez, R, Tiedt, S, Schroeder, T, Gotz, M and Berninger, B (2010). "Directing astroglia from the cerebral cortex into subtype specific functional neurons." PLoS Biol **8**(5): e1000373.

Helm, L (2010). "Optimization of gadolinium-based MRI contrast agents for high magnetic-field applications." Future Med Chem **2**(3): 385-396.

Helpern, JA, Dereski, MO, Knight, RA, Ordidge, RJ, Chopp, M and Qing, ZX (1993). "Histopathological correlations of nuclear magnetic resonance imaging parameters in experimental cerebral ischemia." Magn Reson Imaging **11**(2): 241-246.

Hemmrich, K, Meersch, M, von Heimburg, D and Pallua, N (2006). "Applicability of the dyes CFSE, CM-DiI and PKH26 for tracking of human preadipocytes to evaluate adipose tissue engineering." Cells, tissues, organs **184**(3-4): 117-127.

Hicks, AU, Hewlett, K, Windle, V, Chernenko, G, Ploughman, M, Jolkkonen, J, Weiss, S and Corbett, D (2007). "Enriched environment enhances transplanted subventricular zone stem cell migration and functional recovery after stroke." Neuroscience **146**(1): 31-40.

Hoehn, M, Kustermann, E, Blunk, J, Wiedermann, D, Trapp, T, Wecker, S, Focking, M, Arnold, H, Hescheler, J, Fleischmann, BK, Schwindt, W and Buhrle, C (2002). "Monitoring of implanted stem cell migration in vivo: a highly resolved in vivo magnetic resonance imaging investigation of experimental stroke in rat." Proc Natl Acad Sci U S A **99**(25): 16267-16272.

Horisberger, M and Rosset, J (1977). "Colloidal gold, a useful marker for transmission and scanning electron microscopy." Journal of Histochemistry & Cytochemistry **25**(4): 295-305.

Hoshino, A, Hanada, S and Yamamoto, K (2011). "Toxicity of nanocrystal quantum dots: the relevance of surface modifications." Archives of toxicology.

Hruban, RH, Long, PP, Perlman, EJ, Hutchins, GM, Baumgartner, WA, Baughman, KL and Griffin, CA (1993). "Fluorescence in situ hybridization for the Y-chromosome can be used to detect cells of recipient origin in allografted hearts following cardiac transplantation." Am J Pathol **142**(4): 975-980.

Hua, J, Jones, CK, Blakeley, J, Smith, SA, van Zijl, PC and Zhou, J (2007). "Quantitative description of the asymmetry in magnetization transfer effects around the water resonance in the human brain." Magn Reson Med **58**(4): 786-793.

Huang, W-Y, Aramburu, J, Douglas, PS and Izumo, S (2000). "Transgenic expression of green fluorescence protein can cause dilated cardiomyopathy." Nat Med **6**(5): 482-483.

Hubbard, KS, Gut, IM, Scheeler, SM, Lyman, ME and McNutt, PM (2012). "Compatibility of SYTO 13 and Hoechst 33342 for longitudinal imaging of neuron viability and cell death." BMC Res Notes **5**: 437.

Hunt, D, Coffin, RS, Prinjha, RK, Campbell, G and Anderson, PN (2003). "Nogo-A expression in the intact and injured nervous system." Mol Cell Neurosci **24**(4): 1083-1102.

Hyun, H, Won, YW, Kim, KM, Lee, J, Lee, M and Kim, YH (2010). "Therapeutic effects of a reducible poly (oligo-d-arginine) carrier with the heme oxygenase-1 gene in the treatment of hypoxic-ischemic brain injury." Biomaterials.

Idee, JM, Port, M, Robic, C, Medina, C, Sabatou, M and Corot, C (2009). "Role of thermodynamic and kinetic parameters in gadolinium chelate stability." J Magn Reson Imaging **30**(6): 1249-1258.

Inoue, Y, Kiryu, S, Izawa, K, Watanabe, M, Tojo, A and Ohtomo, K (2009). "Comparison of subcutaneous and intraperitoneal injection of D-luciferin for in vivo bioluminescence imaging." Eur J Nucl Med Mol Imaging **36**(5): 771-779.

Iordanova, B and Ahrens, ET (2012). "In vivo magnetic resonance imaging of ferritin-based reporter visualizes native neuroblast migration." Neuroimage **59**(2): 1004-1012.

Ishikawa, H, Tajiri, N, Shinozuka, K, Vasconcellos, J, Kaneko, Y, Lee, HJ, Mimura, O, Dezawa, M, Kim, SU and Borlongan, CV (2013). "Vasculogenesis in experimental stroke after human cerebral endothelial cell transplantation." Stroke **44**(12): 3473-3481.

Iwashita, Y, Crang, AJ and Blakemore, WF (2000). "Redistribution of bisbenzimide Hoechst 33342 from transplanted cells to host cells." Neuroreport **11**(5): 1013-1016.

Iyer, M, Barrio, JR, Namavari, M, Bauer, E, Satyamurthy, N, Nguyen, K, Toyokuni, T, Phelps, ME, Herschman, HR and Gambhir, SS (2001). "8-[18F]Fluoropenciclovir: an improved reporter probe for imaging HSV1-tk reporter gene expression in vivo using PET." J Nucl Med **42**(1): 96-105.

Jendelova, P, Herynek, V, DeCroos, J, Glogarova, K, Andersson, B, Hajek, M and Sykova, E (2003). "Imaging the fate of implanted bone marrow stromal cells labeled with superparamagnetic nanoparticles." Magn Reson Med **50**(4): 767-776.

Jiang, Q, Zhang, ZG, Ding, GL, Silver, B, Zhang, L, Meng, H, Lu, M, Pourabdillah-Nejed-D, S, Wang, L, Savant-Bhonsale, S, Li, L, Bagher-Ebadian, H, Hu, J, Arbab, AS, Vanguri, P, Ewing, JR, Ledbetter, KA and Chopp, M (2006). "MRI detects white matter reorganization after neural progenitor cell treatment of stroke." Neuroimage **32**(3): 1080-1089.

Johansson, S, Price, J and Modo, M (2008). "Effect of inflammatory cytokines on major histocompatibility complex expression and differentiation of human neural stem/progenitor cells." Stem Cells **26**(9): 2444-2454.

Kallur, T, Farr, TD, Bohm-Sturm, P, Kokaia, Z and Hoehn, M (2011). "Spatio-temporal dynamics, differentiation and viability of human neural stem cells after implantation into neonatal rat brain." Eur J Neurosci **34**(3): 382-393.

Kanal, E, Maravilla, K and Rowley, HA (2014). "Gadolinium Contrast Agents for CNS Imaging: Current Concepts and Clinical Evidence." AJNR Am J Neuroradiol.

Karfeld-Sulzer, LS, Waters, EA, Kohlmeir, EK, Kissler, H, Zhang, X, Kaufman, DB, Barron, AE and Meade, TJ (2011). "Protein polymer MRI contrast agents: Longitudinal analysis of biomaterials in vivo." Magn Reson Med **65**(1): 220-228.

Kawaguchi, K, Katsuyama, Y, Kikkawa, S, Setsu, T and Terashima, T (2010). "PKH26 is an excellent retrograde and anterograde fluorescent tracer characterized by a small injection site and strong fluorescence emission." Archives of histology and cytology **73**(2): 65-72.

Kerr, JN and Denk, W (2008). "Imaging in vivo: watching the brain in action." Nat Rev Neurosci **9**(3): 195-205.

Kidwell, CS, Liebeskind, DS, Starkman, S and Saver, JL (2001). "Trends in acute ischemic stroke trials through the 20th century." Stroke **32**(6): 1349-1359.

Kim, JI, Chun, C, Kim, B, Hong, JM, Cho, JK, Lee, SH and Song, SC (2012). "Thermosensitive/magnetic poly(organophosphazene) hydrogel as a long-term magnetic resonance contrast platform." Biomaterials **33**(1): 218-224.

Kim, SH, Jeong, JH, Kim, TI, Kim, SW and Bull, DA (2009). "VEGF siRNA delivery system using arginine-grafted bioreducible poly(disulfide amine)." Mol Pharm **6**(3): 718-726.

Kim, SU (2004). "Human neural stem cells genetically modified for brain repair in neurological disorders." Neuropathology **24**(3): 159-171.

Kim, TI, Lee, M and Kim, SW (2010). "A guanidinylated bioreducible polymer with high nuclear localization ability for gene delivery systems." Biomaterials **31**(7): 1798-1804.

Klose, D, Laprais, M, Leroux, V, Siepmann, F, Deprez, B, Bordet, R and Siepmann, J (2009). "Fenofibrate-loaded PLGA microparticles: effects on ischemic stroke." Eur J Pharm Sci **37**(1): 43-52.

Knight, RA, Dereski, MO, Helpern, JA, Ordidge, RJ and Chopp, M (1994). "Magnetic resonance imaging assessment of evolving focal cerebral ischemia. Comparison with histopathology in rats." Stroke **25**(6): 1252-1261; discussion 1261-1252.

Kok, MB, Hak, S, Mulder, WJ, van der Schaft, DW, Strijkers, GJ and Nicolay, K (2009). "Cellular compartmentalization of internalized paramagnetic liposomes strongly influences both T1 and T2 relaxivity." Magn Reson Med **61**(5): 1022-1032.

Kondziolka, D, Steinberg, GK, Wechsler, L, Meltzer, CC, Elder, E, Gebel, J, Decesare, S, Jovin, T, Zafonte, R, Lebowitz, J, Flickinger, JC, Tong, D, Marks, MP, Jamieson, C, Luu, D, Bell-Stephens, T and Teraoka, J (2005). "Neurotransplantation for patients with subcortical motor stroke: a phase 2 randomized trial." Journal of neurosurgery **103**(1): 38-45.

Kondziolka, D, Wechsler, L, Goldstein, S, Meltzer, C, Thulborn, KR, Gebel, J, Jannetta, P, DeCesare, S, Elder, EM, McGrogan, M, Reitman, MA and Bynum, L (2000). "Transplantation of cultured human neuronal cells for patients with stroke." Neurology **55**(4): 565-569.

Kozai, TD, Vazquez, AL, Weaver, CL, Kim, SG and Cui, XT (2012). "In vivo two-photon microscopy reveals immediate microglial reaction to implantation of microelectrode through extension of processes." J Neural Eng **9**(6): 066001.

Krupinski, J, Kaluza, J, Kumar, P, Kumar, S and Wang, JM (1994). "Role of angiogenesis in patients with cerebral ischemic stroke." Stroke **25**(9): 1794-1798.

Kuo, CW, Chueh, DY, Singh, N, Chien, FC and Chen, P (2011). "Targeted Nuclear Delivery using Peptide-Coated Quantum Dots." Bioconjugate chemistry **22**(6): 1073-1080.

Kurozumi, K, Nakamura, K, Tamiya, T, Kawano, Y, Ishii, K, Kobune, M, Hirai, S, Uchida, H, Sasaki, K, Ito, Y, Kato, K, Honmou, O, Houkin, K, Date, I and Hamada, H (2005). "Mesenchymal stem cells that produce neurotrophic factors reduce ischemic damage in the rat middle cerebral artery occlusion model." Mol Ther **11**(1): 96-104.

Kurtoglu, YE, Navath, RS, Wang, B, Kannan, S, Romero, R and Kannan, RM (2009). "Poly(amidoamine) dendrimer-drug conjugates with disulfide linkages for intracellular drug delivery." Biomaterials **30**(11): 2112-2121.

Lam, HJ, Patel, S, Wang, A, Chu, J and Li, S (2010). "In vitro regulation of neural differentiation and axon growth by growth factors and bioactive nanofibers." Tissue Eng Part A **16**(8): 2641-2648.

Lassailly, F, Griessinger, E and Bonnet, D (2010). ""Microenvironmental contaminations" induced by fluorescent lipophilic dyes used for non-invasive in vitro and in vivo cell tracking." Blood.

Last'ovicka, J, Budinsky, V, Spisek, R and Bartunkova, J (2009). "Assessment of lymphocyte proliferation: CFSE kills dividing cells and modulates expression of activation markers." Cell Immunol **256**(1-2): 79-85.

Lee, HJ, Lim, IJ, Lee, MC and Kim, SU (2010). "Human neural stem cells genetically modified to overexpress brain-derived neurotrophic factor promote functional recovery and neuroprotection in a mouse stroke model." J Neurosci Res.

Lehner, B, Sandner, B, Marschallinger, J, Lehner, C, Furtner, T, Couillard-Despres, S, Rivera, FJ, Brockhoff, G, Bauer, HC, Weidner, N and Aigner, L (2011). "The dark side of BrdU in neural stem cell biology: detrimental effects on cell cycle, differentiation and survival." Cell and tissue research.

Leuner, B, Glasper, ER and Gould, E (2009). "Thymidine analog methods for studies of adult neurogenesis are not equally sensitive." J Comp Neurol **517**(2): 123-133.

Leventhal, C, Rafii, S, Rafii, D, Shahar, A and Goldman, SA (1999). "Endothelial trophic support of neuronal production and recruitment from the adult mammalian subependyma." Mol Cell Neurosci **13**(6): 450-464.

Lewis, CM, Graves, SA, Hernandez, R, Valdovinos, HF, Barnhart, TE, Cai, W, Meyerand, ME, Nickles, RJ and Suzuki, M (2015). "(5)(2)Mn production for PET/MRI tracking of human stem cells expressing divalent metal transporter 1 (DMT1)." Theranostics **5**(3): 227-239.

Li, AX, Hudson, RH, Barrett, JW, Jones, CK, Pasternak, SH and Bartha, R (2008). "Four-pool modeling of proton exchange processes in biological systems in the presence of MRI-paramagnetic chemical exchange saturation transfer (PARACEST) agents." Magn Reson Med **60**(5): 1197-1206.

Li, S, Overman, JJ, Katsman, D, Kozlov, SV, Donnelly, CJ, Twiss, JL, Giger, RJ, Coppola, G, Geschwind, DH and Carmichael, ST (2010). "An age-related sprouting transcriptome provides molecular control of axonal sprouting after stroke." Nat Neurosci **13**(12): 1496-1504.

Li, X, Dancausse, H, Grijalva, I, Oliveira, M and Levi, AD (2003). "Labeling Schwann cells with CFSE-an in vitro and in vivo study." J Neurosci Methods **125**(1-2): 83-91.

Liauw, J, Hoang, S, Choi, M, Eroglu, C, Sun, GH, Percy, M, Wildman-Tobriner, B, Bliss, T, Guzman, RG, Barres, BA and Steinberg, GK (2008). "Thrombospondins 1 and 2 are necessary for synaptic plasticity and functional recovery after stroke." J Cereb Blood Flow Metab **28**(10): 1722-1732.

Lim, ST, Airavaara, M and Harvey, BK (2010). "Viral vectors for neurotrophic factor delivery: a gene therapy approach for neurodegenerative diseases of the CNS." Pharmacol Res **61**(1): 14-26.

Lipton, P (1999). "Ischemic cell death in brain neurons." Physiol Rev **79**(4): 1431-1568.

Liu, C, Lin, N, Wu, B and Qiu, Y (2009). "Neuroprotective effect of memantine combined with topiramate in hypoxic-ischemic brain injury." Brain Res **1282**: 173-182.

Liu, SJ, Zou, Y, Belegu, V, Lv, LY, Lin, N, Wang, TY, McDonald, JW, Zhou, X, Xia, QJ and Wang, TH (2014). "Co-grafting of neural stem cells with olfactory en sheathing cells promotes neuronal restoration in traumatic brain injury with an anti-inflammatory mechanism." J Neuroinflammation **11**: 66.

Loewenbruck, KF, Fuchs, B, Hermann, A, Brandt, M, Werner, A, Kirsch, M, Schwarz, S, Schwarz, J, Schiller, J and Storch, A (2011). "Proton MR spectroscopy of neural stem cells: does the proton-NMR peak at 1.28 ppm function as a biomarker for cell type or state?" Rejuvenation Res **14**(4): 371-381.

Longa, EZ, Weinstein, PR, Carlson, S and Cummins, R (1989). "Reversible middle cerebral artery occlusion without craniectomy in rats." Stroke **20**(1): 84-91.

Lopez-Valdes, HE, Clarkson, AN, Ao, Y, Charles, AC, Carmichael, ST, Sofroniew, MV and Brennan, KC (2014). "Memantine enhances recovery from stroke." Stroke **45**(7): 2093-2100.

Luk, YO, Chen, WY, Wong, WJ, Hu, HH, Hsu, LC, Chern, CM, Huang, KJ and Law, SL (2004). "Treatment of focal cerebral ischemia with liposomal nerve growth factor." Drug Deliv **11**(5): 319-324.

Manganas, LN, Zhang, X, Li, Y, Hazel, RD, Smith, SD, Wagshul, ME, Henn, F, Benveniste, H, Djuric, PM, Enikolopov, G and Maletic-Savatic, M (2007). "Magnetic resonance spectroscopy identifies neural progenitor cells in the live human brain." Science **318**(5852): 980-985.

Marchal, G, Beaudouin, V, Rioux, P, de la Sayette, V, Le Doze, F, Viader, F, Derlon, JM and Baron, JC (1996). "Prolonged persistence of substantial volumes of potentially viable brain tissue after stroke: a correlative PET-CT study with voxel-based data analysis." Stroke **27**(4): 599-606.

Martin, A, Gomez-Vallejo, V, San Sebastian, E, Padro, D, Markuerkiaga, I, Llarena, I and Llop, J (2013). "In vivo imaging of dopaminergic neurotransmission after transient focal ischemia in rats." J Cereb Blood Flow Metab **33**(2): 244-252.

Martinez-Serrano, A, Villa, A, Navarro, B, Rubio, FJ and Bueno, C (2000). "Human neural progenitor cells: better blue than green?" Nat Med **6**(5): 483-484.

Marzesco, AM, Janich, P, Wilsch-Brauninger, M, Dubreuil, V, Langenfeld, K, Corbeil, D and Huttner, WB (2005). "Release of extracellular membrane particles carrying the stem cell marker prominin-1 (CD133) from neural progenitors and other epithelial cells." J Cell Sci **118**(Pt 13): 2849-2858.

Masamoto, K, Takuwa, H, Tomita, Y, Toriumi, H, Unekawa, M, Taniguchi, J, Kawaguchi, H, Itoh, Y, Suzuki, N, Ito, H and Kanno, I (2013). "Hypoxia-induced cerebral angiogenesis in mouse cortex with two-photon microscopy." Adv Exp Med Biol **789**: 15-20.

Massensini, AR, Medberry, CJ, Ling, W, Nicholls, FJ, Badylak, SF and Modo, M (2014). "Delivery of biomaterials to a stroke cavity – Intracerebral stereotactic injection and drainage based on magnetic resonance imaging." (Submitted).

May, DA and Pennington, DJ (2000). "Effect of gadolinium concentration on renal signal intensity: An in vitro study with a saline bag model." Radiology **216**(1): 232-236.

McVicar, N, Li, AX, Suchy, M, Hudson, RH, Menon, RS and Bartha, R (2013). "Simultaneous in vivo pH and temperature mapping using a PARACEST-MRI contrast agent." Magn Reson Med **70**(4): 1016-1025.

Minger, SL, Ekonomou, A, Carta, EM, Chinoy, A, Perry, RH and Ballard, CG (2007). "Endogenous neurogenesis in the human brain following cerebral infarction." Regen Med **2**(1): 69-74.

Modo, M (2009). "Long-term survival and serial assessment of stroke damage and recovery - practical and methodological considerations." J Exp Stroke Transl Med **2**(2): 52-68.

Modo, M, Beech, JS, Meade, TJ, Williams, SC and Price, J (2009). "A chronic 1 year assessment of MRI contrast agent-labelled neural stem cell transplants in stroke." Neuroimage **47 Suppl 2**: T133-142.

Modo, M, Kolosnjaj-Tabi, J, Nicholls, F, Ling, W, Wilhelm, C, Debarge, O, Gazeau, F and Clement, O (2013). "Considerations for the clinical use of contrast agents for cellular MRI in regenerative medicine." Contrast Media Mol Imaging **8**(6): 439-455.

Modo, M, Mellodew, K, Cash, D, Fraser, SE, Meade, TJ, Price, J and Williams, SC (2004). "Mapping transplanted stem cell migration after a stroke: a serial, in vivo magnetic resonance imaging study." Neuroimage **21**(1): 311-317.

Modo, M, Stroemer, RP, Tang, E, Veizovic, T, Sowniski, P and Hodges, H (2000). "Neurological sequelae and long-term behavioural assessment of rats with transient middle cerebral artery occlusion." J Neurosci Methods **104**(1): 99-109.

Molcanyi, M, Bosche, B, Kraitsy, K, Patz, S, Zivcak, J, Riess, P, Majdoub, FE, Hescheler, J, Goldbrunner, R and Schafer, U (2013). "Pitfalls and fallacies interfering with correct identification of embryonic stem cells implanted into the brain after experimental traumatic injury." Journal of neuroscience methods **215**(1): 60-70.

Moubarik, C, Guillet, B, Youssef, B, Codaccioni, JL, Piercecchi, MD, Sabatier, F, Lionel, P, Dou, L, Foucault-Bertaud, A, Velly, L, Dignat-George, F and Pisano, P (2011). "Transplanted late outgrowth endothelial progenitor cells as cell therapy product for stroke." Stem Cell Rev **7**(1): 208-220.

Moustafa, RR and Baron, JC (2008). "Pathophysiology of ischaemic stroke: insights from imaging, and implications for therapy and drug discovery." Br J Pharmacol **153 Suppl 1**: S44-54.

Murray, CJ, Vos, T, Lozano, R, Naghavi, M, Flaxman, AD, Michaud, C, Ezzati, M, Shibuya, K, Salomon, JA, Abdalla, S, Aboyans, V, Abraham, J, Ackerman, I, Aggarwal, R, Ahn, SY, Ali, MK, Alvarado, M, Anderson, HR, Anderson, LM, Andrews, KG, Atkinson, C, Baddour, LM, Bahalim, AN, Barker-Collo, S, Barrero, LH, Bartels, DH, Basanez, MG, Baxter, A, Bell, ML, Benjamin, EJ, Bennett, D, Bernabe, E, Bhalla, K, Bhandari, B, Bikbov, B, Bin Abdulhak, A, Birbeck, G, Black, JA, Blencowe, H, Blore, JD, Blyth, F, Bolliger, I, Bonaventure, A, Boufous, S, Bourne, R, Boussinesq, M, Braithwaite, T, Brayne, C, Bridgett, L, Brooker, S, Brooks, P, Brugha, TS, Bryan-Hancock, C, Bucello, C, Buchbinder, R, Buckle, G, Budke, CM, Burch, M, Burney, P, Burstein, R, Calabria, B, Campbell, B, Canter, CE, Carabin, H, Carapetis, J, Carmona, L, Cella, C, Charlson, F, Chen, H, Cheng, AT, Chou, D, Chugh, SS, Coffeng, LE, Colan, SD, Colquhoun, S, Colson, KE, Condon, J, Connor, MD, Cooper, LT, Corriere, M, Cortinovis, M, de Vaccaro, KC, Couser, W, Cowie, BC, Criqui, MH, Cross, M, Dabhadkar, KC, Dahiya, M, Dahodwala, N, Damsere-Derry, J, Danaei, G, Davis, A, De Leo, D, Degenhardt, L, Dellavalle, R, Delossantos, A, Denenberg, J, Derrett, S, Des Jarlais, DC, Dharmaratne, SD, Dherani, M, Diaz-Torne, C, Dolk, H, Dorsey, ER, Driscoll, T, Duber, H, Ebel, B, Edmond, K, Elbaz, A, Ali, SE, Erskine, H, Erwin, PJ, Espindola, P, Ewoigbokhan, SE, Farzadfar, F, Feigin, V, Felson, DT, Ferrari, A, Ferri, CP, Fevre, EM, Finucane, MM, Flaxman, S, Flood, L, Foreman, K, Forouzanfar, MH, Fowkes, FG, Fransen, M, Freeman, MK, Gabbe, BJ, Gabriel, SE, Gakidou, E, Ganatra, HA, Garcia, B, Gaspari, F, Gillum, RF, Gmel, G, Gonzalez-Medina, D, Gosselin, R, Grainger, R, Grant, B, Groeger, J, Guillemin, F, Gunnell, D, Gupta, R, Haagsma, J, Hagan, H, Halasa, YA, Hall, W, Haring, D, Haro, JM, Harrison, JE, Havmoeller, R, Hay, RJ, Higashi, H, Hill, C, Hoen, B, Hoffman, H, Hotez, PJ, Hoy, D, Huang, JJ, Ibeanusi, SE, Jacobsen, KH, James, SL, Jarvis, D, Jasrasaria, R, Jayaraman, S, Johns, N, Jonas, JB, Karthikeyan, G, Kassebaum, N, Kawakami, N, Keren, A, Khoo, JP, King, CH, Knowlton, LM, Kobusingye, O, Koranteng, A, Krishnamurthi, R, Laden, F, Lalloo, R, Laslett, LL, Lathlean, T, Leasher, JL, Lee, YY, Leigh, J, Levinson, D, Lim, SS, Limb, E, Lin, JK, Lipnick, M, Lipshultz, SE, Liu, W, Loane, M, Ohno, SL, Lyons, R, Mabweijano, J, MacIntyre, MF, Malekzadeh, R, Mallinger, L, Manivannan, S, Marcenes, W, March, L, Margolis, DJ, Marks, GB, Marks, R, Matsumori, A, Matzopoulos, R, Mayosi, BM, McAnulty, JH, McDermott, MM, McGill, N, McGrath, J, Medina-Mora, ME, Meltzer, M, Mensah, GA, Merriman, TR, Meyer, AC, Miglioli, V, Miller, M, Miller, TR, Mitchell, PB, Mock, C, Mocumbi, AO, Moffitt, TE, Mokdad, AA, Monasta, L, Montico, M, Moradi-Lakeh, M, Moran, A, Morawska, L, Mori, R, Murdoch, ME, Mwaniki, MK, Naidoo, K, Nair, MN, Naldi, L, Narayan, KM, Nelson, PK, Nelson, RG, Nevitt, MC, Newton, CR, Nolte, S, Norman, P, Norman, R, O'Donnell, M, O'Hanlon, S, Olives, C, Omer, SB, Ortblad, K, Osborne, R, Ozgediz, D, Page, A, Pahari, B, Pandian, JD, Rivero, AP, Patten, SB, Pearce, N, Padilla, RP, Perez-Ruiz, F, Perico, N, Pesudovs, K, Phillips, D, Phillips, MR, Pierce, K, Pion, S, Polanczyk, GV, Polinder, S, Pope, CA, 3rd, Popova, S, Porrini, E, Pourmalek, F, Prince, M, Pullan, RL, Ramaiah, KD, Ranganathan, D, Razavi, H, Regan, M, Rehm, JT, Rein, DB, Remuzzi, G, Richardson, K, Rivara, FP, Roberts, T, Robinson, C, De Leon, FR, Ronfani, L, Room, R, Rosenfeld, LC, Rushton, L, Sacco, RL, Saha, S, Sampson, U, Sanchez-Riera, L, Sanman, E, Schwebel, DC, Scott, JG, Segui-Gomez, M, Shahraz, S, Shepard, DS, Shin, H, Shivakoti, R, Singh, D, Singh, GM, Singh, JA, Singleton, J, Sleet, DA, Sliwa, K, Smith, E, Smith, JL, Stapelberg, NJ, Steer, A, Steiner, T, Stolk, WA, Stovner, LJ, Sudfeld, C, Syed, S, Tamburlini, G, Tavakkoli, M, Taylor, HR, Taylor, JA, Taylor, WJ, Thomas, B, Thomson, WM, Thurston, GD, Tleyjeh, IM, Tonelli, M, Towbin, JA, Truelsen, T, Tsilimbaris, MK, Ubeda, C, Undurraga, EA, van der Werf, MJ, van Os, J, Vavilala, MS, Venketasubramanian, N, Wang, M, Wang, W, Watt, K, Weatherall, DJ, Weinstock, MA, Weintraub, R, Weisskopf, MG, Weissman, MM, White, RA, Whiteford, H, Wiebe, N, Wiersma, ST, Wilkinson, JD, Williams, HC, Williams, SR, Witt, E, Wolfe, F, Woolf, AD, Wulf, S, Yeh, PH, Zaidi, AK, Zheng, ZJ, Zonies, D, Lopez, AD, AlMazroa, MA and Memish, ZA (2012). "Disability-adjusted life years (DALYs) for 291 diseases and injuries in 21

regions, 1990-2010: a systematic analysis for the Global Burden of Disease Study 2010." Lancet **380**(9859): 2197-2223.

Naumova, AV, Balu, N, Yarnykh, VL, Reinecke, H, Murry, CE and Yuan, C (2014). "Magnetic Resonance Imaging Tracking of Graft Survival in the Infarcted Heart: Iron Oxide Particles Versus Ferritin Overexpression Approach." J Cardiovasc Pharmacol Ther **19**(4): 358-367.

Oh, BJ, Oh, SH, Jin, SM, Suh, S, Bae, JC, Park, CG, Lee, MS, Lee, MK, Kim, JH and Kim, KW (2013). "Co-transplantation of bone marrow-derived endothelial progenitor cells improves revascularization and organization in islet grafts." Am J Transplant **13**(6): 1429-1440.

Olanow, CW (2004). "Manganese-induced parkinsonism and Parkinson's disease." Ann N Y Acad Sci **1012**: 209-223.

Olson, HE, Rooney, GE, Gross, L, Nesbitt, JJ, Galvin, KE, Knight, A, Chen, B, Yaszemski, MJ and Windebank, AJ (2009). "Neural stem cell- and Schwann cell-loaded biodegradable polymer scaffolds support axonal regeneration in the transected spinal cord." Tissue Eng Part A **15**(7): 1797-1805.

Onifer, SM, White, LA, Whittemore, SR and Holets, VR (1993). "In vitro labeling strategies for identifying primary neural tissue and a neuronal cell line after transplantation in the CNS." Cell transplantation **2**(2): 131-149.

Onuki, Y, Jacobs, I, Artemov, D and Kato, Y (2010). "Noninvasive visualization of in vivo release and intratumoral distribution of surrogate MR contrast agent using the dual MR contrast technique." Biomaterials **31**(27): 7132-7138.

Parish, CR (1999). "Fluorescent dyes for lymphocyte migration and proliferation studies." Immunol Cell Biol **77**(6): 499-508.

Park, KI, Teng, YD and Snyder, EY (2002). "The injured brain interacts reciprocally with neural stem cells supported by scaffolds to reconstitute lost tissue." Nat Biotechnol **20**(11): 1111-1117.

Pettersson, J, Lobov, S and Novikova, LN (2010). "Labeling of olfactory ensheathing glial cells with fluorescent tracers for neurotransplantation." Brain Res Bull **81**(1): 125-132.

Pollock, K, Stroemer, P, Patel, S, Stevanato, L, Hope, A, Miljan, E, Dong, Z, Hodges, H, Price, J and Sinden, JD (2006). "A conditionally immortal clonal stem cell line from human cortical neuroepithelium for the treatment of ischemic stroke." Experimental neurology **199**(1): 143-155.

Popovtzer, R, Agrawal, A, Kotov, NA, Popovtzer, A, Balter, J, Carey, TE and Kopelman, R (2008). "Targeted Gold Nanoparticles Enable Molecular CT Imaging of Cancer." Nano Letters **8**(12): 4593-4596.

Privalov, PL, Dragan, AI, Crane-Robinson, C, Breslauer, KJ, Remeta, DP and Minetti, CA (2007). "What drives proteins into the major or minor grooves of DNA?" J Mol Biol **365**(1): 1-9.

Quah, BJ and Parish, CR (2010). "The use of carboxyfluorescein diacetate succinimidyl ester (CFSE) to monitor lymphocyte proliferation." J Vis Exp(44).

Raya, JG, Dietrich, O, Horng, A, Weber, J, Reiser, MF and Glaser, C (2010). "T2 measurement in articular cartilage: impact of the fitting method on accuracy and precision at low SNR." Magn Reson Med **63**(1): 181-193.

Reddy, MK and Labhasetwar, V (2009). "Nanoparticle-mediated delivery of superoxide dismutase to the brain: an effective strategy to reduce ischemia-reperfusion injury." FASEB J **23**(5): 1384-1395.

Roberts, TJ, Price, J, Williams, SC and Modo, M (2007). "Pharmacological MRI of stem cell transplants in the 3-nitropropionic acid-damaged striatum." Neuroscience **144**(1): 100-109.

Robertson, PL, Du Bois, M, Bowman, PD and Goldstein, GW (1985). "Angiogenesis in developing rat brain: an in vivo and in vitro study." Brain Res **355**(2): 219-223.

Roffman, JL, Lipska, BK, Bertolino, A, Van Gelderen, P, Olson, AW, Khaing, ZZ and Weinberger, DR (2000). "Local and downstream effects of excitotoxic lesions in the rat medial prefrontal cortex on In vivo 1H-MRS signals." Neuropsychopharmacology **22**(4): 430-439.

Roine, T, Jeurissen, B, Perrone, D, Aelterman, J, Leemans, A, Philips, W and Sijbers, J (2014). "Isotropic non-white matter partial volume effects in constrained spherical deconvolution." Front Neuroinform **8**: 28.

Ross, BD, Hoang, TQ, Bluml, S, Dubowitz, D, Kopyov, OV, Jacques, DB, Lin, A, Seymour, K and Tan, J (1999). "In vivo magnetic resonance spectroscopy of human fetal neural transplants." NMR Biomed **12**(4): 221-236.

Rossignol, J, Boyer, C, LÈvËque, X, Fink, KD, Thinard, R, Blanchard, F, Dunbar, GL and Lescaudron, L (2011). "Mesenchymal stem cell transplantation and DMEM administration in a 3NP rat model of Huntington's disease: Morphological and behavioral outcomes." Behavioural Brain Research **217**(2): 369-378.

Rudd, AG, Hoffman, A, Grant, R, Campbell, JT, Lowe, D and Intercollegiate Working Party for, S (2011). "Stroke thrombolysis in England, Wales and Northern Ireland: how much do we do and how much do we need?" J Neurol Neurosurg Psychiatry **82**(1): 14-19.

Ryvolova, M, Chomoucka, J, Janu, L, Drbohlavova, J, Adam, V, Hubalek, J and Kizek, R (2011). "Biotin-modified glutathione as a functionalized coating for bioconjugation of CdTe-based quantum dots." Electrophoresis.

Saar, G, Zhang, B, Ling, W, Regatte, RR, Navon, G and Jerschow, A (2012). "Assessment of glycosaminoglycan concentration changes in the intervertebral disc via chemical exchange saturation transfer." NMR Biomed **25**(2): 255-261.

Sahni, A, Sporn, LA and Francis, CW (1999). "Potentiation of endothelial cell proliferation by fibrin(ogen)-bound fibroblast growth factor-2." J Biol Chem **274**(21): 14936-14941.

Saif, J, Schwarz, TM, Chau, DY, Henstock, J, Sami, P, Leicht, SF, Hermann, PC, Alcala, S, Mulero, F, Shakesheff, KM, Heeschen, C and Aicher, A (2010). "Combination of injectable multiple growth factor-releasing scaffolds and cell therapy as an advanced modality to enhance tissue neovascularization." Arterioscler Thromb Vasc Biol **30**(10): 1897-1904.

Saka, Ö, McGuire, A and Wolfe, C (2009). "Cost of stroke in the United Kingdom." Age and Ageing **38**(1): 27-32.

Samlowski, WE, Robertson, BA, Draper, BK, Prystas, E and McGregor, JR (1991). "Effects of supravital fluorochromes used to analyze the in vivo homing of murine lymphocytes on cellular function." J Immunol Methods **144**(1): 101-115.

Saporta, S, Borlongan, CV and Sanberg, PR (1999). "Neural transplantation of human neuroteratocarcinoma (hNT) neurons into ischemic rats. A quantitative dose-response analysis of cell survival and behavioral recovery." Neuroscience **91**(2): 519-525.

Schmidt, R, Nippe, N, Strobel, K, Masthoff, M, Reifschneider, O, Castelli, DD, Holtke, C, Aime, S, Karst, U, Sunderkotter, C, Bremer, C and Faber, C (2014). "Highly shifted proton MR imaging: cell tracking by using direct detection of paramagnetic compounds." Radiology **272**(3): 785-795.

Seevinck, PR, Deddens, LH and Dijkhuizen, RM (2010). "Magnetic resonance imaging of brain angiogenesis after stroke." Angiogenesis **13**(2): 101-111.

Seferos, DS, Prigodich, AE, Giljohann, DA, Patel, PC and Mirkin, CA (2009). "Polyvalent DNA nanoparticle conjugates stabilize nucleic acids." Nano Letters **9**(1): 308-311.

Sekar, RB, Kizana, E, Smith, RR, Barth, AS, Zhang, Y, Marban, E and Tung, L (2007). "Lentiviral vector-mediated expression of GFP or Kir2.1 alters the electrophysiology of neonatal rat ventricular myocytes without inducing cytotoxicity." American journal of physiology. Heart and circulatory physiology **293**(5): H2757-2770.

Seleverstov, O, Zabirnyk, O, Zscharnack, M, Bulavina, L, Nowicki, M, Heinrich, JM, Yezhelyev, M, Emmrich, F, O'Regan, R and Bader, A (2006). "Quantum dots for human mesenchymal stem cells labeling. A size-dependent autophagy activation." Nano Lett **6**(12): 2826-2832.

Shen, LH, Li, Y and Chopp, M (2010). "Astrocytic endogenous glial cell derived neurotrophic factor production is enhanced by bone marrow stromal cell transplantation in the ischemic boundary zone after stroke in adult rats." Glia **58**(9): 1074-1081.

Shen, Q, Goderie, SK, Jin, L, Karanth, N, Sun, Y, Abramova, N, Vincent, P, Pumiglia, K and Temple, S (2004). "Endothelial cells stimulate self-renewal and expand neurogenesis of neural stem cells." Science **304**(5675): 1338-1340.

Singh, S, Dwarakanath, BS and Lazar Mathew, T (2005). "Role of topoisomerases in cytotoxicity induced by DNA ligand Hoechst-33342 and UV-C in a glioma cell line." Indian J Exp Biol **43**(4): 313-323.

Siriwardena-Mahanama, BN and Allen, MJ (2013). "Strategies for optimizing water-exchange rates of lanthanide-based contrast agents for magnetic resonance imaging." Molecules **18**(8): 9352-9381.

Smith, EJ, Stroemer, RP, Gorenkova, N, Nakajima, M, Crum, WR, Tang, E, Stevanato, L, Sinden, JD and Modo, M (2011). "Implantation Site and Lesion Topology Determine Efficacy of a Human Neural Stem Cell Line in a Rat Model of Chronic Stroke." Stem Cells.

Song, Y, Xu, X, MacRenaris, KW, Zhang, XQ, Mirkin, CA and Meade, TJ (2009). "Multimodal gadolinium-enriched DNA-gold nanoparticle conjugates for cellular imaging." Angewandte Chemie **48**(48): 9143-9147.

Spitzer, N, Sammons, GS and Price, EM (2011). "Autofluorescent cells in rat brain can be convincing impostors in green fluorescent reporter studies." Journal of neuroscience methods **197**(1): 48-55.

Sprick, U (1991). "Long-term tracing of vital neurons with Hoechst 33342 in transplantation studies." J Neurosci Methods **36**(2-3): 229-238.

Stancanello, J, Terreno, E, Castelli, DD, Cabella, C, Uggeri, F and Aime, S (2008). "Development and validation of a smoothing-splines-based correction method for improving the analysis of CEST-MR images." Contrast media & molecular imaging **3**(4): 136-149.

Stanisz, GJ, Odrobina, EE, Pun, J, Escaravage, M, Graham, SJ, Bronskill, MJ and Henkelman, RM (2005). "T1, T2 relaxation and magnetization transfer in tissue at 3T." Magn Reson Med **54**(3): 507-512.

Steinbeck, JA, Choi, SJ, Mrejeru, A, Ganat, Y, Deisseroth, K, Sulzer, D, Mosharov, EV and Studer, L (2015). "Optogenetics enables functional analysis of human embryonic stem cell-derived grafts in a Parkinson's disease model." Nat Biotechnol **33**(2): 204-209.

Stille, M, Smith, EJ, Crum, WR and Modo, M (2013). "3D reconstruction of 2D fluorescence histology images and registration with in vivo MR images: application in a rodent stroke model." J Neurosci Methods **219**(1): 27-40.

Stroemer, P, Patel, S, Hope, A, Oliveira, C, Pollock, K and Sinden, J (2009). "The neural stem cell line CTX0E03 promotes behavioral recovery and endogenous neurogenesis after experimental stroke in a dose-dependent fashion." Neurorehabil Neural Repair **23**(9): 895-909.

Tanaka, EM and Ferretti, P (2009). "Considering the evolution of regeneration in the central nervous system." Nat Rev Neurosci **10**(10): 713-723.

Tang, H, Sha, H, Sun, H, Wu, X, Xie, L, Wang, P, Xu, C, Larsen, C, Zhang, HL, Gong, Y, Mao, Y, Chen, X, Zhou, L, Feng, X and Zhu, J (2013). "Tracking induced pluripotent stem cells-derived neural stem cells in the central nervous system of rats and monkeys." Cell Reprogram **15**(5): 435-442.

Teng, YD, Lavik, EB, Qu, X, Park, KI, Ourednik, J, Zurakowski, D, Langer, R and Snyder, EY (2002). "Functional recovery following traumatic spinal cord injury mediated by a unique polymer scaffold seeded with neural stem cells." Proc Natl Acad Sci U S A **99**(5): 3024-3029.

Tennstaedt, A, Aswendt, M, Adamczak, J and Hoehn, M (2013). "Noninvasive multimodal imaging of stem cell transplants in the brain using bioluminescence imaging and magnetic resonance imaging." Methods Mol Biol **1052**: 153-166.

Terreno, E, Geninatti Crich, S, Belfiore, S, Biancone, L, Cabella, C, Esposito, G, Manazza, AD and Aime, S (2006). "Effect of the intracellular localization of a Gd-based imaging probe on the relaxation enhancement of water protons." Magnetic resonance in medicine : official journal of the Society of Magnetic Resonance in Medicine / Society of Magnetic Resonance in Medicine **55**(3): 491-497.

Thonhoff, JR, Lou, DI, Jordan, PM, Zhao, X and Wu, P (2008). "Compatibility of human fetal neural stem cells with hydrogel biomaterials in vitro." Brain Res **1187**: 42-51.

Thored, P, Wood, J, Arvidsson, A, Cammenga, J, Kokaia, Z and Lindvall, O (2007). "Long-term neuroblast migration along blood vessels in an area with transient angiogenesis and increased vascularization after stroke." Stroke **38**(11): 3032-3039.

Trumble, TE and Parvin, D (1994). "Cell viability and migration in nerve isografts and allografts." J Reconstr Microsurg **10**(1): 27-34.

van der Zijden, JP, Wu, O, van der Toorn, A, Roeling, TP, Bleys, RL and Dijkhuizen, RM (2007). "Changes in neuronal connectivity after stroke in rats as studied by serial manganese-enhanced MRI." Neuroimage **34**(4): 1650-1657.

Vandeputte, C, Reumers, V, Aelvoet, S-A, Thiry, I, De Swaef, S, Van den Haute, C, Pascual-Brazo, J, Farr, TD, Vande Velde, G, Hoehn, M, Himmelreich, U, Van Laere, K, Debyser, Z, Gijsbers, R and Baekelandt, V (2014). "Bioluminescence imaging of stroke-induced endogenous neural stem cell response." Neurobiology of Disease **69**(0): 144-155.

Vandeputte, C, Thomas, D, Dresselaers, T, Crabbe, A, Verfaillie, C, Baekelandt, V, Van Laere, K and Himmelreich, U (2010). "Characterization of the Inflammatory Response in a Photothrombotic Stroke Model by MRI: Implications for Stem Cell Transplantation." Mol Imaging Biol.

Vega, MC, Garcia Saez, I, Aymami, J, Eritja, R, Van der Marel, GA, Van Boom, JH, Rich, A and Coll, M (1994). "Three-dimensional crystal structure of the A-tract DNA dodecamer d(CGCAAATTTGCG) complexed with the minor-groove-binding drug Hoechst 33258." Eur J Biochem **222**(3): 721-726.

Vinogradov, E, Sherry, AD and Lenkinski, RE (2013). "CEST: from basic principles to applications, challenges and opportunities." J Magn Reson **229**: 155-172.

Wakabayashi, K, Nagai, A, Sheikh, AM, Shiota, Y, Narantuya, D, Watanabe, T, Masuda, J, Kobayashi, S, Kim, SU and Yamaguchi, S (2010). "Transplantation of human mesenchymal stem cells promotes functional improvement and increased expression of neurotrophic factors in a rat focal cerebral ischemia model." J Neurosci Res **88**(5): 1017-1025.

Walling, MA, Novak, JA and Shepard, JR (2009). "Quantum dots for live cell and in vivo imaging." Int J Mol Sci **10**(2): 441-491.

Wang, PH, Schwindt, TT, Barnabe, GF, Motta, FL, Semedo, P, Beraldo, FC, Mazzali, M, Dos Reis, MA, Teixeira Vde, P, Pacheco-Silva, A, Mello, LE and Camara, NO (2009). "Administration of neural precursor cells ameliorates renal ischemia-reperfusion injury." Nephron Exp Nephrol **112**(1): e20-28.

Wang, Y, Mo, Y and Zhou, L (2011). "Synthesis of CdSe quantum dots using selenium dioxide as selenium source and its interaction with pepsin." Spectrochimica acta. Part A, Molecular and biomolecular spectroscopy.

Weissler, B, Gebhardt, P, Duppenbecker, P, Wehner, J, Schug, D, Lerche, C, Goldschmidt, B, Salomon, A, Verel, I, Heijman, E, Perkuhn, M, Heberling, D, Botnar, R, Kiessling, F and Schulz, V (2015). "A Digital Preclinical PET/MRI Insert and Initial Results." IEEE Trans Med Imaging.

Weksler, BB, Subileau, EA, Perriere, N, Charneau, P, Holloway, K, Leveque, M, Tricoire-Leignel, H, Nicotra, A, Bourdoulous, S, Turowski, P, Male, DK, Roux, F, Greenwood, J, Romero, IA and Couraud, PO (2005). "Blood-brain barrier-specific properties of a human adult brain endothelial cell line." FASEB journal : official publication of the Federation of American Societies for Experimental Biology **19**(13): 1872-1874.

White, LJ, Kirby, GT, Cox, HC, Qodratnama, R, Qutachi, O, Rose, FR and Shakesheff, KM (2013). "Accelerating protein release from microparticles for regenerative medicine applications." Mater Sci Eng C Mater Biol Appl **33**(5): 2578-2583.

Woo, CW, Lee, BS, Kim, ST and Kim, KS (2010). "Correlation between lactate and neuronal cell damage in the rat brain after focal ischemia: An in vivo 1H magnetic resonance spectroscopic (1H-MRS) study." Acta Radiol **51**(3): 344-350.

Woods, M, Woessner, DE and Sherry, AD (2006). "Paramagnetic lanthanide complexes as PARACEST agents for medical imaging." Chemical Society reviews **35**(6): 500-511.

Wu, J, Apontes, P, Song, L, Liang, P, Yang, L and Li, F (2007). "Molecular mechanism of upregulation of survivin transcription by the AT-rich DNA-binding ligand, Hoechst33342: evidence for survivin involvement in drug resistance." Nucleic Acids Res **35**(7): 2390-2402.

Yim, H, Seo, S and Na, K (2011). "MRI Contrast Agent-Based Multifunctional Materials: Diagnosis and Therapy." Journal of Nanomaterials **2011**.

Yoo, AJ, Pulli, B and Gonzalez, RG (2011). "Imaging-based treatment selection for intravenous and intra-arterial stroke therapies: a comprehensive review." Expert Rev Cardiovasc Ther **9**(7): 857-876.

Yu, F and Morshead, CM (2011). "Adult stem cells and bioengineering strategies for the treatment of cerebral ischemic stroke." Current stem cell research & therapy **6**(3): 190-207.

Zanzonico, P, Dauer, L and St Germain, J (2008). "Operational radiation safety for PET-CT, SPECT-CT, and cyclotron facilities." Health Phys **95**(5): 554-570.

Zaremba, LA (2002) "FDA Guidelines for Magnetic Resonance Equipment Safety ".

Zhang, L, Zhang, F, Weng, Z, Brown, BN, Yan, H, Ma, XM, Vosler, PS, Badylak, SF, Dixon, CE, Cui, XT and Chen, J (2013). "Effect of an Inductive Hydrogel Composed of Urinary Bladder Matrix Upon Functional Recovery Following Traumatic Brain Injury." Tissue engineering. Part A.

Zhang, RL, Zhang, ZG, Roberts, C, LeTourneau, Y, Lu, M, Zhang, L, Wang, Y and Chopp, M (2008). "Lengthening the G(1) phase of neural progenitor cells is concurrent with an increase of symmetric neuron generating division after stroke." J Cereb Blood Flow Metab **28**(3): 602-611.

Zhang, ZG, Zhang, L, Jiang, Q, Zhang, R, Davies, K, Powers, C, Bruggen, N and Chopp, M (2000). "VEGF enhances angiogenesis and promotes blood-brain barrier leakage in the ischemic brain." J Clin Invest **106**(7): 829-838.

Zhao, H, Doyle, TC, Coquoz, O, Kalish, F, Rice, BW and Contag, CH (2005). "Emission spectra of bioluminescent reporters and interaction with mammalian tissue determine the sensitivity of detection in vivo." J Biomed Opt **10**(4): 41210.

Zhong, J, Chan, A, Morad, L, Kornblum, HI, Fan, G and Carmichael, ST (2010). "Hydrogel matrix to support stem cell survival after brain transplantation in stroke." Neurorehabil Neural Repair **24**(7): 636-644.

Zhu, W, Zhou, LF, Wang, Y, Zhu, JH and Mao, Y (2004). "[Transplantation of gene-transfected neural stem cells for transient cerebral ischemia in rats]." Zhonghua Yi Xue Za Zhi **84**(12): 1029-1034.

Zu, Z, Spear, J, Li, H, Xu, J and Gore, JC (2014). "Measurement of regional cerebral glucose uptake by magnetic resonance spin-lock imaging." Magn Reson Imaging.

Publications arising from this thesis

Papers

Modo M, Kolosnjaj-Tabib J, **Nicholls F**, Ling W, Wilhelm C, Debarge O, Gazeau F and Clement O. (2013) Considerations for the clinical use of contrast agents for cellular MRI in regenerative medicine. Contrast Media & Molecular Imaging 8(6):439

Book chapters

Nicholls F, Ling W, and Modo M. (2014) In vivo imaging of cell dynamics by Magnetic Resonance Imaging (Chapter) in Cell Imaging: Methods Express (In Press, Wiley-Blackwell)

Nicholls F, Gorenkova N, Bible E, Franco C, Chau D, Tolias C, Shakesheff K, West J and Modo M. (2013) Improving the Treatment of Stroke through Nanotechnology (Chapter 21) in Kateb B and Heiss JD (eds), Nanoneuroscience and Nanoneurosurgery. 283-298, CRC Press.

Chung CH, **Nicholls F**, & Modo M. (2013). Image-guided injection and non-invasive monitoring of regeneration in the stroke-damaged brain (Chapter 7) in Walczak, P. & Jolkkonen, J. (eds), Cell-based Therapies in Stroke. 93-104. Springer Verlag.

Conference Abstracts

Ling W, **Nicholls FJ,** Kim S, Ferrauto G, Delli Castelli D, Aime S and Modo M. Optimization of Detection Parameters for Eu-HPDO3A in agarose gel. Poster presentation by W Ling at *ISMRM* 2014, Italy

Massensini AR, Medberry CJ, **Nicholls FJ,** Ling W, Badylak SF and Modo M. Use of MRI to noninvasively guide ECM-gel treatment of stroke lesions in a rat model. Poster presentation by M Modo at *ASNTR* 2014*,* FL

Nicholls FJ, Ling W, Ferrauto G, Massensini AR, Delli Castelli D, Aime S. and Modo M. Using ParaCEST MRI to simultaneously track two cell populations in vivo. Poster presentation by **F Nicholls** at *MIRM Scientific Retreat* 2014, PA and *ASNTR* 2014*,* FL

Ling W*, **Nicholls F***, Massensini AR, Delli Castelli D, Medberry CJ, Badylak SF, Aime S and Modo M. The potential of ParaCEST for independent in vivo tracking of multiple cell populations. Poster presentation by M Modo at *INTR* 2013, Cardiff (*indicates equal author contribution).

Ling W, **Nicholls F,** Aime S, Delli-Castelli D and Modo M. Evaluation of ParaCEST detection threshold on human stem cells under physiological constraints. Poster presentation by W Ling at *ISMRM* 2013, UT

Nicholls F, Ling W, Delli Castelli D, Ferrauto G, Medberry CJ, Jin T, Kim S-G, Badylak SF, Aime S and Modo M. The potential of CEST for independent in vivo tracking of transplant components. Poster presentation by **F Nicholls** at *MIRM Scientific Retreat* 2013, PA

Rossetti T, **Nicholls F** and Modo M. A systematic in vitro investigation of cell preparation for intracerebral cell implantation. *Cell Transplantation* 22(5): 914. Poster presentation by M Modo at *ASNTR* 2013*,* FL

Nicholls F, Uwanogho D, Bible E, Williams B and Modo M. Dying to be seen? The biological effect of labeling neural stem cells. Poster presentation by **F Nicholls** at *SfN* 2012, LA

Nicholls F, Bible E, Hicks C, Tolias CM, & Modo M. Validating Exogenous Markers of Transplanted Cells. *Cell Transplantation* 20(4): 577-8. Oral presentation by **F Nicholls** at *INTR/ASNTR* 2011*,* FL